Aeroelastic and structural optimization for weight reduction of a wind turbine rotor blade

Master Thesis

Ira Lange

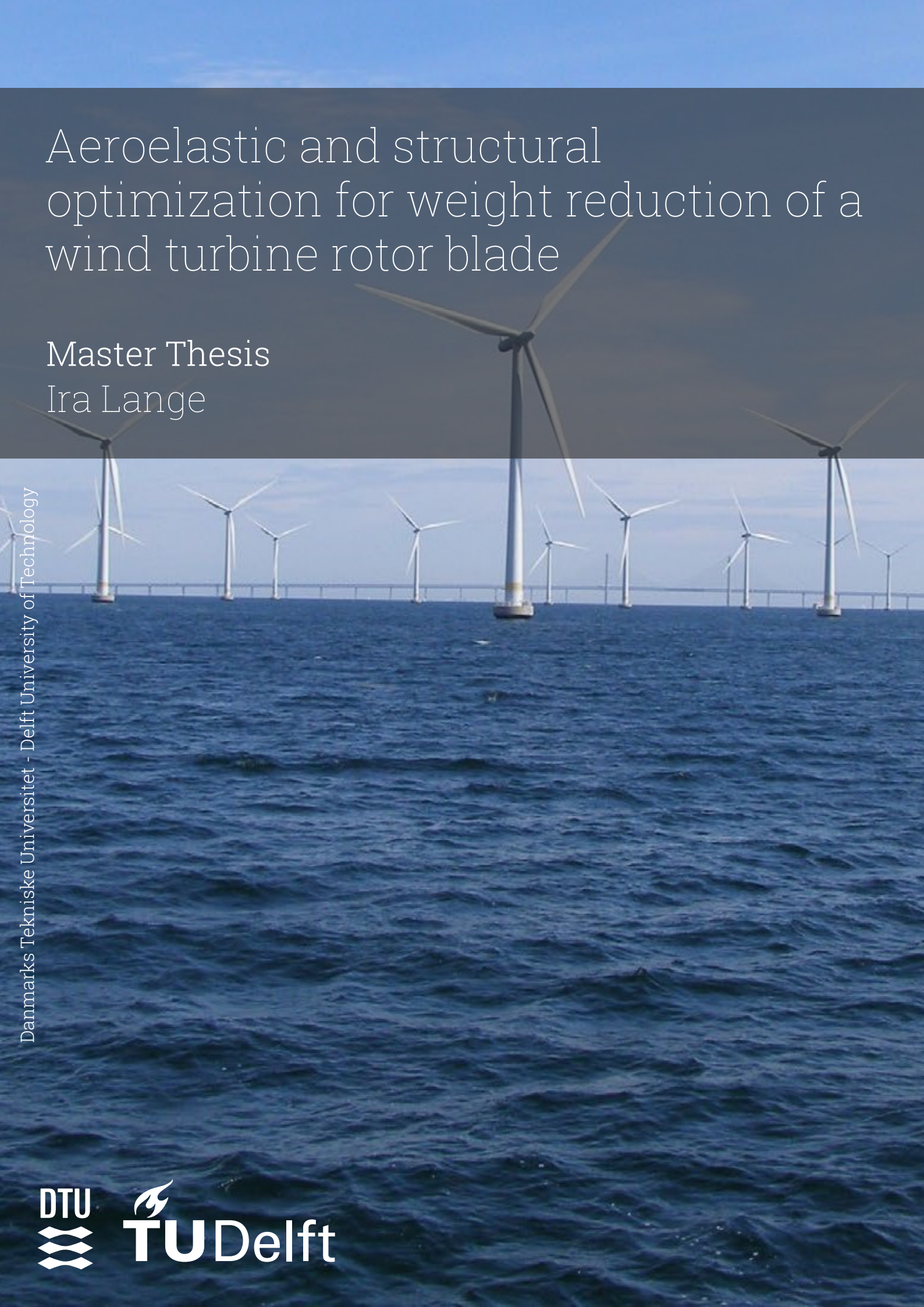

Danmarks Tekniske Universitet - Delft University of Technology

DTU TU Delft

Author:
Ira Lange

Title:
Aeroelastic and structural optimization for weight reduction of a wind turbine rotor blade

European Wind Energy Master Thesis
ECTS: 45

Education:

Master of Science
Aerospace Engineering
Technical University of Delft

Master of Science
Wind Energy
Technical University of Denmark

Remarks:
This report is submitted as partial fulfillment of the requirements for graduation in the above education at the Technical University of Delft and the Technical University of Denmark.

Cover image: Courtesy of DTU Wind Energy

August 2025

Supervisors:

Julie Teuwen
TU Delft Faculty of Aerospace Engineering

Philipp Ulrich Haselbach
Peter Berring
David Robert Verelst
DTU Wind & Energy Systems

Troels Ette
Thorbjørn Sætre
Olsen Wings A/S

Ole Sangill
NorZet Ltd

Technical University of Delft Faculty of Aerospace Engineering
Kluyverweg 1, 2629 HS Delft
Netherlands
www.tudelft.nl/en/ae

Technical University of Denmark Department of Wind Energy Frederiksborgvej 399
4000 Roskilde
Denmark
www.wind.dtu.dk

Preface

This thesis is the final step of the two-year European Wind Energy Master program. The past two years were not always easy, but they have helped me grow a lot, both academically and personally. Ending this chapter with a thesis on blade redesign and being able to work on a real-life project has been very rewarding.

I would like to thank my supervisors at DTU and TU Delft for making this project possible and for their support along the way. A special thanks goes to Philipp and Julie for your guidance and advice throughout the project. I also want to thank Frederick, David, and Peter, who were always ready to answer my questions and explain their research and software.

My gratitude also goes to Thorbjørn and Troels from Olsen Wings A/S and Ole from Norzet Ltd. for your trust and for the valuable input you provided while I worked on your turbine and blade models.

I am thankful as well for the friends I met along the way, who made these years so much fun. From board game nights to Aperol Spritzes and much more, you made this journey so much more enjoyable.

Most of all, I would like to thank my family for their constant support over the years. I would not be here without you, and I am very grateful to have you in my life.

Ira Lange
Copenhagen, September 2025

Abstract

Lightweight wind turbine blades play a crucial role in improving wind turbine technology. They enforce lower loads on the overall system, making material and cost savings possible. Also, increasingly longer blades can be used, enabling more efficient, economically viable turbines. This thesis investigates how the mass of a rotor blade can be reduced without compromising its structural integrity. The work is based on the OLW934 blade from Olsen Wings A/S. Its mass is reduced using a comprehensive optimization framework.

A structural and aeroelastic optimization process was applied using the gradient-based AESOpt algorithm, finite element analysis (FEM), and aeroelastic checks with HAWC2S. The framework reduced the blade's mass by 35% while keeping its structural integrity. The redesigned blade was found with improved internal structure and layup. Since the optimization mainly focused on the structure, the aeroelastic performance was checked manually throughout the process. Due to stiffness assumptions in the tip region, no definite validation on the aeroelastic stability of the turbine with the redesigned blade has been found yet, but the results indicate sufficiency.

This behaviour should be verified. Also, the internal structure setup, especially the spar caps and shear webs, should be studied in more detail, as only initial design considerations were explored. Additionally, varying initial layup regions and evaluating alternative material options could yield further improvements. Still, the results show that the structural optimization framework used can significantly reduce blade mass and can be applied to other designs. This supports the development of lighter blades and better turbine performance.

Contents

1 Introduction

In the past few decades, the wind energy industry has been evolving immensely [1]. As a green energy source, wind energy is one of the solutions for addressing the increasing climate change challenges and ongoing energy crisis [1]. Different optimization strategies can be utilized to compete with other energy sources and decrease the cost of energy for wind turbines. This paper will focus on reducing the blade mass, which would result in multiple positive cascading effects.

One direct effect of decreasing the mass of a wind turbine rotor blade is the reduction in the amount of material used. That can reduce the cost of the blade by lowering material costs. Following that, transportation and installation costs can also be decreased because, for example, expensive high-capacity cranes are not necessary. Less heavy blades also induce less gravity and inertia loads, lowering the requirements for the downstream components of the turbine and lowering their cost [2] [3].

All sizes of turbines would profit from this development. When looking at big turbines, the size of the turbine and, therefore, the power output is limited by the weight of the blades, inducing critical in-plane root bending moments. The possibility of longer blades would significantly impact the annual energy production of a turbine, because the power increases squarely with the blade length [4]. However, small wind turbines would also profit from lighter blades. While the in-plane blade root moment is less of an issue for these turbines, the low wind speed performance is. These turbines are often used in regions with only little wind resources. Therefore, they operate mainly in the low wind regime, and a reduced wind speed would be favorable for the annual energy production [5]. For that, lighter blades are necessary as they have less inertia. Still, the stiffness of the structure needs to be sufficient to withstand the extreme and fatigue loads and maintain sufficient tower clearance [5].

The blade optimized in this project is the 9.34 m long OLW934 blade from Olsen Wings A/S. It is supposed to be used in a rotor redesign project started by NorZet Ltd for about 800 installed E-3120 downwind, stall-regulated, fixed-speed turbines in the UK. About 550 of these, however, require lighter blades than the OLW934. This is the case because these are original turbines that need to be retrofitted with a new rotor. The remaining about 250 turbines are the next evolution with updated shafts and bed plates, which can carry the loading induced by the original blade. A new blade design

based on the OLW934 is necessary to retrofit the original turbines with reduced mass. The current weight of the in reality manufactured blades is around 327 kg [6]. This project aims to achieve a target weight reduction of 75 kg. Usually, a blade design is done by improving the blade's aerodynamic, structural, and aeroelastic design. However, a requirement in this project is that Olsen Wings A/S will use the same molds as the ones for the OLW934 blade to produce the new blade. This requires the outer surface of the blade to stay the same and, therefore, also the aerodynamic design, limiting the optimization in this project to the aeroelastic and structural design.

The current mass of around 327 kg of the OLW934 is relatively high when compared to existing comparable blades [6]. A similarly long blade of 9 m made by the National Renewable Energy Laboratory (NREL) weighs 116.57 kg [7]. The 12.6 m blade designed and manufactured by DTU Wind and Energy Systems weighs 362 kg, approximately the same weight as the OLW934 blade, but is 3.26 m longer [8]. Thus, there is a strong indication that significant weight reduction for the OLW934 blade is feasible.

This report presents the optimization framework applied to the OLW934 blade and the weight reduction achieved. It also highlights the strengths and weaknesses of the framework and provides a critical evaluation of the redesigned blade using structural and aeroelastic analyses. Following a background chapter outlining the state of the art and key theory in chapter 2, the report presents two main parts. In the first part, the current OLW934 blade is analyzed and improvement potential is identified, by explaining the methodology in chapter 3 and presenting the results and analysis in chapter 4. In the second part, the methodology and results of the redesign process are shown in chapter 6 and chapter 7. After critically discussing the findings in chapter 8, the report concludes with a conclusion of the findings and what future work should be done in chapter 9.

2

Background

This chapter discusses the state of the art in the wind turbine blade design research field and important background information for the design process, including the design process steps, materials, layups, optimization strategies, and structural modeling. Also, typical failure causes and measures to prevent them, as well as what loads must be sustained by wind turbine blades, are evaluated. Moreover, a review of the design loads and life assessment is shown. Lastly, the background chapter ends with a description of this project's research objectives.

2.1. Blade design process

The design of a wind turbine blade involves an iterative process that integrates aerodynamic, aeroelastic, and structural considerations to optimize performance and durability, shown in Figure 2.1. The aerodynamic design focuses on blade length, airfoil selection, chord distribution, relative thickness, and twist to maximize power generation while minimizing drag and roughness sensitivity [9]. The structural design ensures that the blade can withstand operational and extreme loads by optimizing material composition and geometric configuration, typically using composite materials [9]. The aeroelastic design then assesses the dynamic response of the blade, ensuring stability under varying wind conditions by analyzing interactions between aerodynamic forces and structural flexibility [9]. These three aspects are interconnected because wind turbine blades are aeroelastic structures. Aeroelasticity describes the phenomenon of aerodynamic loads influencing the deformation of a structure and a deformed structure changing the aerodynamic loads. In the design process, all three aspects cannot be optimized separately as they influence each other later in the turbine's operation. The iterative process refines the design to balance power efficiency, load mitigation, and material constraints, ultimately achieving an optimized lightweight and high-performance rotor.

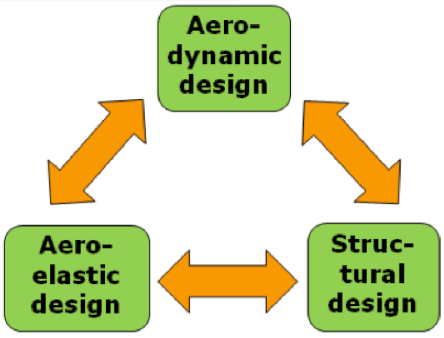

Figure 2.1: Wind turbine design. [10]

The iterative design process described in the IEC 61400-5 standard is shown in Figure 2.2 [11]. After completing the aerodynamic design, the first preliminary structural design is made [11]. The loads are evaluated using an aeroelastic solver [11] for this design. The ultimate and fatigue loads get evaluated [11]. If the structural integrity is sufficient under the loads and the objective function of the optimization reaches an acceptable value, the design is complete; if not, a new aerodynamic and structural design needs to be made and reevaluated [11]. In this project, the aerodynamic design is considered constant, and the structural design will be improved in a new iteration to result in sufficient structural integrity.

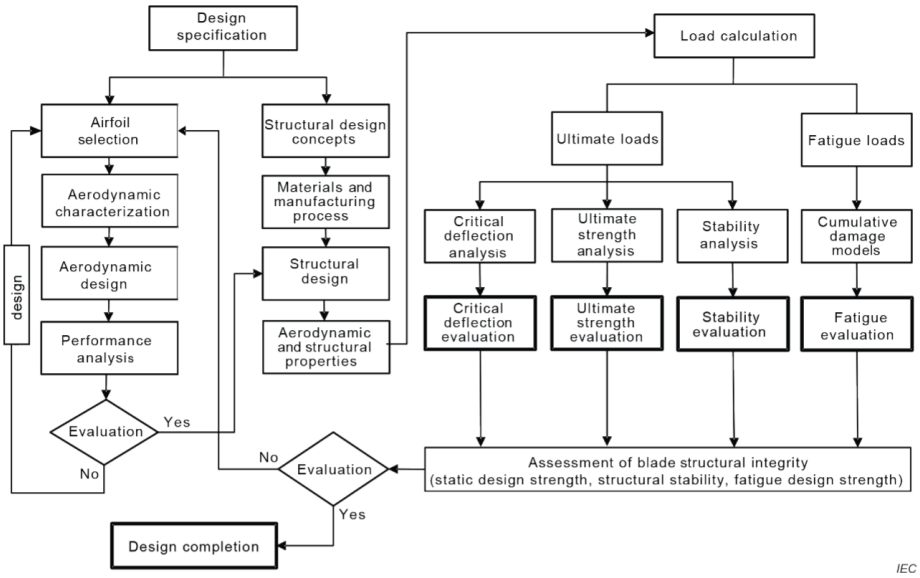

Figure 2.2: Wind turbine blade design process. [11]

The literature underscores the importance of integrating aerodynamic, structural, and aeroelastic considerations in an iterative design process for wind turbine blades. While the iterative nature of design is well-recognized, limited information is provided on how different design choices affect the aeroelastic behaviour and what design changes are effective to overcome possible problems in the assessment of the blades' structural integrity during the iterative process. This will be investigated during this work based on the case study of the OLW934 blade.

2.2. Structural design

The structural design of a rotor blade determines its stiffness and strength and, therefore, its ability to withstand loads. The internal structural design is thus critical for a sufficient wind turbine design to result in a lightweight design, which keeps its structural integrity. The wind turbine blade consists mainly of two outer shells and a bonded spar. That can be seen in Figure 2.3. These parts have different functions to ensure sufficient blade stability, needing different materials and lay-ups. Usually, the blades are manufactured in parts and joined afterward using adhesives. However, Siemens uses an integral approach, manufacturing the whole blade in one part, reducing the extra process step of the assembly and the adhesive material, resulting in a mass reduction [12].

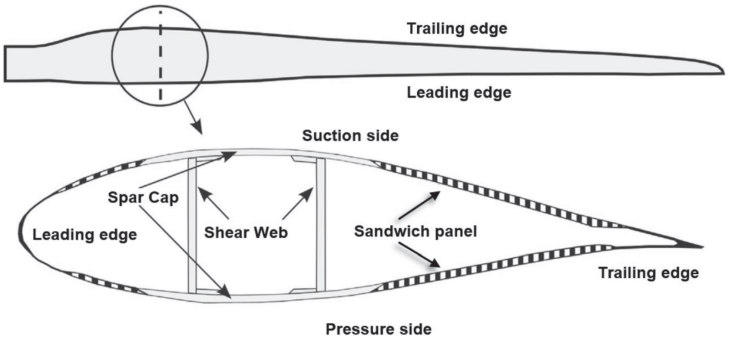

Figure 2.3: Internal structure wind turbine blade. [13]

The two outer shells, as can be seen in Figure 2.3, form the airfoils along the blade span, resulting in pressure on the upwind side and suction on the downwind side. Adhesive joints are used to bond them together at the leading and trailing edges. The outer shell's main task, next to providing the desired aerodynamic performance, is to prevent buckling and ensure the stability of the structure [14]. That is done using sandwich structures in the leading and trailing panel regions [15]. These increase the second moment of area I, resulting in higher critical local bending and buckling loads than an outer skin without them. Next to buckling are the skin areas in the leading and trailing edge, also subjected to tension-compression loads [15]. Gravitational loads of the blade induce edgewise bending moments that have to be withstood by the edges [15]. Reduced mass of the blade can thus decrease the reinforcements in these areas, resulting in even higher mass reduction.

The outer shell is reinforced using a spar. The function of the spar is to provide flexural rigidity for the blade and keep the structural integrity in operation by restricting shear between the two aeroshells [15]. The pressure side of the spar is subjected to cyclic tension-tension loading and the suction side to cyclic compression-compression [15]. There are different possible spar designs, one or multiple shear webs with a spar cap, as shown in Figure 2.3, or a box girder, made as a box or in the shape of an eight, where the spar cap is not part of the skin layup [16]. Instead, the box girder is manufactured as its own part and glued into the outer skin of the blade. The different designs can be seen in Figure 2.4. This design thus imposes the drawback of higher adhesive mass than the shear web design.

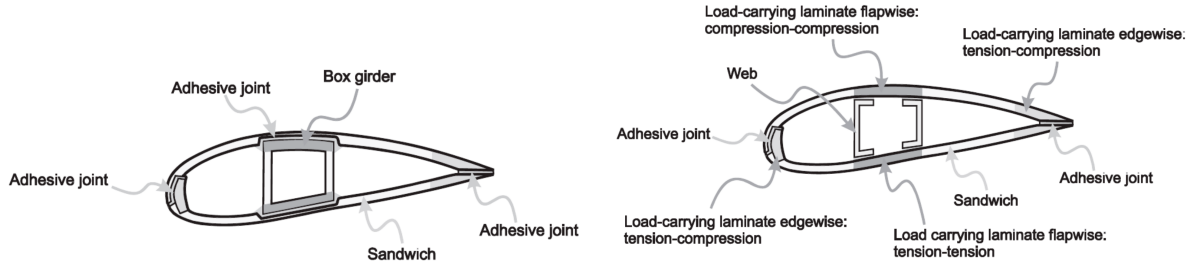

(a) Box girder spar design. **(b)** Shear web spar design.

Figure 2.4: Box girder and shear web spar cap design [17].

Depending on which spar is chosen and its position in the blade, the blade's stiffness and strength are affected immensely. This affects the blade's ability to withstand loads and changes in stiffness and mass, which also directly affect the blade's natural frequency. The aeroelastic stability of the blade is, therefore, directly dependent on how the spar is designed [16].

Literature shows that different designs of the internal structure can be used. It comprehensively shows which functions the different parts of the structure have and shows that they affect the blades' performance. Especially the choice of spar design and placement has a high impact. The investigation of these effects will be addressed in the course of this report for the case of the OLW934 blade. An investigation on how different internal structure designs affect the blade mass distribution, and structural and aeroelastic behaviour of a wind turbine blade will be done.

2.2.1. Materials

The materials used for wind turbine blades are composite materials because they have a high specific strength and stiffness. They consist of stacked plies, which are made of fibers and matrix material, as can be seen in Figure 2.5.

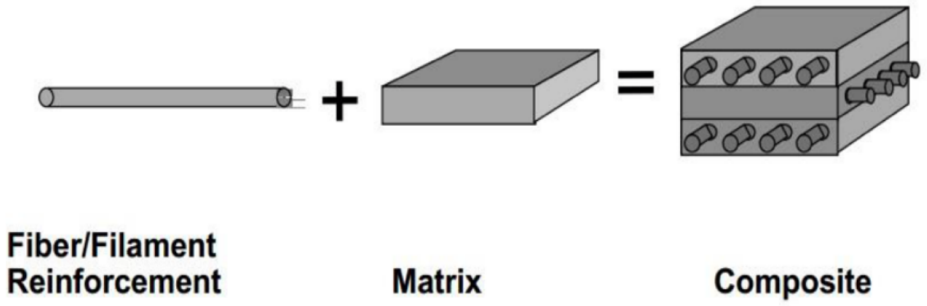

Figure 2.5: Composite material. [18]

The fibers provide strength in their longitudinal direction, and the matrix distributes the stress between the fibers [5]. While the longitudinal stiffness and strength of the fibers are typically way higher than those of the matrix, the transverse stiffness and strength are typically lower. The matrix material is homogeneous. The loads applied

in the transverse direction need to be accounted for by the matrix. Composite materials have, therefore, orthotropic characteristics, with different properties in and out of the fibre direction.

The matrix also holds the function of fracture toughness and protects the fibers from environmental effects [5]. To increase the second moment of inertia, as explained in section 2.2, sandwich structures are also used in wind turbine blades. Core materials can thus also be part of the lay-up. A composite's mechanical properties and performance heavily depend on its stacking sequence, thickness, ply alignment, fiber volume fraction, and void content. Therefore, using composites, a specifically tailored material can be achieved. A low fiber volume fraction and high void content reduce the performance of the composite. Lower fiber volume fractions result in lower strength and stiffness values, and high void contents lessen the material's resistance against delamination. Having suitable fiber volume fractions and void contents are mainly dependent on the manufacturing process.

The most common materials used as reinforcing fibers in wind turbine blades are glass fibers and carbon fibers, used selectively [14]. Glass fibers are used mainly as they have a high tensile strength while still being a low-cost material [5]. Carbon fibers typically have a higher tensile strength and tensile modulus with 3–7 GPa and 200–935 GPa compared to 3.5 GPa and 70–80 GPa for glass fibers [19], [20]. This also results in a lower sensitivity to fatigue [5]. Carbon fibers also have less density, making them lighter and more favorable [5]. Compared to glass fibers, they are, however, much more costly with 30 $/kg compared to 1.87 $/kg in 2019 [21]. Therefore, the amount of carbon fibers used is always a trade-off between material costs and weight loss, which also results in lower costs when considering the cascading effects of a lighter blade, described in chapter 1. Thus, full glass fiber blades and hybrid blades, including different amounts of carbon fibers, are used. Pultruded carbon planes are typically used in the spar cap region to increase their strength in the fiber direction. The function of this blade region will be explained in subsection 2.2.2. For smaller blades, it is more favorable to use fewer carbon fibers than for longer blades, as the loads experienced by the longer blades induced by their weight are significantly higher, justifying the higher material costs [4]. In the original OLW 934 blade Olsen Wings A/S used a pure glass fiber blade, likely following that logic and reducing material costs.

The matrix materials used in wind turbine blades can be divided into thermoset and thermoplastic polymers, with stiffnesses between 1.4 and 3.5 GPa and tensile strengths between 21 to 100 MPa [22]. Thermoset polymers can cure at way lower temperatures, making the fabrication cheaper [4]. Thermoplastic materials have the advantage of recyclability as they go to their original viscous form when heated [4]. Their high viscosity and the need for high processing temperatures make them costly in fabrication, which is why they are not used and further discussed in this project [4]. The two main thermoset matrices widely used are epoxy and polyester.

While epoxy has superior performance in terms of strength and durability, polyester is often used because of its low cost while having appropriate mechanical properties [4].

Also, it has a faster cycle time and improved energy efficiency [23]. The bigger blades are often made with epoxy, resulting in higher performance. Next to its relatively low costs, polyester has the advantage of relatively easy manufacturability [24]. The molding and curing can be done at room temperature and atmospheric pressure [24]. The easy manufacturability aids polyester as a good option for small wind turbine blades, which is likely why Olsen Wings A/S uses it in their blade manufacturing.

One of the most common core materials used is balsa wood, a natural material known for its high stiffness, strength, and cost-effectiveness [25]. It is, therefore, often used in the inner span of the rotor blade [26]. One drawback of Balsa wood is that the outer layers of the wood often absorb resin in the infusion process, resulting in significant weight gain [26]. This can be reduced by using higher-cost balsa with surface treatment, losing the advantage of a cost-effective core material [26]. Balsa wood is also inherently heavier and more brittle than, for example, polymer foams, including Polyvinyl Chloride (PVC) and Polyethylene Terephthalate (PET) [25]. Even though they have worse mechanical properties than balsa, they offer a low-cost and mass solution [26]. They have a high strength and stiffness-to-weight ratio [25]. Additionally, foams have a higher damage tolerance and do not experience catastrophic failure, leaving time for repairs [25]. The foam is also easily shaped to different forms and bonded to the face sheets [26]. Polymer foams offer a balanced combination of strength, stiffness, and weight, making them a versatile option for wind turbine blades, often found in the outer part of wind turbine blades [25], [26]. The choice of core material depends on the requirements, such as mechanical performance, weight, and cost. It is common to use a combination of different core materials along the length of the blade to optimize performance and ensure the turbine's efficiency. The small blades manufactured by Olsen Wings A/S use Soric material as a core. It is a foam core with hexagon foam elements and resin flow channels in between [27]. In their design, no Balsa wood was used, likely because it is not as suitable for small blades due to its weight drawback.

During this report, the materials of the original OLW934 are largely kept the same to adhere to the requirements of OLW934; the main focus is, however, on how they are used to find the most effective internal structure and layup.

2.2.2. Layup

A wind turbine blade layup is one of the most important design parameters when optimizing for a good structural design. Composites are stacked fiber plies with characteristic properties bonded together with a matrix. The plies can have inherently different mechanical properties, like glass or carbon fibers, or they could be manufactured differently. Next to the material being different, the same kind of ply can also be placed in different directions, resulting in a change in the mechanical properties of the combined composite. The resulting composite will have significantly different stiffnesses and stresses in all loading cases [28]. Next to increasing or decreasing strength in specific directions, coupled tension-bending, tension-torsion, and bending-torsion behaviour can be achieved by strategically designing the layup. This can be done by changing the layup to be nonsymmetrical or unbalanced. This unique behaviour of composites can be used as an advantage for a design by having a passive structure

change when subjected to specific loading. One example could be the automatic change of the airfoil characteristic when reaching too close to the stall to prevent getting into high load variations in the stall region. Next to the ply layup is the thickness distribution through the structure and the placement of ply drops influencing the structural performance [28]. Only dropping one ply at a time reduces the induced loads from redistributing the stress carried in that ply to the other plies significantly [14]. All these design parameters are part of getting a high-performance design. Different requirements are employed for different blade parts as described in 2.2. Therefore, the layup design has to be done for each part individually.

The internal and external skins are usually triax or double-bias lay-ups that reach around the whole blade, as shown in Figure 2.6 [29], [30]. As the spar is taking on the flapwise bending loads, this section, especially the spar cap, has the biggest influence on the blade weight as it is a thick laminate with mainly unidirectional fibers [28]. This can also be seen in Figure 2.6. The fiber thickness of the spar cap reduces with the flapwise bending moment from the root to the tip [4]. The trailing and leading edge lay-ups are usually much thinner and have less influence on the blade mass [28]. They carry the edgewise bending loads and are reinforced using UD layers with a thin core [29], [30]. The skins between these two main load-bearing regions are normally sandwich structures using a thicker core to resist buckling loads [4], [29]. Because the shear webs carry the shear loads, they are usually done with a biaxial lay-up and a core [4].

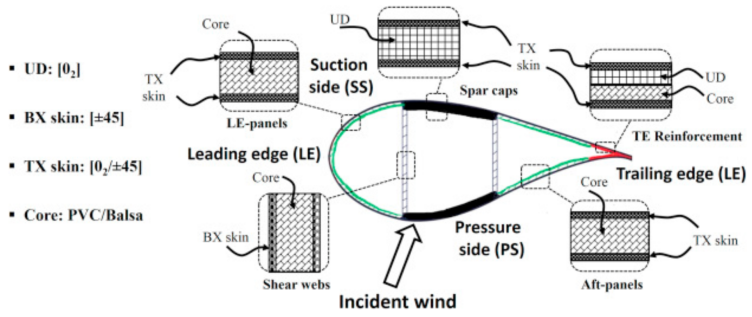

Figure 2.6: Typical lay-up in the different regions of a wind turbine blade. [30]

The original OLW934 blade uses a box girder design. For a box girder design, the general layup regions are similar. The spar cap region is, however, built differently. The UD material is not part of the outer skin layup. The UD-layers are building the box girder layup, which gets glued on the inside of the outer blade skin. This thus changes the properties of the region significantly. This was also done in the original OLW934 blade.

The literature does not sufficiently show what influence a change between spar designs and the corresponding changes in the layup have on the structural and aeroelastic behaviour of a wind turbine blade. This will be investigated in the course of this report. Additionally, based on the OLW934 blade, the thickness distribution of these regions is investigated for small wind turbine blades. Following that, it is investigated

where in the blade the highest potential for mass reduction is present, showing the optimization importance level for the different regions in the design of a wind turbine blade.

2.2.3. Optimization strategies

This subsection shows different optimization strategies and examples of mass reductions using them. When doing a structural optimization for a wind turbine blade, the approaches can be divided into two main categories [29]. The first is a topology optimization over the whole blade to find the optimal distribution of material, like Neil Buckney et al. and José Pedro Blasques and Mathias Stolpe did [31], [32]. Because this kind of optimization often results in a complex distribution of material, it often also results in a higher difficulty in the manufacturing process [29]. Additionally, the optimization is more complicated, resulting in longer computational times. The second category of using a typical blade build-up is focused on in the following [29]. Utilizing knowledge about typical blade build-ups reduces the optimization effort to the material selection, the material distribution on different parts of the blade, and the positions of reinforcements, making the optimization process faster and helping manufacturability [29]. This category can, however, be divided again into gradient- and evolutionary-based algorithms [33].

The gradient-based methods optimize the parameters by using the gradient of the objective function [33]. The gradient describes the change in the objective function for the parameters at the specific design point [33]. It, therefore, shows in which direction the parameters need to be changed to get to the optimal solution [33]. A typical gradient optimization method flow chart is shown in Figure 2.7. The optimization starts by evaluating the blade with the current thicknesses in a finite element analysis, resulting in measures of objective function m and the structural constraints g [29]. These will be explained later. Next, a sensitivity analysis is done using the current configuration to result in the differentials of the objective function and the structural constraints to the thickness [29]. This information is used in the solver [29]. This flowchart uses a sequential linear programming (SLP) approach, which formulates a linearized optimization problem and solves it to determine a design update Δt [29]. The solver finds the direction and magnitude of change to improve the objective function while complying with the structural constraints [29]. The next step is to check for convergence of the objective function m while complying with the constraints [29]. When the solution is converged, the optimal design is found. If not in the next step, a global convergence filter prevents the optimizer from accepting changes that violate constraints more than a set tolerance or destabilize the process [29]. It calculates m and g using a finite element analysis using the updated $t+\Delta t$ for the next iteration [29]. When the constraints are not overly violated, and the step is not too significant, the changed thickness is accepted, and the next iteration starts with the new design [29]. However, if they are violated more than the set tolerance, the move limits get reduced, and the linear solver solves for a new Δt [29]. Next to linear programming (SLP), Sequential Quadratic Programming (SQP) can also be used for the gradient approaches [34]. It uses a quadratic solver instead of a linearized solver [34]. A quadratic solver uses more computational time per iteration but needs fewer iterations to converge, as it

finds better solutions [35]. Generally, it thus needs overall less computational time [35].

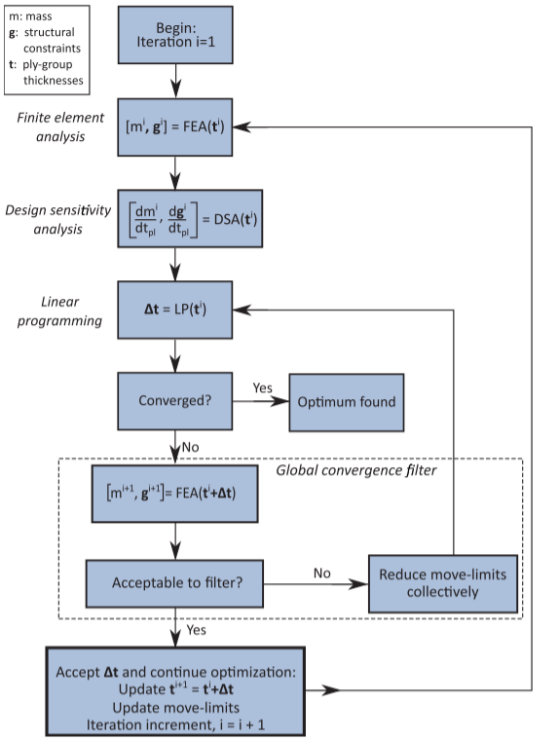

Figure 2.7: Flow chart of a gradient optimization algorithm using sequential linear programming (SLP) and optimizing the thickness.[29]

An evolutionary algorithm, on the other hand, simulates the evolution of a population [33]. Different evolutionary algorithms are, for example, genetic and particle swarm algorithms [33]. The genetic algorithm randomly generates design solutions as a first generation [4]. These get evaluated using a fitness parameter [36]. All solutions get assigned a fitness value [4]. Using that value is the offspring for the next generation of designs chosen using natural selection, cross-over, and mutation [4]. The process ends when the set number of generations is generated, and the most optimal solution is picked [4]. The particle swarm algorithm uses the behaviour of swarms. In the initial step, design solutions (”particles”) get generated randomly inside the feasible boundaries [37]. Then, the best solution is found. The velocity angle to the best solution is found for all other particles, and they move in that direction in the next iteration [37]. The velocity is set for the algorithm, for example, 20 % of the distance between the two solutions [38]. The new position is then evaluated in the next iteration. The process ends after a set number of iterations [37].

Both gradient and evolutionary algorithms have advantages and disadvantages. While the gradient-based algorithms converge faster as they have the gradient information, they are more likely to converge to a locally optimal solution. The result is very dependent on the initial design guess. Also, sensitivity analyses are necessary, making the algorithm complex and costly. Evolution-based algorithms, on the other hand, only

use a finite number of generations, resulting in the possibility of a non-converged solution after the last generation. However, these methods are much simpler, making them more useful when blades are optimized for multiple goals simultaneously, such as costs and weight. [33]

Literature shows that both kinds of algorithms have been successfully used. Hayat et al. and Jureczko et al., for example, used evolutionary genetic algorithms and showed significant weight loss [4][39]. Also, particle swarm evolutionary algorithms showed improvement, which was used in studies by Zhu et al. and Chen et al [1][40]. A gradient-based SLP method used, for example, by Sørensen et al. and Sjølund and Lund and found significant weight loss [34] [29].

In the literature, different design variables were used. Barnes and Morozov found that optimizing thicknesses in each layup region and other additional design parameters like the position of the shear web and the spar width and position helped reduce the mass [41]. They also found that it is beneficial to vary the thickness of the regions over the length of the blade [41]. Hermansen and Lund found that already the optimization of the root section of the blade yields significant weight reduction as it accounts for 60% of the blade mass, emphasizing the importance of the root region for the optimization [42].

Sørensen et al. additionally found that the mass can be reduced even more when also using the material choice in different regions as design variables [34]. They also found a high dependence of the parametrization on the blade when optimizing the materials and thickness. Longitudinal or circular parametrization did not result in higher weight reduction than the grid parametrization, emphasizing the need to optimize the layup in the cross section but also in the blade length [34].

Sørensen et al. additionally found that the thickness discretization significantly impacts the results [34]. Sørensen et al. found that their buckling load factor constraint is violated by 19.3 % after discretizing their successful design after the optimization [34]. They, therefore, conclude that the optimization can only be used as a preliminary result, and thickness discretization is a significant issue in the optimization process [34].

In the process of optimizing a blade, not only is the objective function considered, but also various constraints. Generally, in the optimization frameworks presented above, the structural constraints of stability (buckling), strength (maximum strain criterion), stiffness (maximum tip deflection), and resonance (difference between natural frequencies of the turbine and blade) are considered [4]. Fatigue damage has also been used as a constraint in optimization in the most recent studies [42], [43]. Additionally, manufacturing constraints are applied, considering, for instance, ply drops and through-the-thickness changes [42]. All these constraints must be fulfilled before the optimization can be stopped and called successful.

In this report, optimization will be based on the DTU Wind and Energy Systems devel-

oped tool HAWTOpt2, which was later updated and named AESOpt. It is a gradient-based optimization scheme, and its workflow can be seen in Figure 2.8 [44].

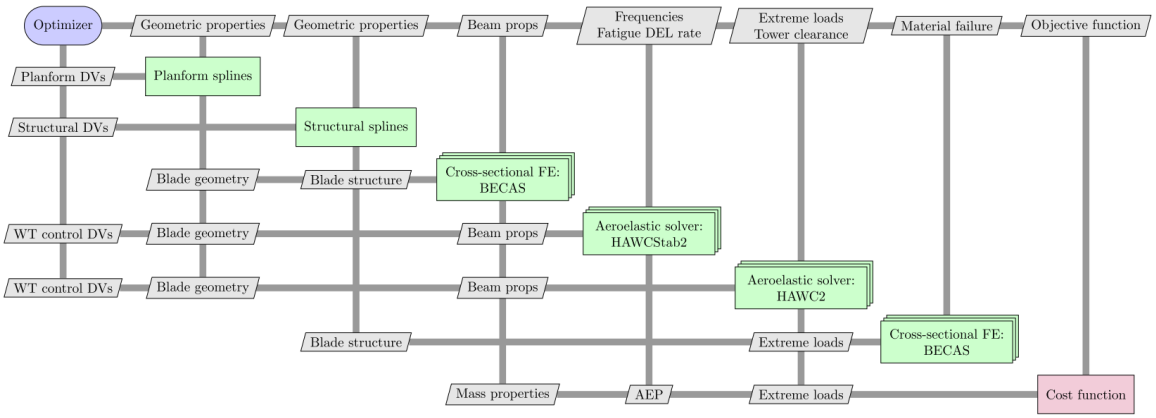

Figure 2.8: HAWTOpt2 framework workflow [44].

This workflow shows the structural and planform optimization of a wind turbine blade with the objective of cost reduction. Planform and structural splines are optimized using the DTU cross-sectional finite element tool BECAS and the aeroelastic solvers HAWC2 and HAWCStab2 [44]. By optimizing the blade using a structural and aerelastic solver, the structural properties as well as the aeroelastic behaviour of the resulting blade can be part of the constraints and objectives of the optimization framework [44].

The literature highlights several strategies for blade weight reduction, emphasizing gradient-based and evolutionary algorithms as two principal approaches. It shows the workflow of the tool AESOpt that will be used in this report. During the optimization, it will be investigated which adjustments are needed to the framework to result in a successful redesign of the OLW934 to be used on the NorZet Ltd E-3120 turbine. Additionally, the results from the literature on design variables and discretization will be investigated in the presented case study.

2.2.4. Structural modeling

The structural modeling used in the optimization methods is usually done using layered shell 3D finite elements to have lower computational efforts than when using solid elements, but still reflect the variance through the thickness [34], [39]–[41]. In the first iterations of the optimization, beam elements can be used efficiently, as well as codes that evaluate beam cross sections [45]. In these tools, the interface planes at the nodes are evaluated [45]. The acting forces can be superimposed onto each cross-section, resulting in smaller finite element models and less computation time [45]. For each cross-section, can the strain and stress state be evaluated and then interpolated [45]. However, this method cannot be used to get the final design because beam models can not predict stability problems, such as buckling. The failure mechanism buckling is, however, as described in subsection 2.2.3, a structural constraint for the optimization problem. Additionally, the accuracy of beam models is very limited close to beam boundaries and to sudden changes in loads or cross-sectional geome-

try [45]. To predict the realistic system behaviour in later iterations, a more advanced finite element analysis of the entire blade is necessary [45].

To use solid cuboid elements, which would yield the most accurate results, a very detailed mesh is necessary [45]. These elements need an exact thickness definition, making it necessary to use very fine meshes [45]. Therefore, these elements are computationally expensive for an iterative approach, and shell elements are used [45]. In comparison, shell elements can also predict the transverse shear stresses distributed through the thickness more realistically [45]. However, shell elements cannot predict the out-of-plane stresses as accurately as solid brick elements [34]. This can be overcome by introducing manufacturing constraints mimicking these stresses [34]. These manufacturing constraints involve combining smaller finite element domains into larger regions to enable manageable variations in thickness and material selection [34]. They also control thickness differences between neighboring regions to prevent delamination and restrict the number of identical layers within the laminate to reduce the risk of matrix cracking [34]. Additional considerations include ensuring laminates are symmetric and balanced to prevent bending-torsion coupling, guaranteeing a minimum amount present of all materials used, and implementing blending rules to regulate changes in fiber orientation in-plane [34].

For the outer shell with a given outer aerodynamic blade, shell elements can be used that are offset by half of the material thickness [45]. No offset is necessary for the spars, and the shell element's mid-plane can coincide with the position of the mid-plane of the spar [45]. Haselbach found, however, that shell elements do not accurately predict the behaviour in the trailing edge region because they do not account for extra stiffness when two elements intersect in the joined region [45]. To overcome this, Haselbach found that a partial discretization of the joint elements at the trailing edge with solid elements solves this discrepancy of stiffness [45]. Linear solid cuboid elements with hourglass control and reduced integration are used to increase the computational time and prevent shear locking (Abaqus type C3D8I) [45]. The rest of the blade is still discretized using thick shell elements with reduced integration (Abaqus type S8R), and the solid elements are tied to their neighboring shell elements [45]. The shell-solid model additionally allows for implementing cohesive elements or surfaces, making a delamination study feasible [45].

The choice of shell element type to use is governed by the need to prevent numerical errors. In FEM simulations, spurious elements must be avoided. Shear locking and hour glassing are two element phenomena, that result in nonphysical predictions of the stiffness and deformations respectively and that should be prevented. Shear locking introduces an overestimation of stiffness in fully integrated first-order elements in bending. The linear element can not follow a curve on its sides, resulting in a shape under bending shown in Figure 2.9a. In a real bend specimen, the dotted lines would stay orthogonal to each other and the outer sides of the element. However, because of the element's linear behaviour, angle A in a bent case is no longer 90°. This introduces artificial shear stress at the element's bottom and top surface, incorrectly increasing its stiffness and resulting in incorrect displacements, stresses, and natural

frequencies. This problem can be fixed by increasing the element's order or using reduced integration. Increasing the order of the elements would result in higher computational time and is, therefore, less attractive. However, using reduced integration in bending results in the numerical problem of hourglassing. In Figure 2.9b, the dotted lines are now orthogonal, but no stresses can be detected under bending when only one integration point is used. This can propagate through the whole structure when a too coarse mesh is used. The structure is, therefore, often predicted to be excessively flexible, and the results are not physical. Hourglassing control is generally provided in finite element analysis codes to still be able to use linear elements with reduced integration. [46]

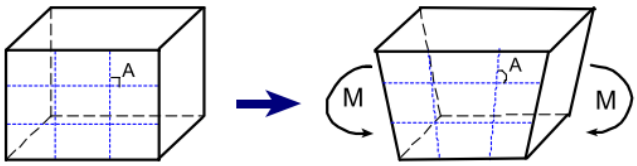

(a) Linear first order element with full integration.

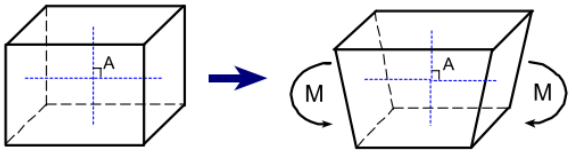

(b) Linear first order element with reduced integration.

Figure 2.9: Effects of a bending load on a linear fully integrated and reduced integrated first-order element. [46]

2.3. Failure causes

Understanding the main failure mechanisms in composite wind turbine blades is crucial for optimizing their design, improving reliability, and reducing maintenance costs. This chapter outlines key failure causes to be aware of in the optimization process.

One primary failure mechanism is buckling. Buckling is a non-linear structural instability that significantly impacts wind turbine blades [2]. It describes the sudden deformation of a thin-walled structure under compressive loading. The trailing and leading edge panels are mainly in danger of experiencing buckling. Carbon fiber usage has been shown to improve buckling resistance, with stacking sequences, such as [90/90/0]s, offering higher critical buckling loads compared to [90/45/0]s, [+-45/0]as, [0/0/90]s, and [+-45/90]s [47]. More plies of the direction +-90°, therefore, increase the buckling strength [47]. Also, introducing a core in the skin and the spar increases the buckling load. The buckling load decreases in the skins as core thickness is reduced, and so does the bending stiffness [47]. The number of layers in the skins of a sandwich structure has a negligible effect on the buckling load resulting from their skinny thickness compared to the core [47]. Introducing a sandwich structure for example in the spar reduces the blade weight while increasing the buckling resistance [48]. This measure can, however, result in less flap-wise stiffness and natural frequency when the number of layers in the sandwich structure's skin is reduced compared to the layup before [48]. Also, a sufficient interface between spar cap and spar has to be ensured

as the interface strength, the shear stiffness of the matrix at the interface, and the interface angle directly affect the buckling resistance of the structure [48]. Another buckling problem is the fatigue failure mechanism of buckling-driven delamination [2]. For this mechanism to appear, initial delamination has to be already apparent [2].

One phenomenon that induces buckling in a wind turbine blade by flattening the spar caps is the Brazier effect [48]. The Brazier effect, characterized by ovalization of the blade's cross-section under bending, reduces bending stiffness and increases the likelihood of unstable failure [48]. This effect is more pronounced in unidirectional 0° ply layups, which exhibit lower failure strains [48]. With a spar cap of fibers mainly in the longitudinal direction, transverse tension failure or interlaminar shear failure between the layers could be the result [2]. Higher stability ply orientations, such as ±60° to 90°, can suppress the Brazier effect, enhancing blade stability and buckling resistance [48]. To maintain stability against bending but increased buckling loads, carbon 0° plies with angled glass fiber plies can be used [48]. Another measure that can be used is to split the spar caps, which increases the flexural rigidity. Lastly, a bending-torsion coupling could be implemented to act as a passive load control [48].

Cross-sectional shear distortion is another critical failure mechanism. This problem increases with the size and weight of the blade, as the increase in the edgewise loads changes the direction of the resulting load vector significantly [2]. Additionally, more flexible blades are in greater danger as the bending stress increases, which would result faster in the failure of a shear-distorted blade section [2]. This mechanism, therefore, needs to be checked for in a new design. The stiffness should be increased if critical.

Fatigue failures are particularly apparent in the root transition area, where large edgewise forces are transferred through curved panels [2]. This region is, therefore, prone to feel out-of-plane deformations and peeling stresses in adhesive bond lines [2]. These factors often result in fatigue failure, especially in trailing-edge adhesive joints [2]. These loads also need to be transferred into the hub. Root end failure is more prone to occur when abrupt, significant geometry changes occur [48]. In the worst case, this could result in a detachment of the blade from the hub [48]. The root area, therefore, needs to be emphasized in the design process by introducing smooth transition areas [48].

Ply drops in composite laminates create local interlaminar stress concentrations, which can lead to delamination [48]. The stress concentrations are higher when multiple plies are dropped at the same location [48]. Thicker laminates and internal ply-drops reduce the stresses [48]. Also, gradual, staggered ply-drop placement helps mitigate this issue [48]. When these are placed between continuous plies and an adhesive layer in the ply drop region is introduced, it reduces the build-up of stress at the ply drop further [48].

Surface damage, including microcracks in coatings and resin or interface defects, is also a common issue for wind turbine blades [48]. Leading-edge erosion further

compromises blade integrity, emphasizing the need for protective coatings and maintenance strategies, but no specific design requirements of the composite [48].

2.3.1. Failure criteria

Except for the surface damage, which should be assessed by inspections in real operation, the other failure mechanisms can be tested in calculations during the design phase using failure criteria.

Failure criteria describe the outer strength or strain envelope that a material can withstand. If the applied loading surpasses it, the failure criteria index shows a resulting number of over 1, and the structure has failed. An index between 0 and 1 shows no failure. Different failure criteria can be used to assess composite structures. This report uses the software Abaqus CAE as a full-blade FEM software and AESOpt to check the failure index of the blade structure. While Abaqus provides four different stress-based failure criteria, Max Stress, Tsai-Wu, Tsai-Hill, and Azzi-Tsai-Hill, and the Max Strain criterion, AESopt is only based on the Max Strain criterion [49]. These five failure indices are presented in this chapter, along with their advantages and disadvantages.

Tsai-Wu Failure Criterion

The polynomial-based Tsai-Wu failure criterion extends traditional isotropic failure theories to anisotropic composite materials and takes into consideration the interaction between various stress components [50]. It is expressed as [49]:

$$I_F = F_1\sigma_{11} + F_2\sigma_{22} + F_{11}\sigma_{11}^2 + F_{22}\sigma_{22}^2 + F_{66}\sigma_{12}^2 + 2F_{12}\sigma_{11}\sigma_{22} < 1.0 \tag{2.1}$$

where σ_{11}, σ_{22} are the normal stresses in the principal material directions, and σ_{12} is the in-plane shear stress. The Tsai-Wu coefficients are [49]:

$$F_1 = \frac{1}{X_t} + \frac{1}{X_c}, \quad F_2 = \frac{1}{Y_t} + \frac{1}{Y_c}, \quad F_{11} = -\frac{1}{X_t X_c}, \quad F_{22} = -\frac{1}{Y_t Y_c}, \quad F_{66} = \frac{1}{S^2}$$

$$F_{12} = \frac{1}{2\sigma_{\text{biax}}^2}\left[1 - \left(\frac{1}{X_t} + \frac{1}{X_c} + \frac{1}{Y_t} + \frac{1}{Y_c}\right)\sigma_{\text{biax}} + \left(\frac{1}{X_t X_c} + \frac{1}{Y_t Y_c}\right)\sigma_{\text{biax}}^2\right]$$

or

$$F_{12} = \overset{*}{f}\sqrt{F_{11}F_{22}},$$

when the equibiaxial stress at failure σ_{biax} is not known [49]. For $\overset{*}{f}$ is the default value zero, where $-1.0 \leq \overset{*}{f} \leq 1.0$ [49].

Tsai-Hill and Azzi-Tsai-Hill Failure Criterion

The Tsai-Hill criterion provides a simpler form than Tsai-Wu [49]:

$$I_F = \frac{\sigma_{11}^2}{X^2} - \frac{\sigma_{11}\sigma_{22}}{X^2} + \frac{\sigma_{22}^2}{Y^2} + \frac{\sigma_{12}^2}{S^2} < 1.0. \tag{2.2}$$

The Azzi-Tsai-Hill criterion has almost the same definition as the Tsai-Hill criterion [49]. Just the absolute value of second term is taken, which only has an effect when σ_{11} and

σ_{22} have opposite signs [49]. This version is thus the modified Tsai-Hill criterion for orthotropic composite materials [50]. It is defined as [49]:

$$I_F = \frac{\sigma_{11}^2}{X^2} - \frac{|\sigma_{11}\sigma_{22}|}{X^2} + \frac{\sigma_{22}^2}{Y^2} + \frac{\sigma_{12}^2}{S^2} < 1.0. \tag{2.3}$$

where X and Y are the strengths in the 1 and 2 directions, and S is the in-plane shear strength.

Maximum Stress Criterion

This criterion assumes failure, when any stress component is higher than its strength in the corresponding direction [49]:

$$I_F = \max\left(\frac{\sigma_{11}}{X}, \frac{\sigma_{22}}{Y}, \left|\frac{\sigma_{12}}{S}\right|\right) < 1.0 \tag{2.4}$$

Maximum Strain Criterion

The maximum strain criterion is defined similary [49]:

$$I_F = \max\left(\frac{\varepsilon_{11}}{X_\varepsilon}, \frac{\varepsilon_{22}}{Y_\varepsilon}, \left|\frac{\varepsilon_{12}}{S_\varepsilon}\right|\right) < 1.0 \tag{2.5}$$

where X_ε, Y_ε, S_ε are the allowable strains.

The envelopes of the four different criteria can be seen in Figure 2.10. They all have the same values on the axes, as they are all based on the maximum strength values of the material in tensile and compressive loading in both the fiber and transverse direction.

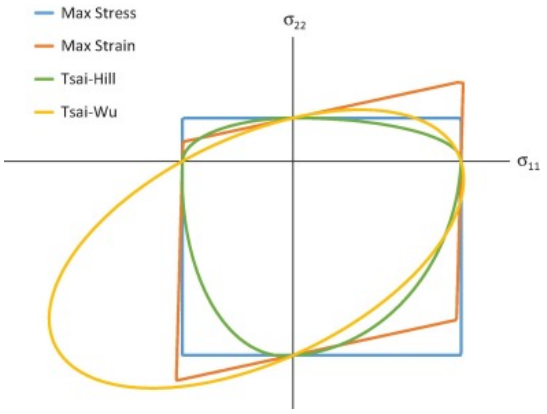

Figure 2.10: Envelopes of different failure indeces [51].

The differences are in the areas between those points. Table 2.1 shows the advantages and disadvantages of the different failure criteria.

Table 2.1: Comparison of Failure Criteria for Composite Materials [50].

Criterion	Advantages	Disadvantages
Tsai-Wu	• Considers the combined influence of multiple stress components • Can be applied to a wide range of loading scenarios	• Requires a relatively large number of material constants • More complicated to formulate and use
Tsai-Hill/ Azzi-Tsai-Hill	• Less complex than the Tsai-Wu model • Useful for quick, preliminary evaluations	• Reduced accuracy for complex stress conditions • No differentiation between tensile and compressive strength values
Maximum Stress	• Very straightforward and simple to apply • Needs only few material properties	• No interaction between different stress components • Results that are too conservative
Maximum Strain	• Easy to implement • Works well when strain limit values are clearly defined	• No influence of combined strain components • When complex loading has low accuracy

The literature comprehensively identifies key failure mechanisms, including buckling, shear distortion, and fatigue failures, as well as failure criteria to assess the blades' performance during the design process. These failure mechanisms, except for the environmental degradation, should be checked in the original design and also in the redesign. Based on how high the failure index of the blade is in different regions, regions with high improvement potentials can be identified, and critical regions with high failure index values close to or above 1 should be found and addressed.

2.4. Loads and frequency issues

Wind turbine blades' operational performance and longevity depend significantly on their ability to withstand various loads and their interaction with the blade's natural frequencies. Proper load distribution and frequency management are critical to avoid catastrophic failures such as resonance, excessive vibration, and structural fatigue. This chapter shows the loads and frequency issues a wind turbine blade can experience and measures to prevent them.

2.4.1. Loads

Wind turbine blades experience complex loading conditions throughout their lifecycle, arising from environmental, operational, and design-specific factors [52]. The forces integrate along the blade span to produce bending and torsion loads [52]. These loads induce internal stresses and strains, causing alteration of the blade's shape [52]. Dangerous for a blade's integrity are ultimate loads and fatigue loads accumulating over its lifetime. The loads can be classified into several categories:

Gravitational and inertial forces act continuously on the blades [53]. At standstill, they are static; when in operation, however, the gravitational and inertial loads are cyclic as the blade rotates in the gravity field [53]. Inertia forces can get very high at abrupt stops of the turbine, resulting in this being a critical load case to consider [52].

Aerodynamic forces result from airflow interaction with the stationary and moving parts of wind turbines [53]. These loads are influenced by the average wind speed and the atmosphere's turbulence level [53]. Aerodynamic loads include lift and drag forces acting at the aerodynamic center of the blade, resulting in in-plane driving forces, out-of-plane thrust forces, and torsional moments that contribute to blade deformation [52]. Additionally, wake loads caused by the turbulent air behind the blades can further impact blade performance [53].

Actuation loads occur during the operation and control of wind turbines [53]. For instance, pitching the blade from a full-load operation toward a feathered position at high speeds can generate a large flapwise load in the upwind direction [53]. This is opposite to the expected bending loads for the blade during regular operation and poses significant risks to its structural integrity. This load case should, therefore, be considered in terms of the ultimate limit state [52].

Additional loads that wind turbine blades may encounter include impact loads from debris or objects hitting the blades, tower loads resulting in vortex-induced vibrations, and other environmental loads that contribute to long-term degradation like ice [53]. Also, in transportation and installation, various loads are possible [53].

Cyclic loads can be detrimental to the wind turbine blades when their frequency coincides with the natural frequency of the blade [52]. Cyclic loading can result from gravity, aerodynamic variations, and blade-passing effects [52]. As explained, gravity causes a sinusoidal in-plane blade root moment as the blade rotates. Also, when the blade passes through the tower wake, it results in sudden drops in aerodynamic forces, inducing a cyclic loading every rotation [52]. As the wind shear results in higher wind speeds at the top of the turbine and lower ones at the bottom, the blade has different aerodynamics per rotation. Also, dynamic stall effects can induce cyclic loading, bringing the structure closer to resonance instability when the aerodynamic forces provide negative damping [52]. Because the blade experiences cyclic loading every rotation, it is the most critical excitation frequency 1P [52]. Less energetic, higher multiples of these frequencies are less significant but should still be analyzed when close to a natural frequency of the blade [52]. For the tower of a wind turbine blade, 3P and its

higher multiples and the 1P frequency are excitation frequencies [52]. The full turbine system experiences the cyclic loads from the blades three times per rotation. The 1P frequency is significant when there is an imbalance in the rotor.

2.4.2. Resonance

One critical design consideration is the avoidance of resonance, which occurs when a poorly damped natural frequency of a blade coincides with the frequency of one of its exciting forces. This can be checked using an aeroelastic Campbell diagram. It consists of a frequency versus wind speed and a damping ratio versus wind speed plot, as shown in Figure 2.11. The first plot of an aeroelastic Campbell diagram usually contains the turbines and blades' natural frequencies and the excitation frequencies plotted against the rotor or wind speed. The second plot shows the damping ratios of the motions plotted over the rotor or wind speed. For the design of a blade, the intersections between the blade's natural frequencies and the excitation frequencies in 1 to 3P in the first plot are the relevant dangerous spots [52]. Resonance only appears when the dangerous natural frequency is poorly damped in the damping ratio plot. Flapwise motions are generally damped higher than edgewise because the blade experiences aerodynamic damping. Resonance can lead to large amplitude oscillations and potential structural damage. Modal analysis helps characterize the vibration mode shapes and provides frequency criteria to ensure safe operation [54]. For instance, maintaining a frequency ratio $\frac{f_{excitation}}{f_{0,n}} \leq 0.95$ is often acceptable [54].

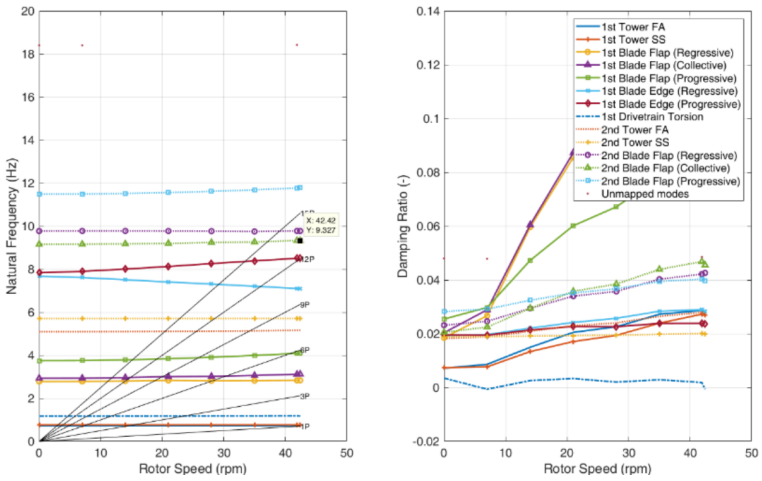

Figure 2.11: Example Aeroelastic Campbell diagram. [55]

Therefore, the blade's natural frequency is an important design parameter. When changing the blades' mass, the tower's natural frequencies can also be affected, which should be compared to 1P and 3P and its higher multiples in the Campbell diagram [52]. Boudounit et al. followed that in deciding what spar to use in their design [16]. They decided on a box girder structure, resulting in a blade natural frequency farthest from the excitation frequencies [16]. Another measure to alter the natural frequency of the blade is called frequency placement [54]. This method uses lumped masses along the blade and the variation of blade thickness to alter the natural frequency [54]. Strategic mass and stiffness modifications can also change the mode shapes of the

vibrating structure [54]. This process is called ‘‘modal shaping’’ or ‘‘modal tailoring’’ [54]. High frequencies are a result of high stiffness in comparison to low mass. High natural frequencies are, therefore, the goal because they reduce the steady state and transient response of an excited structure [54]. To compute the natural frequencies, the eigenvalue problem

$$[\mathrm{M}]\ddot{\boldsymbol{x}} + [\mathrm{C}]\dot{\boldsymbol{x}} + [\mathrm{K}]\boldsymbol{x} = 0 \tag{2.6}$$

needs to be solved for the blade and the full turbine [56].

Other strategies to prevent resonance next to modifying the natural frequencies are load management using stall or pitch control and extra parts to reduce flow separation and resulting flow fluctuations like Vortex generators [52]. Aeroelastic tailoring can also be used. Aeroelastic tailoring is essential in mitigating aeroelastic instabilities [52]. It is a passive load control. The offset between a blade’s aerodynamic and shear center induces a twisting motion under aerodynamic thrust [52]. While the blade is bending with increasing loads, the angle of attack gets reduced, reducing the aerodynamic force and, therefore, helping with the system’s stability [52]. However, it risks introducing flutter, a destructive instability where aerodynamic forces amplify natural vibrations [52].

The literature provides a detailed categorization of load types, offering valuable insights into their individual impacts on blade performance. Discussions about the effects of gravity, aerodynamic forces, and actuation loads are comprehensive and well-supported. For the NorZet Ltd turbine using the original blade, these loads should be investigated, and the aeroelastic stability should be checked to validate the safe operation of the turbine. The same loads and excitation frequencies should then be used to constrain the optimization process.

2.5. Design Loads and Life Assessment

In the iteration process described in subsection 2.2.3, the step to assess whether the design is complete is the assessment of the blade’s structural integrity [11]. For normal design situations, extreme loads, fault design situations, and transportation, installation, and maintenance design load cases should be analyzed [53]. When using design load cases, including enough critical loading directions and the number of blade elements along the span is essential. The concrete numbers are in the IEC 61400-5 standard [11]. Four primary analyses must be made to assess the blade: ultimate strength analysis, fatigue failure, stability, and critical deflection analysis [53]. These should be done for defined design load cases in the IEC 61400-1 standard [53].

2.5.1. Ultimate strength analysis

The structure should be tested against relevant failure modes in ultimate load cases [11]. An ultimate failure could result in fiber, inter-fiber-failure, inter-laminar failure, delamination, or debonding at interfaces between different laminae, adhesives, or core materials [11]. The ultimate strength is calculated using characteristic loads and resistance [11]. These loads are predicted to occur at a specific probability [53]. According to IEC 61400-1, the characteristic load can be calculated in three different ways de-

pending on the load channel to be calculated [53]. In all cases, the data used in the analysis is an at least 10-minute-long turbine simulation for multiple wind speeds, where the extreme values are analyzed [53]. The specific load cases can be seen in the IEC 61400-1. The characteristic resistance has, per default, a 95 % probability that the real one is higher with a 95 % confidence level [11]. To get the design loads, the characteristic loads and resistance get multiplied with partial safety factors [11]. The load gets multiplied with partial safety factors for loads y_f and the characteristic resistance with a material partial safety factor y_m [11]. A safety factor for consequences of failure y_n is also added, either as an increase in design response from the design load or a decrease in design resistance [11]. The design response cannot exceed the design resistance [11].

The partial safety factor for materials is defined in the IEC 61400-5 standard as [11]:

$$\gamma_m = \gamma_{m,0}\gamma_{m,1}\gamma_{m,2}\gamma_{m,3}\gamma_{m,4}\gamma_{m,5} \tag{2.7}$$

with the base material safety factor $\gamma_{m,0}$ and the factors for environmental degradation $\gamma_{m,1}$, for temperature effects $\gamma_{m,2}$, for manufacturing effects $\gamma_{m,3}$, for calculation accuracy and validity of the method, and for load characterization [11].

The partial safety factors for loads y_f and for consequences of failure y_n are defined in the IEC 61400-1 design standard. The partial safety factor for loads depends on the load case to be analysed. It is 1.35 for normal operation load cases; it can be reduced to 1.1 in abnormal load cases [11]. Additionally, there are some exceptions for specific load cases mentioned in [11]. When analyzing the loads on a blade, a lot of different load cases should be checked, and the highest one should be used as the limit for the design.

y_n can be 0.9, 1, or 1.2, depending on the part of the turbine that is designed [11]. Class 1 with $y_n = 0.9$ are 'fail-safe' components, which describe components, which when they fail, do not correlate with the failure of a main part of the turbine [11]. Class 2 with $y_n = 1$ are components that have as a result the failure of a main part [11]. Lastly, class 3 parts link actuators and brakes to the turbine's structure for essential safety functions without backups [11].

2.5.2. Fatigue failure

Compared to the ultimate strength failure, fatigue failure is caused by numerous small loading cycles that gradually degrade the structure. These are analyzed using equivalent fatigue loads found using rain flow counting from 10-minute time-series data [52]. The 10-minute equivalent fatigue can then be combined to the lifetime equivalent fatigue load using Equation 2.8.

$$L_{\mathsf{eq}} = \left[\frac{\int R_{\mathsf{eq}}(U)^m n_{\mathsf{eq}} p(U) n_{\mathsf{T}}\, dU}{n_{\mathsf{eq,L}}}\right]^{1/m} \tag{2.8}$$

with the 10-minute equivalent fatigue loads R_{eq}, the Wöhler exponent m, the number of cycles in the lifetime $n_{eq,L} \approx 10^6$, the number of data series n_{eq}, the wind speed

probability $p(U)$, and the amount of total lifetime short term periods n_T, when using 1 Hz $n_T = 20{*}365{*}24{*}60{*}60\ (\mathrm{sec})$ [57]. The lifetime equivalent fatigue load corresponds to the total damage by Equation 2.9.

$$D_L = n_{\mathsf{eq,L}} L_{\mathsf{eq}}^m \tag{2.9}$$

The total damage can therefore be calculated from Equation 2.10.

$$D_L = \int R_{\mathsf{eq}}(U)^m n_{\mathsf{eq}} p(U) n_{\mathsf{r}}\, dU \tag{2.10}$$

The partial safety factor for fatigue loads is $y_f = 1.0$ [53]. The same material y_m and consequences of failure safety factor values y_n are used as in the ultimate strength analysis [53].

2.5.3. Stability

No buckling is allowed to occur in the load-carrying ”non-fail-safe” parts of the blade [53]. In the other parts, buckling is acceptable when the load is higher than the characteristic load [53]. The design load uses the same partial safety factor y_f as in the ultimate strength analysis calculation [53].

2.5.4. Critical deflection analysis

For critical deflection analysis, the combined safety factor, $\gamma_f \gamma_n \gamma_m$, needs to be at least 1.15 [53]. Next to the requirement that the design resistance has to be bigger than the design load, another necessary verification is that the tower clearance of the deflected blade is bigger than the undeflected position clearance times the ratio shown in Equation 2.11 [53].

$$y_{tc} = y_{tc,undeflected} \cdot \frac{\gamma_f \gamma_n \gamma_m - 1}{\gamma_f \gamma_n \gamma_m} \tag{2.11}$$

For all tests applies when the magnitude of loads was determined by physical tests prior, a lower partial safety factor for the load can be used [53]. When no failure occurs, the design is completed if no other optimizations are desired.

The reviewed standards and procedures for life assessment provide a solid framework for design validation. This will be used to constrain the design variables in the optimization and check the blade designs for failure during operation.

2.6. Research objectives

The reviewed literature offers a solid foundation for understanding wind turbine blade design, optimization, and validation processes. However, significant gaps remain, particularly in the exploration of strategies to reduce blade weight without compromising structural integrity. These gaps underscore the need for a comprehensive investigation into how advanced material distributions, smart ply lay-up strategies, and optimized structural concepts can contribute to the development of more efficient blade designs.

A key gap lies in the limited exploration of the advantages and disadvantages of structural concepts like the use of different spar designs. There is insufficient research on which approach could achieve greater weight efficiency while maintaining or improving structural performance. The potential of selective material placement and strategic lay-ups for enhancing load-bearing capacity and stiffness without increasing weight is also underexplored. The interaction between structural changes and the aeroelastic behaviour of the blade also remains insufficiently addressed. Ensuring that a lighter blade maintains stability under operational conditions and avoids resonance issues is critical for safe and robust turbine operation. The literature provides limited guidance on how design adjustments might mitigate these risks.

These gaps collectively highlight the need for this project's main research question: How can the weight of a rotor blade be reduced while maintaining the integrity of the structure? To answer this, the following questions will be investigated, which can be answered with their connected sub-questions:

- How is the performance, structural, and aeroelastic of the original design?
  - Which regions of the blade have optimization potential?
  - Which regions of the blade need reinforcement?
  - How is the aeroelastic behaviour of the turbine with the original blade?
- What are the most significant weight drivers in the design?
  - What different structural concept could be lighter, for instance, shear webs instead of a box design?
  - What are more optimal, less heavy materials and ply lay-ups?
  - In which sections of the blade can the highest weight reduction be achieved?
- What can be done to address the weight drivers?
  - What improvement could be accomplished by changing the internal structure?
  - What improvement could be accomplished by changing the lay-ups and material regions?
  - What adjustments are needed to how the AESOpt optimization framework is used in this report to result in an optimized design?
  - What design variables and constraints are needed in the framework?
- What are the effects of the redesign on the aeroelastic behaviour and the stability of the rotor blade and turbine?
  - How does the redesign behave with respect to resonance, and what potential adjustments are needed?
  - How does the redesign withstand its aeroelastic loads?
  - How are the loads and aeroelastic stability influenced by the internal structure?

Part 1: Current blade OLW934

The current blade OLW934 from Olsen Wings A/S is the basis of the structural and aeroelastic optimization in this project. The real-life blade planform can be seen in Figure 2.12. It is 9.34 m long and consists of four main parts. The blade is made in a box girder configuration using a pressure side beam, a suction side beam, and two outer shells. They are manufactured individually and joint adhesively. The configuration to be analyzed in this report additionally has a tip-break installed.

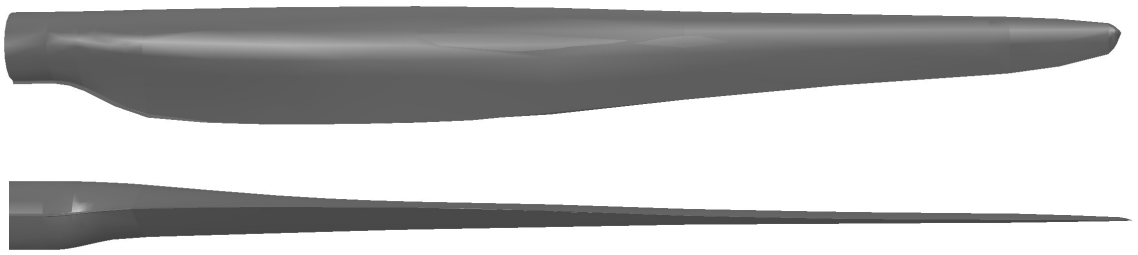

Figure 2.12: Blade OLW934.

3 Methodology

To optimize the blade, resulting in a weight reduction, is the first part of this project, a digital recreation of the currently existing blade OLW934 and the E-3120 turbine with NorZet redesigns. This is used as a starting point for the optimization and for comparison of the resulting design in the second part of the project. In Figure 3.1, the workflow of the first part is shown. First, the blade is numerically modeled in the FEM-software Abaqus. This model is used to generate a structural input file of the blade for the following HAWCStab2 setup and simulation. HAWCStab2 is a steady-state aeroelastic solver. It results in flapwise and edgewise bending moments, which are imposed on the FEM-model in order to check for the stresses and deflection of the blade. Also, it allows for the analysis of the failure index of the structure, showing the improvement potential of the original blade.

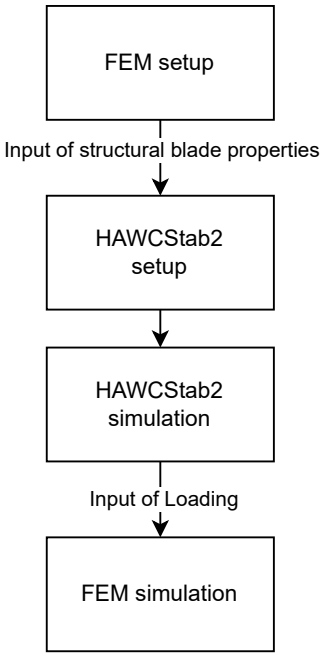

Figure 3.1: Work flow of the analysis of the existing blade OLW934.

3.1. FEM Setup

A detailed Finite Element Model is necessary to investigate the eigenfrequencies, stresses, strains, and the failure index of the original OLW934 blade over the blade span. This is done using Abaqus CAE.

3.1.1. Blade Planform

The model is created based on the airfoil distribution from the OLW965 blade previously designed by DTU. The current blade OLW934 was designed by Olsen Wings A/S for production using those airfoils, but with reduced spacing between the airfoil sections in the tip region. The OLW965 and OLW934 blades are identical until the tip cut at 8.04 m. The airfoils in the tip were then found by proportionally reducing the spacing of the airfoils in the tip region to fit in 1.3 m instead of 1.61 m. The process is shown in Figure 3.2.

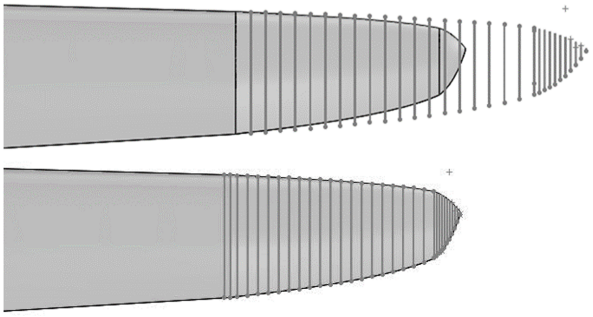

Figure 3.2: OLW934 tip region, developed from OLW965 [6].

The same method is used in this report. The blade planform for the FEM-model is found by altering an Excel file containing the cross-sectional geometry for the OLW965 to have the correct cross-section spacing. The inner blade part, until the tip cut, is kept the same, and the z-positions of the outer cross sections are proportionally reduced to result in a blade of length 9.2325 m. The missing length of 0.1075 m is added in a later step with the blade's tip, imported from CAD, to close the blade. Additionally, a new hub radius is used in the Excel file, as in the newly installed rotors of NorZet, a new hub is installed.

Using Python scripts, the cross sections are imported into Abaqus CAE in the next step to build up the blade as a shell geometry. The Excel file is used as an input, generating 2D cross-section geometry at different planes along the blade span. These cross sections are connected using the Shell Loft Feature in Abaqus. Because the described model of the OLW965 blade did not include the correct tip geometry, the tip is imported into Abaqus CAE from a CAD model of the new OLW934 blade as an additional part. The additional part was used instead of a kinematic coupling constraint and added mass to resemble the outer geometry most realistically, because it gets imported later into HAWCStab2, where the blades' length would influence the loads and power output of the turbine. The resulting blade shell and the imported tip get assembled, and the adjacent surfaces get tied with a tie constraint. This completes the outer shell of the blade, as can be seen in Figure 3.3a.

Figure 3.3b shows a zoomed-in section of the tip region. It can be seen that the form of the imported tip from the CAD model does not exactly match the tip section of the blade part. Its chord and thickness are slightly bigger. This error is a result of the scaling of the tip section of the blade part. In the following, this model will be used to create cross sections to be imported into HAWC2 and to do a stress and failure analysis. For both these applications, this error will only have a marginal effect. For HAWC2, only cross sections on the main blade part are used, and in the failure and stress analysis, no high values are expected in the tip part region. The error, therefore, does not need to be considered.

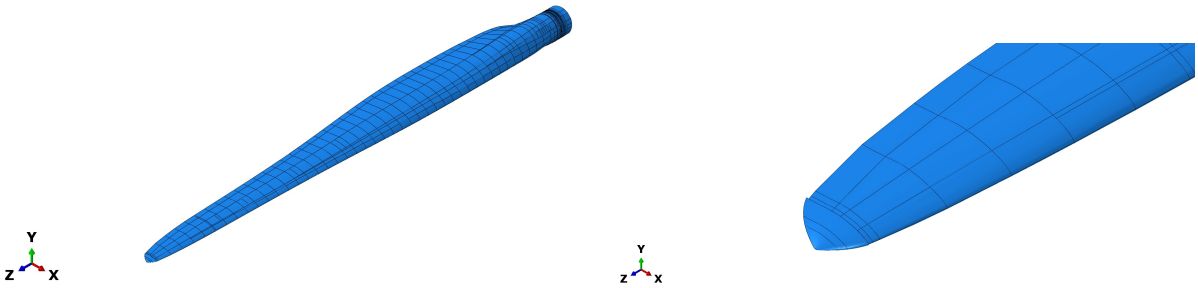

(a) Outer shell of OLW934 implemented in Abaqus.

(b) Tip section of the assembly.

Figure 3.3: Blade form.

Next, shear webs are introduced in the blade part. Even though it would be more exact to model the FEM-model with a box girder structure and the same parts used in real life, in this framework, the structure is converted to a shear web design to make the optimization and analysis easier; hence, the tools are made for this kind of blade representation. This is necessary as the preprocessor code Shellexpander is used to convert between an Abaqus and a cross-sectional FEM model in BECAS in the next phase. This tool requires the cross sections to be connected sets of elements in only one part. It would require a lot of modification to use the box girder design utilizing multiple parts. Additionally, a shear web design is expected to result in a higher weight reduction because its lay-up is more effective, and less adhesive is necessary in the assembly process.

To simplify the model, no tip break is included during this project. The tip break, however, alters the behaviour of the blade significantly, especially in the tip cut region. A decision was made against truncating the blade at the tip cut and including the tip as a dead mass. This measure would have been sufficient for the structural design, because this area will be excluded from the optimization. However, for a good representation of the natural frequency and because this blade will be exported into the aeroelastic solver HAWCStab2, which calculates the loads and power output of the turbine based on the blade's length, this option is disregarded. Instead, to most accurately resemble the original blade, the following design decisions are made:

- The spar cap is stopped as in real life at the tip cut position, to resemble the correct weight and stiffness distribution over the blade.

- The shear webs are introduced, starting where the webs also start in the box girder and are continued over the whole length of the blade, even though the box girder stops at the tip cut, in reality, to reflect real-life behaviour as closely as possible. Because in real life, there is a tip-cut at this z-position, there is no stress transfer over the blade shell in this region. When stopping both the spar caps and the shear webs here, it would result in a non-realistic stress concentration impacting the results of the blade. Additionally, the tip region is, in reality, extra reinforced with the cross-sectional walls of the two parts, the tip break construction itself, and foam to strengthen this area, as can be seen in Figure 3.4.

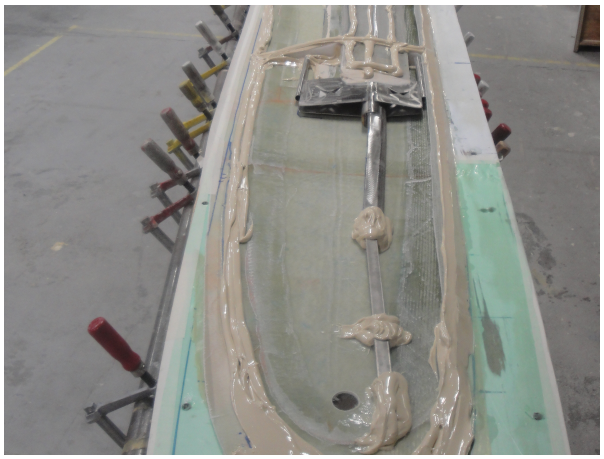

Figure 3.4: Tip break of OLW934 in reality [6].

The introduced shear webs can be seen in a view from the root in Figure 3.5a. The form at the start of the shear webs is simplified to a straight vertical line, as shown in Figure 3.5a. In reality, there is usually a gradual introduction of the shear webs to prevent stiffness jumps, which could result in unrealistic stress concentrations in the area where the spar caps start. That is also the case in the original OLW934 blade, as can be seen in Figure 3.5b. Figure 3.5b shows the root part of the box girder that gets glued into the outer skin in the original OLW934 design.

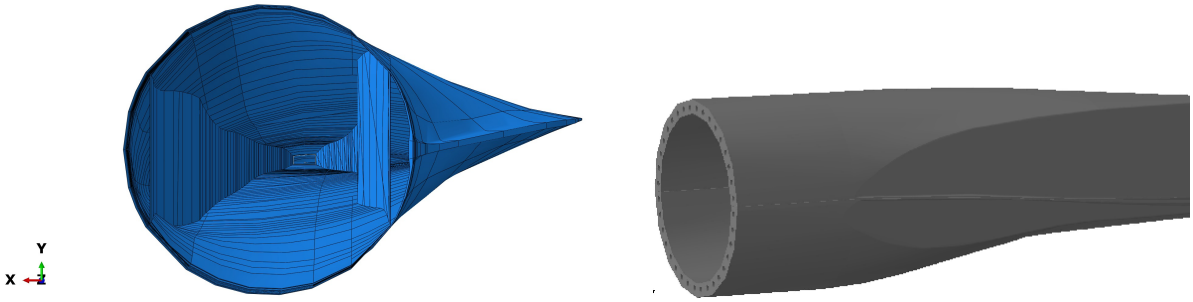

(a) Blade form root view.

(b) Box girder root section OLW934 [6].

Figure 3.5: Modelled internal structure of the OLW934 blade and original box girder design in reality.

3.1.2. Materials and Layup

The materials used in the layup of the blade are defined next. The stiffness and Poisson ratio values used for the UD, Biax, Triax, Chopped Strand Mat (CSM), and Chopped Fiber Mat (CFM) materials are the same materials as used in the 9.65 m blade design made by DTU Wind and Energy Systems. This was done because Olsen Wings A/S uses the same materials in the two blades. They are shown in Table 3.1. The engineering constants of the Chopped Fiber Mat are, in this project, assumed to be the same as the ones for the Chopped Strand Mat. This is approximately true, as the Chopped Fiber Mat ply consists of CSM for 83.44 % of its areal weight. 16.56% is a polypropylene core, which is only 0.13 mm thick in each ply.

Table 3.1: Engineering constants used for OLW934 blade for the different plies with unsaturated polyester resin matrix.

Material	UD 1200	UD 600	Biax	Triax	Soric TF	Soric XF	CSM/ CFM
E_{11} [GPa]	37.8	37.8	9.55	18.70	1.50	0.80	16.10
E_{22} [GPa]	11.10	11.10	9.55	10.90	1.50	0.80	16.10
E_{33} [GPa]	9.87	9.87	9.83	9.62	1.50	0.80	9.17
ν_{12} [-]	0.24	0.24	0.62	0.55	0.30	0.30	0.32
ν_{23} [-]	0.47	0.47	0.18	0.34	0.30	0.30	0.33
ν_{31} [-]	0.08	0.08	0.19	0.01	0.30	0.30	0.19
G_{12} [GPa]	3.27	3.27	10.10	7.72	0.03	0.04	6.09
G_{23} [GPa]	3.23	3.23	2.90	2.89	0.58	0.31	2.69
G_{31} [GPa]	3.27	3.27	2.90	2.92	0.03	0.04	2.69
ρ [kg/m^3]	1850	1850	1780	1780	700	700	1740
X_{t1} [MPa]	762.79	699.51	406.91	443.31	30	18	70
X_{t2} [MPa]	33.18	42.63	406.91	73.33	30	18	70
X_{c1} [MPa]	534	489.66	285	310	45	25	84
X_{c2} [MPa]	38.40	42.63	285	73.33	45	25	84
S [MPa]	28.91	39.55	100.73	69.48	7	3.5	48.3

Next to the definition of the stiffnesses and Poisson ratios, also the definition of the failure strength is important to be able to check for failure in the blade. The failure stresses are collected using test data from Olsen Wings A/S and from comparable materials data from literature [58]. Most data can only be found for epoxy-impregnated laminates. In ”Materials Science and Engineering (9th edition)” the tensile strength of a polyester UD laminate and an epoxy UD laminate are reported to be 1020 MPa and 700 MPa [59]. With $1020/700 \approx 0.7$, 0.7 is used as a conversion factor between laminates with those two different resins [59]. As a base, the data found in ”Ultimate Strength of Wind Turbine Blades under Multiaxial Loading” from P. U. Haselbach was used. This was compared to the tested values of Olsen Wings A/S. When tested data exists that data is used, as it reflects the actual material used best. Because the UD, Biax, and Triax materials reported by P. U. Haselbach have smaller tensile strength values than found in Olsen Wings tests, for these materials, the values were increased to the tested values. The compressive strength was approximated to be 0.7 times the

tensile strength in the Olsen Wings testing series. This assumption was made based on a comparison between different strength data in the fiber direction in the literature, and is also used in this report in the fiber direction.

In the transverse direction, the compressive strength is governed by the matrix behaviour, which has a higher compressive strength than tensile strength. For the UD 1200 material, this strength is found by using the rule of mixtures [60]. Assuming the fibers do not contribute to the transverse strength, $\sigma_f = 0$ is assumed, resulting in the equation shown in Equation 3.1 [60]:

$$X = V_f \cdot \sigma_f + V_m \cdot \sigma_m = 0 + V_m \cdot \sigma_m \tag{3.1}$$

Using the compressive strength of polyester resin, which is 80 to 100 MPa, and an assumed fiber volume fraction of 0.52, a lower bound of the strength of 38.4 MPa is calculated and used in this report [61].

Due to a lack of data on the strength of the Soric TF and Soric XF core materials, they were also approximated using the rule of mixtures. The flexural modulus was reported in the data sheet to be 1.5 and 0.8 GPa. This is approximated to be the Young's modulus in this project. Unsaturated polyester resin has a Young's modulus of 2-3 GPa [61]. When assuming the Soric foam material does not contribute to the stiffness, the percentage of resin in the material can be calculated from the rule of mixtures in Equation 3.2 [60]:

$$E_c = V_{honeycomb} E_{honeycomb} + V_m E_m \tag{3.2}$$

With $E_{honeycomb} = 0$, the percentage of matrix in the material $V_m = E_c / E_m$ is about 50% for the Soric TF material and 25% for the Soric XF material. Using these, the strength of the plies can be calculated from the strength of the unsaturated polyester matrix, which is 50 to 70 MPa for tensile loading and 80 to 100 MPa in compressive loading with Equation 3.3 [60][61].

$$X = V_{honeycomb} \cdot \sigma_{honeycomb} + V_m \cdot \sigma_m = 0 + V_m \cdot \sigma_m \tag{3.3}$$

To be conservative, the minimum bounds of the strength are used, resulting in the values in Table 3.2. Because the honeycomb structure also has a small effect on the strength, all strength parameters are increased by about 5 MPa. These values are used in the FEM-model.

Table 3.2: Strength parameters Soric TF and Soric XF.

Material	X_t	X_c	$X_{t,final}$	$X_{c,final}$
Soric TF [MPa]	25	40	30	45
Soric XF [MPa]	12.5	20	18	25

Lastly, the strength values for the Chopped Strand Mat and, thus, also the Chopped Fiber Mat in Table 3.1 are found. In "Composite Materials, Science and Engineering (Fourth Edition)", strength values for Chopped Strand Mat with epoxy are found [62].

These are, as explained above, multiplied by 0.7 to get realistic values with polyester resin, which results in the documented values in Table 3.1.

As explained in subsection 2.5.1, partial material safety factors are used to reduce the material strength and ensure a safe operation of the designed blade. The partial safety factors for the material γ_m in this project are calculated using the IEC 61400-5 standard, where γ_m is defined as in Equation 2.7 [11]. For this project, the partial material safety factors used are shown in Table 3.3.

Table 3.3: Material partial safety factors [11].

	$\gamma_{m,0}$	$\gamma_{m,1}$	$\gamma_{m,2}$	$\gamma_{m,3}$	$\gamma_{m,4}$	$\gamma_{m,5}$	γ_m
Laminate ultimate strength σ_1	1.2	1.2	1.1	1.3	1.2	1.2	2.965
Inter fibre failure σ_2, τ	1.2	1.0	1.1	1.1	1.1	1.1	1.757
Sandwich core ultimate strength	1.2	1.1	1.2	1.3	1.35	1.2	3.336

In the longitudinal direction for UD1200 and UD600, and in both directions for Biax and Triax, the values given by the standard for laminate ultimate strength are used. In the transverse direction for the two UD materials, the material's partial safety factor for inter-fiber failure is used. Because for the Chopped Strand Mat and the Chopped Fiber Mat, in both directions, mainly the matrix is responsible for the strength, for these, the partial safety factor for inter-fiber failure is used for all strength values. Lastly, for the two core materials, a specific partial safety factor is calculated, shown in Table 3.3, which is used for all strength values.

These values for the different partial safety factors $\gamma_{m,1}$ to $\gamma_{m,1}$ are found from the IEC 61400-5. For $\gamma_{m,1}$, $\gamma_{m,2}$, and $\gamma_{m,3}$ are the shown values used because no effects of environmental degradation, of extreme temperatures, and of manufacturing tolerances were taken into account in the determination of the strength values [11]. Additionally, no validation of the strain calculation was done, and 4 main load directions will be tested in this project, resulting in the above values for $\gamma_{m,4}$ and $\gamma_{m,5}$ [11]. The base material safety factor used is $\gamma_{m,0} = 1.2$ to cover other uncertainties. Also, $\gamma_{m,0} \cdot \gamma_n = 1.2$ is defined in IEC 61400-5, resulting in $\gamma_{m,0} = 1.2$ with a safety factor for consequence of failure defined in section 3.3 of $\gamma_n = 1$ [11]. This results in a material partial safety factor $\gamma_m = 2.95$, by which all strength values in Table 3.1 are divided.

The thickness of the plies is calculated using Equation 3.1.2 with the materials area weight, a glass fiber density of 2600 kg/m^3, and an approximated fiber volume fraction of $v_{f,est} = 0.52$ [63].

$$t_c = \frac{Area\,weight_{fiber}}{\rho_{fiber} \cdot v_{f,est}} \tag{3.4}$$

The resulting thicknesses are shown in Table 3.4. The thickness of the core materials was given in the layup and applied accordingly in the FEM-model.

Table 3.4: Calculated ply thicknesses.

Material	UD 1200	UD 600	Biax	Triax	CSM	CFM
Areal weight [g/m^2]	1182	640	610	933	450	1087
Thickness [mm]	0.95	0.5	0.5	0.7	0.33	0.96

Using these materials, the layup of the blade was implemented. The layup is not the same all over the blade span, resulting in the need to use partitions of the geometry to apply the correct material to each region. Because the blade is a shear web design, but is supposed to resemble the original blade with a box girder as closely as possible, some approximations were necessary in the spar cap and web area. Figure 3.6a shows the view from the root of the blade implemented in Abaqus. In comparison, the box girder structure of the original blade in reality is shown in Figure 3.6b, imported from a CAD model of the blade. On the outside of this structure are the two outer shells added in reality. In order to resemble the lay-up as closely as possible in the Abaqus model, the same layup regions are defined. The box girder has transitional areas between its spar cap regions and the shear webs. These are also defined in the Abaqus model, as can be seen in Figure 3.6a. The transitional lay-up from the box girder is applied in the regions between the shear webs and the spar cap and around the whole circumference until the z-position, where the shear webs start. The transitional layup is as shown in Figure 3.6b; in reality, however, it is also partly defined in the shear web region. As an approximation, this is not done in the Abaqus model. Instead, the shear webs are defined with the layup defined in the region marked in Figure 3.6b. The spar cap is applied with the same lay-up and width as in the in reality manufactured OLW934 blades. In addition to these lay-ups, the shell lay-up is added as the outer skin in all regions. Lastly, the root insert lay-up is included around the whole circumference at the root to result in a realistic root section, mass distribution, and center of gravity.

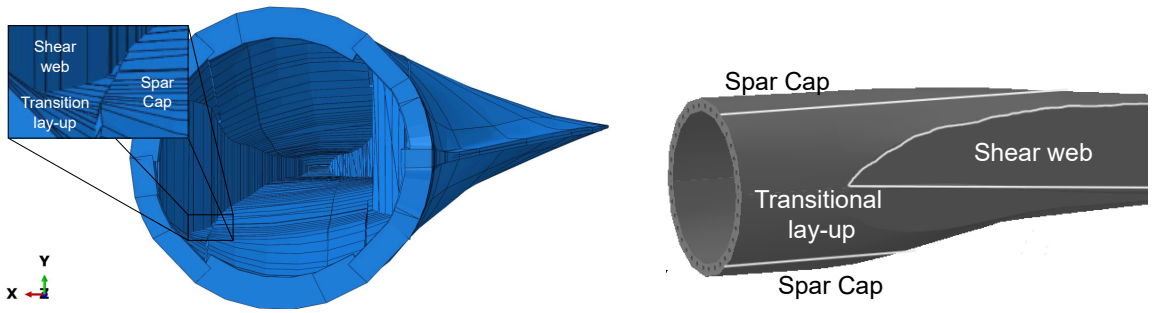

(a) Root thickness distribution.

(b) Box girder of original OLW934 blade [6].

Figure 3.6: Difference in modeling of the spar in the Abaqus model and the spar construction in reality.

The resulting thickness distribution in the rendered conventional shell model view can be seen in Figure 3.6a. The spar cap lay-ups are clearly visible, as their thickness is significantly higher than the adjacent transition lay-up thicknesses. The significant thickness variations could result in modeling artifacts in the stress and strain response

of the blade. These will have to be excluded from the analysis, as the tailoring on ply drops is smoother in reality.

Because some masses are not included in the layup model, containing only the above-mentioned materials, engineering constants are used to include these to match the mass and center of gravity with the original. They are added as nonstructural mass to the areas where they apply and consist of adhesive, gel coat, root nuts, and the tip break with its shaft. In Figure 3.7, the areas where the nonstructural mass was applied are shown. The gel coat is applied to the whole outer shell as it protects the outer layer of the blade from environmental factors. Figure 3.7a shows the application of the adhesive. As most of the adhesive is used to glue the box girder into the shells, it is distributed along the area where the box girder is in real life. The extra weight for the root nuts is applied in the root insert area, as can be seen in Figure 3.7b. And lastly, in Figure 3.7c, the application of the extra mass for the tip break system and its shaft is shown.

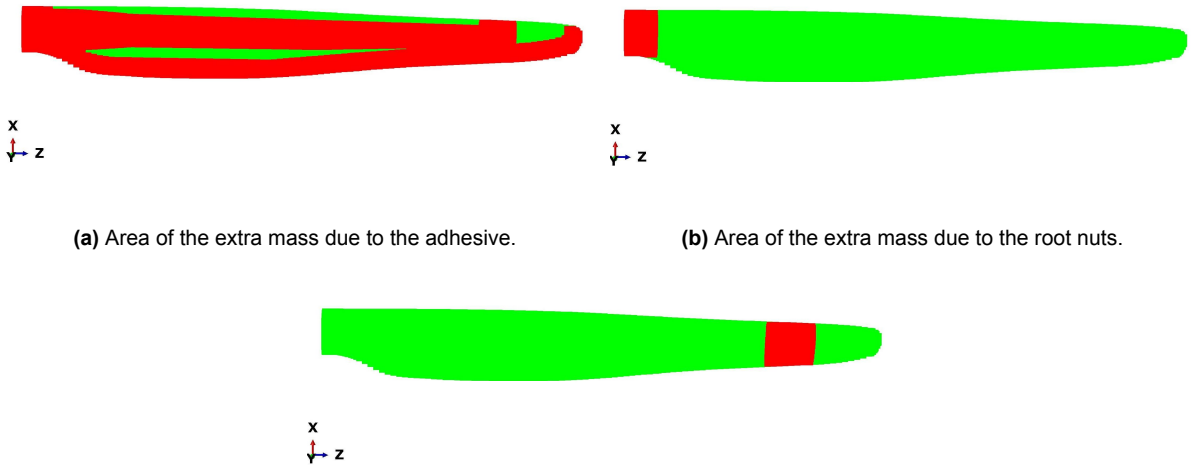

(a) Area of the extra mass due to the adhesive.

(b) Area of the extra mass due to the root nuts.

(c) Area of the extra mass due to the tip break.

Figure 3.7: Extra nonstructural masses implemented as Engineering features.

The tip break adds mass at the cut of the blade, as the bearing of the tip shaft is there. Its center of gravity is z=7.88 m in reality. Even though there is also some mass at the root and along the blade due to the shaft, the main mass is approximated to be in the area shown in Figure 3.7c. Using these extra masses is the mass with 321.42 kg of the simulated blade, only 1.85 % different from the median of the in-reality manufactured blades. The center of gravity of the simulated blade is at 3.18 m and thus 4.56 % different from the reality. The center of mass is, in reality, about 15 cm closer to the tip. The differences in mass and center of gravity are considered to be small enough to have negligible effects on the simulation results.

3.1.3. Meshing

The two parts, blade and tip, are meshed using S4R elements, which are linear 4-node elements, with reduced integration and hourglass control. As explained in subsection 2.2.4, these elements reduce the computational time due to their linear characteristic in comparison to quadratic elements. The reduced integration prevents shear locking from happening, and the hourglass control integrated in Abaqus CAE ensures physical solutions without hourglassing effects. A global mesh size of 0.02 m is used with additional refinements in areas where it is necessary due to small geometries. The global mesh size and element type are proven to be appropriate with a mesh convergence study of the redesigned blade in section 7.5. Because the outer airfoil shape stays exactly the same and only the internal structure is changed, that is considered to be sufficient. Additionally, it can be considered conservative as the deformation of the redesign is significantly higher, which would result in a slower convergence than in the originally modeled blade.

3.1.4. Constraints and Simulation setup

The last step in the setup of the Abaqus FEM-model is applying constraints and setting up the actual simulation parameters. As mentioned before, the tip is connected to the blade using a tie constraint. The blade root is completely fixed utilizing the full fixation of a reference point, which is coupled to the root with a kinematic coupling constraint.

In the following analysis, two FEM simulations are done, testing the eigen frequencies and a deflection analysis using loads calculated from HAWCStab2. Therefore, two models are prepared with different loads and simulation setups. The eigen frequency analysis does not require the application of loads, and the simulation is set up by adding a Frequency step to the simulation. In the second simulation, the load model, the loads are applied in five point forces along the blade span. At the correct z-position, a partition of the blade is made and a reference point (RP) is introduced, as can be seen in Figure 3.8. The loads are applied on the reference point, which is coupled to the outer surface of the blade with a distributed coupling constraint. This model is run by introducing a Static, General step. In order to check the blade for failure, the CFAILURE failure index variable is added to the field output, which includes the failure indices introduced in subsection 2.3.1 in the output.

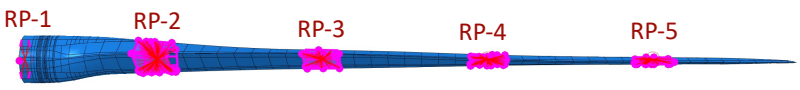

Figure 3.8: Coupling constraints at load input sections.

3.2. HAWCStab2 Setup

In order to know how the system behaves aeroelastically and to predict the design loads for the blade in the FEM-model, a HAWCStab2 model is implemented. In this report, only a steady state calculation using HAWCStab2 is done due to simulation time reduction, disregarding turbulent and steady time-series influences on the system. A factor of 2 is multiplied by the resulting steady-state loads to receive a reasonable

estimate of the ultimate loads on the blades, which is an engineering estimate from DTU in early design phases. This factor is to be verified later using Flex4 turbulent flow calculations. The HAWCStab2 inputs are generated using the Python module lacbox made at DTU. It enables loading and saving st.dat and ae.dat files, and the c2_def block in the main body definition in the *.htc* file. The inputs and simulation setup are described in this section.

3.2.1. Structural inputs turbine

HAWCStab2 requires structural inputs describing the turbine. These include information about the tower, the tower top, the hub, and the shaft, as well as their orientation and constraints towards each other. The structural inputs are described in a structural input file for each component and the definition of a main body in the *.htc* file, including the definition of the centerline of the body in the c2_def block. The structural input files for HAWC2 and HAWCStab2 include the parameters listed in Table 3.5, and the centerline definition in the *.htc* file requires the x, y, and z position of the centerline and the twist along the blade span.

Table 3.5: Parameters used in the HAWCStab2 structural input files.

HAWCStab2 structural input file parameters	
Curved length s	Area moment of inertia around x I_x
Distributed mass m	Area moment of inertia around y I_y
x distance from half-chord to mass center x_m	Torsional stiffness constant K
y distance from half-chord to mass center y_m	Shear factor k_x
Radius of Gyration r_{ix}	Shear factor k_y
Radius of Gyration r_{iy}	Cross sectional area A
x distance from half-chord to shear center x_s	Structural pitch η_z
y distance from half-chord to shear center y_s	x distance from half-chord to elastic center x_e
Modulus of elasticity E	y distance from half-chord to elastic center y_e
Shear modulus of elasticity G	—

These input data are found from the input data for a Flex 4 simulation conducted by NorZet. This simulation calculated the aeroelastic behaviour of a target turbine with the old 9.34 m blades. These turbines are intended to be equipped with the new 9.34 m blades, and the structural, aerodynamic, and operational data from the Flex4 model can be used in the setup of the HAWCStab2 model.

The structural input file for the tower *Tower_st.dat* is generated from the structural input in the Flex 4 model. Because the two aeroelastic solvers use different input parameters, the following calculations are necessary to get the required parameters

shown in Table 3.5.

$$I_x = \frac{EI_x}{E} \tag{3.5}$$

$$I_y = \frac{EI_y}{E} \tag{3.6}$$

$$K = \frac{\pi}{4}\left(R^4 - r^4\right) \tag{3.7}$$

$$A = \pi\left(R^2 - r^2\right) \tag{3.8}$$

$$ri_x = \frac{I_x}{A} \tag{3.9}$$

$$ri_y = \frac{I_y}{A} \tag{3.10}$$

Additionally, Young's modulus and shear modulus of steel $E = 210$ GPa and $G = 80.769$ GPa are used, and shear factors of $k_x = k_y = 0.5$ with small all thicknesses, as the tower has cylindrical cross sections [64][65]. The x and y distances of the mass, shear, and elastic center, as well as the structural pitch, are set to zero over the length of the tower because it is a symmetric hollow cylinder. Therefore, also the x- and y-position of the centerline of the tower, as well as the twist, are set to 0 in the main body definition in the *.htc* file. This concludes the setup of the tower.

The next main body to be defined is the tower top. In the *st.dat* file, the parameters in Table 3.5 are defined using the Flex 4 input data and the *Tower_st.dat* file. The parameters are the same as in the top cross-section of the tower. They are used in two sections at the bottom of the nacelle and at the hub height.

Because of the lack of data for the hub input, the *Hub_st.dat* of the DTU 12.6 m blade HAWC2 model, which uses the Vestas V27 turbine, is used [66]. The curved length is changed to the hub length of 0.56 m according to the current hub. The z-position in the centerline definition is adjusted accordingly. Because the mass and inertia of the hub are defined in the *.htc* file later, only stiffness values are used from the Vestas V27 hub. These are not expected to be significantly different from the hub of the NorZet rotor, making this assumption reasonable.

The same is done for the *Shaft_st.dat*. Here, the file from the 12.6 m model is used, as it serves as a sufficient assumption. Additionally, as an assumption, the generator and shaft inertia from the Vestas V27 turbine model are used [66]. Because a steady state analysis using HAWCStab2 is done, this inertia would not play a significant role in the outputs, making this assumption reasonable. The rotor center z-position was taken from the Flex 4 data. The z-position of the shaft is positive for this turbine because it is a downwind turbine, and the shaft coordinate system's z-position is defined with the wind direction. This defines the rotor to be behind the turbine. In the description of the main body in the *.htc* file, the hub mass and inertias are updated using the Flex 4 data, concluding the structural inputs of the turbine.

3.2.2. Structural inputs blades

The structural inputs of the new 9.34 m blades are generated using the previously generated Abaqus FEM-model. Every 0.2 m along the blade length, all elements in the cross-section are defined as a new set. In order to be able to get clear cross sections, partitions are used to have new starting elements at the same z-position. These cross sections are named and loaded into the BECAS preprocessor Python code shellexpander. The shellexpander generates input files for the cross-sectional FEM-analysis tool BECAS from the Abaqus input files. Additionally, to the Abaqus input file, a file defining the coordinate system for the cross sections is also made in order to set the reference point of the cross section to the half-chord point. The half-chord is the reference axis for HAWC2 and thus all structural parameters need to be calculated with respect to that. The shellexpander then generates a folder with the input files for BECAS for each cross section and a *shellexpander_sections.log* file to be used in the following BECAS calculation. Because shellexpander does not take the extra masses defined in subsection 3.1.2 into account, when transferring the cross-sectional data to BECAS an artificial layer is added on the outside of the blade shell with minimal stiffness and thickness, and high strength, which has a high density. The layer density and thickness are adjusted until the blade without the extra masses has a mass of 322.65 kg and a center of gravity of 3.2 m. The mass is thus only 0.38 % different from the mass obtained in the original FEM-model and the center of gravity has a percent difference of 0.63 %. The mass and center of gravity of the two models are thus similar enough, making their difference negligible.

In the next step, a BECAS script is made to import these and generate the *Blade_st.dat* file as an input for HAWCStab2. The BECAS script loads the input and loops through each cross-section name from the *shellexpander_sections.log* file. After building the correct arrays for BECAS, the cross-sectional stiffness and mass are calculated and used in the following to calculate the cross-sectional properties of the section. Figure 3.9 shows an exemplary cross-section of the blade at 3 m with its elastic, mass, and shear center calculated by BECAS.

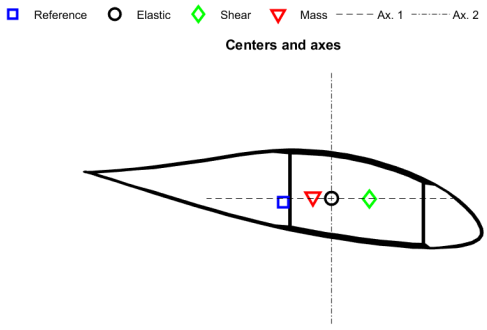

Figure 3.9: Cross sectional properties at $z = 3$ m computed by BECAS.

Using the BECAS_Becas2Hawc2 function, the parameters of the current cross section are then written to the *Blade_st.dat* file. The style of the *Blade_st.dat* file made

by BECAS differs from the inputs in Table 3.5. Here, the full stiffness matrix is used instead of defining the distances to the shear center, the elastic moduli E and G, the area moments of inertia, the torsional stiffness constant, and the shear factors. Additionally, the z-position of the cross sections along the blade is used instead of the curved length. This format is also a usable *Blade_st.dat* input file format for HAWC2 and HAWCStab2 and can be used in the following analysis.

The centerline of the blade for the c2_def block of the *.htc* file is defined using again the Abaqus FEM-model and the Flex input data. The twist is taken from the Flex input. It is defined at specific cross sections along the blade. For these cross sections, the x-, y-, and z-position of the centerline, which is defined as the half chord, is found from the FEM-model by measuring the half chord position at each section. The resulting centerline can be seen in Figure 3.10.

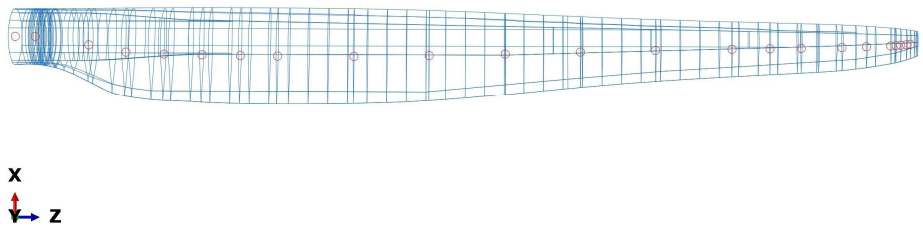

Figure 3.10: Centerline of the blade used in the c2_def block shown by the red circles.

3.2.3. Airfoil definition inputs

The aerodynamic input for HAWC2 and HAWCStab2 is defined in an ae.dat file, which contains the blade chord and relative thickness of the blade along its curved length, and a pc.dat file, which defines the different airfoils of the blade. The relative thickness of each airfoil is defined, and its properties include the distribution of the lift, drag, and moment coefficient along the angle of attack. HAWC2 interpolates the airfoils between the defined airfoils at specific relative thicknesses. These inputs are generated for the new model from the Flex 4 input data.

The ae.dat file is generated using lacbox to load and save the ae.dat file with the new data for curved length, chord, and relative thickness. Where the curved length is approximated to be the radius defined in the Flex 4 model. The chord of the last section at z=9.34 m is reduced to 0.1 m to resemble the real tip of the blade. The pc.dat file can be directly generated from the input without modifications.

3.2.4. Operational inputs and simulation setup

Also, an operational input is necessary for the HAWCStab2 to run successfully. The operation of the turbine is defined in an .opt file, containing the wind speeds of the

operational regime and the corresponding pitch and rotational speed. In this case, a fixed speed and pitch stall turbine is analysed, resulting in a constant pitch and rotational speed in the full wind regime in the .opt file. The pitch and rotational speed are set to be the same as in the Flex 4 model.

After defining all input files for the HAWCStab2 simulation, the *.htc* master file is set up next. The master file of the DTU 10 MW and the 12.6 m blade HAWC2 model are used as a base. The first part in the *.htc* files is the main body definitions described before. The next block contains the orientation of the bodies to each other. No tilt or yaw angles are introduced, but the free shaft rotational speed is updated in the relative definition of the tower top last and shaft 1 bodies. In the relative between the shaft last and the three hub 1 bodies, the coning angle of 13° is introduced. This concludes the changes in the orientation block. The next block is the constraint block. Instead of using bearing 1, defining free rotation, in this case, bearing 3 is used, which fixes the shaft rotation to a specific rotational speed. This measure disregards the influence of the generator control in this study. A more exact speed control should be investigated in the following research, but is rendered out of scope for this report. Because this turbine does not have a pitch control, the hubs and blades are also fixed to each other in the constraint block, and the pitch bearing2 definition is deleted.

The next block is the wind block, containing the tower_shadow_potential block. In these, the hub height and the radius of the tower at the bottom and top are defined. In the aero block, only the change of the input files and the number of aerosections is necessary. That is done, and next, the following DLL blocks are deleted, because no control is possible in the current model. Lastly, the hawcstab2 block is updated, which sets the commands for running HAWCStab2 in the terminal version called HAWC2S. After updating the path to the .opt file and output folder, the commands *compute_steady_states*, *save_power*, and *save_induction* are given, concluding the *.htc* master file.

To generate an *.htc* file to submit for simulation, the function *make_hawc2s* is used from the package myteampack from DTU. It deletes unnecessary information and generates a new HAWCStab2 *.htc* file based on the master *.htc* file. This file is submitted, resulting in a power *.pwr* file containing all steady-state operational data and induction files over the wind regime. The aeroelastic Campbell diagram and with that the eigen frequencies of the blade and the entire turbine are found by using the GUI interface HAWCStab2 to be able to identify the eigenmodes in the visualization.

3.3. Simplified Load estimation

The FEM-model gets loaded using the maximum blade root moments in the edgewise and flapwise direction found in the HAWCStab2 .pwr file. The bending moment over the blade span is found using the second-order polynomial approximation function Equation 3.11 to get the approximated moment distribution, which is used at DTU Wind to approximate a realistic moment distribution over the blade.

$$M(x) = M_0 \left(1 - 1.75 \cdot \frac{x}{L} + 0.75 \cdot \left(\frac{x}{L}\right)^2\right) \tag{3.11}$$

The value M_0 is, however, not directly the maximum value of the HAWCStab2 calculation along the wind speed regime. As in the HAWCStab2 simulation, only steady states were calculated; these values do not represent real-life load states. An engineering approximation of the characteristic load for the ultimate load case, DLC 1.3, in the early stages of a blade design is multiplying the steady state loads by a factor of 2. DLC 1.3, which includes extreme turbulence, is chosen as the design load case because it is usually the load case experiencing the highest ultimate loads. Next to this factor, partial safety factors are also necessary to load the blade with the correct design load. The blade is loaded using Equation 3.12 [53].

$$M_0 = M_{max,HAWCStab2} \cdot 2 \cdot \gamma_f \cdot \gamma_n \tag{3.12}$$

A load partial safety factor of $\gamma_f = 1.35$ is set in the standard IEC 61400-1 for load case DLC 1.3 [53]. The partial safety factor for the consequence of failure for a ”safe-life” structural component like the wind turbine blade is $\gamma_n = 1$ [53]. With that, the design load bending moment distribution resulting from HAWCStab2 is found. The edge and flap load is applied in both directions, in upwind and downwind, and towards the leading and trailing edge as a conservative estimate. These design load estimates are compared to Flex 4 time series ultimate loads computed by NorZet in the next step. On the FEM-model, only the HAWCStab2 load direction estimates that approximately agree with the time series result are used. For the other directions, the Flex4 result is used instead, as they are assumed to be more correct due to detailed time series simulations.

In order to apply the moment distribution on the FEM-model, forces in 5 different spots along the blade are used. The forces to result in the correct moment distribution are found by interpolating for the moment at each position and then using Equation 3.13 [58]:

$$\begin{pmatrix} F_1 \\ F_2 \\ F_3 \\ F_4 \end{pmatrix} = \begin{bmatrix} \frac{1}{z_1 - z_2} & 0 & 0 & 0 \\ \frac{z_3 - z_1}{(z_2 - z_3)(z_1 - z_2)} & \frac{1}{z_2 - z_3} & 0 & 0 \\ \frac{1}{z_2 - z_3} & \frac{z_4 - z_2}{(z_3 - z_4)(z_2 - z_3)} & \frac{1}{z_3 - z_4} & 0 \\ 0 & \frac{1}{z_3 - z_4} & \frac{-z_3}{(z_3 - z_4)z_4} & \frac{1}{z_4} \end{bmatrix} \cdot \begin{pmatrix} M_2 \\ M_3 \\ M_4 \\ M_5 \end{pmatrix} \tag{3.13}$$

The load at z=0 is $F_5 = 0$ N.

4

Results and Analysis

This chapter shows the results from the FEM and HAWCStab2 simulations. Additionally, an analysis is done on how big the improvement potential of the original OLW934 blade is and which areas of the blade are loaded the most.

4.1. Eigenvalue analysis

In this section, the eigenvalue results for the blade and the entire turbine are evaluated. The blade is analyzed structurally using the FEM-model and the HAWCStab2 model to check how accurately the blade model in the HAWCStab2 represents the values from the detailed FEM-analysis. For the turbine, a full aeroelastic analysis is shown using HAWCStab2.

4.1.1. Structural blade only eigenvalue analysis

The results of the structural analysis of the eigenvalues in the FEM-model and the HAWCStab2 model, as well as their percent difference, can be seen in Table 4.1.

Table 4.1: Blade only eigenfrequencies.

Mode	Mode name	FEM-model [Hz]	HAWCStab2 [Hz]	Percent difference [%]
1	1st flap	3.11	3.30	5.92
2	1st edge	5.89	6.42	8.61
3	2nd flap	10.38	9.91	4.63
4	3rd flap	20.54	20.73	0.92
5	Combination flap and edge	25.66	26.75	4.16
6	1st torsion	27.83	33.41	18.22

The frequencies of the first six modes in the FEM-model and the HAWCStab2 model are shown, including the first, second, and third flap modes, the first edge, the first torsion mode, and a combined flap and edge mode. It can be seen that the third flap mode is at a lower frequency than the second edge-including mode, indicating that the blade is significantly stiffer in the edgewise direction.

When comparing the FEM-model and HAWCStab2 model frequency results, it is apparent that the values match approximately but not exactly. While the highest percent difference with 18.22% can be observed in the 1st torsion mode, the frequency results are almost identical at the 3rd flap mode with a percent difference of only 0.92%.

There is no real pattern in the differences obtainable. Sometimes the HAWCStab2 model predicts higher frequencies, as in modes 1, 2, 5, and 6, and sometimes the FEM-model predicts higher values, as can be seen in modes 3 and 4. Also, the frequency difference does not seem to get higher or lower with increasing mode number. This suggests that the difference is a result of the simplifications made to get the HAWCStab2 model and not a miscalculation.

While the FEM-model is a detailed, high-resolution shell model, the HAWCStab2 model runs a simplified version of the blade as a beam model. Additionally, the difference in the method to add the extra masses in the two models described in subsection 3.1.2 and subsection 3.2.2, and other simplifications in the ShellExpander and simplifications in the stiffness calculation in BECAS can result in the observed behaviour.

In literature, a similar behaviour can be observed. In ”Static response of wind turbine blades: Comparison of low- and high-fidelity numerical models”, A M Antunes et al. found that the beam-based models result in different frequencies than the shell element-based models, especially for torsion modes and higher eigen mode numbers [67]. The first torsion mode was found to be the first, where the models differ significantly [67]. Thus, for the purpose of this report, the eigenvalue results of the HAWCStab2 model are considered to be close enough to render the blade input data as realistic enough for the load estimation of the blade and the following optimisation.

4.1.2. Aeroelastic eigenvalue analysis turbine

The aeroelastic behaviour of the entire turbine can be evaluated using the aeroelastic Campbell diagram shown in Figure 4.1. It can be seen that its general behaviour differs quite significantly from the example in chapter 2. This is again a result of the fixed rotor speed characteristic. Because the rotor speed does not change with the wind speed, the natural frequencies as well as the excitation frequencies 1P, 3P, 6P, and 9P do not change. Only the first flapwise eigen frequencies show a slight reduction in frequency due to the reduction in damping on the right side of Figure 4.1.

In the case of a stall-regulated turbine with a fixed rotor speed, the frequency placement is straightforward. The natural frequencies are simply not allowed to coincide with one of their excitation frequencies. As explained in chapter 2, these are for the tower modes, the frequencies 3P, 6P, and 9P, and for the blades, 1P and 3P. In Figure 4.1, it can be seen that the only dangerous eigen frequency is the first backwards whirling flap, which is with a minimum value 2.44 Hz after rated wind speed close to the excitation frequency 3P of 2.175 Hz.

When looking at the damping plot, it can, however, be seen that this frequency is the one that is damped the most. In general, in the damping plot, the typical behaviour

that the flapwise modes have higher damping than the edgewise modes due to aerodynamic damping can be seen. Also, it is apparent that the aerodynamic damping reduces with increasing wind speed, which can be explained by the stall behaviour of the turbine. The damping is the lowest at a wind speed of 21 m/s. At this wind speed, the first backwards whirling flapwise mode should therefore be monitored to ensure safe operation. In the redesign of the blade, this eigen frequency should not fall closer to the excitation frequency 1P than the original blade's value of 2.44 Hz.

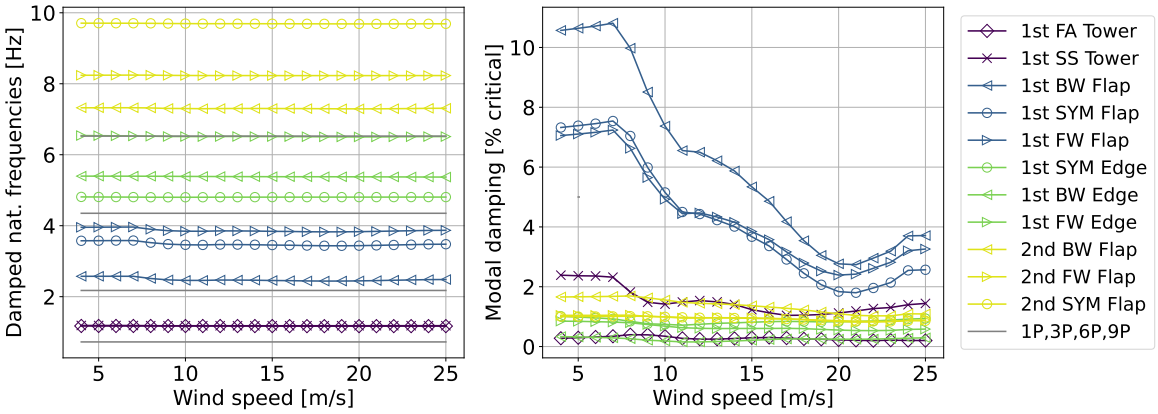

Figure 4.1: Aeroelastic Campbell diagram of the NorZet Turbine with the OLW934 blade.

4.2. HAWCStab2 analysis

The operational data results of the HAWCStab2 simulation are discussed in this section, followed by a deflection analysis and the resulting steady-state loads. These are additionally compared to a turbulent Flex 4 simulation conducted by NorZet, including 676 load cases, to result in the correct loads to apply on the structural FEM-model.

4.2.1. Operational data results

In Figure 4.2, the induction behaviour of the rotor can be seen for the different wind speeds over the blade span. Because the turbine is stall-regulated and does not have a pitch bearing increases the angle of attack with increasing wind speed, eventually resulting in stall at rated wind speed. The angle of attack gets higher with higher tip speed ratios $\lambda = \frac{\omega R}{V}$. Because the rotational speed of the turbine relative to the wind speed is higher at low wind speeds and with the s position along the blade, here lower angles of attack are found. The stall characteristic of the turbine can be seen in the lift coefficient behaviour. The C_l increases with the angle of attack until reaching the rated wind speed, where the turbine goes into stall and the flow separates. This results in decreasing lift coefficients after V_{rated}.

The induction plot shows that the induction is the highest at low wind speeds and decreases thereafter. This is a result of the fixed rotor speed. In the low wind speed regime, the turbine is spinning faster than necessary, resulting in low angles of attack. Even though not much energy is extracted, due to the relatively tangential flow at the blade, the wind speed is reduced immensely before and after the turbine. Therefore,

the axial induction is high even though not a lot of power is extracted from the wind. With increasing wind speeds, the aerodynamic state at the blade becomes more and more profitable, resulting in higher power, even though the induction reduces. Even though the thrust force increases with higher wind speeds, the thrust coefficient and axial induction factor decrease because the constant rotor speed allows the wind to pass more easily through the turbine as wind speed rises. This is also the reason why there are higher induction values at the tip of the blade as the local rotational speed increases along the blade span.

Lastly, the lift-to-drag ratio plot shows first an increase until 7 m/s and then a decrease. This is the case because the airfoil gets aerodynamically better with increasing wind speeds, as explained before, but at some point, the rotational speed is not high enough, inducing more drag in comparison to the lift. After V_{rated}, the lift-to-drag ratio reduces significantly, as then the stall conditions induce high drag values. Also, C_l/C_D is higher at the tip because the airfoil shape gets thinner with the length of the blade, resulting in a better aerodynamic airfoil.

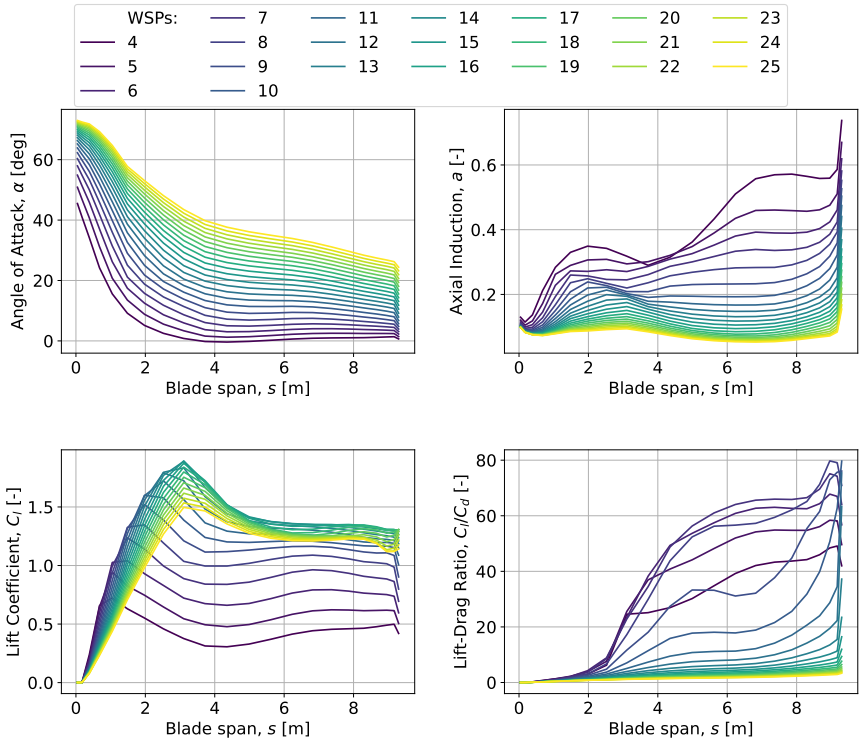

Figure 4.2: Induction properties of the Norwin Energy turbine using the OLW934 blade.

The operational data results from the HAWCStab2 calculation for the OLW934 blade and from a previous calculation of the OLW965 can be seen in Figure 4.3. The HAWCStab2 power curves show a typical behaviour of a stall-regulated downwind turbine with a coning angle and constant rotational speed. The power increases with increasing wind speeds until the turbine reaches the rated wind speed at around 11 m/s. The turbine goes into stall, and the curve gets limited to the turbine's rated power of 80 kW.

Above rated, it can be seen that the curves still keep increasing slightly. This does not follow the regular convergence behaviour above rated of upwind stall turbines. It can be explained by the fact that the downwind coning angle changes the effective angle of attack on the blade. At higher wind speeds, the increasing effective coning angle due to its deformation reduces the angle of attack, increasing the aerodynamic torque limit and thus the power output.

When comparing the two different designs, it can be seen that in the region below the rated wind speed, the two curves are almost identical. Above V_{rated}, however, the OLW965 curve stays slightly below the OLW934 curve. And the slope of the increase above V_{rated} is higher for the OLW934 case. The reason could be that increasing wind speeds result in a higher decrease in rotor area for bigger than for smaller blades, because higher deformations are induced. Thus, a higher reduction in rotor area results with $P = \frac{1}{2}\rho A V^3 C_P$ in lower power output. Additionally, some simulation setup differences could have an impact, like the use of different generator and stall models. Both simulations show, however, approximately the same behaviour, and the resulting power at the end of the operational range is the expected rated power of 80 kW of the turbine. This validates the conducted HAWCStab2 simulation for the OLW934 blade.

In the OLW934 thrust plot, it can be seen that the thrust plot increases constantly over the wind regime. This behaviour is typical for a stall-regulated turbine and differs greatly from a pitch-regulated turbine, where the thrust would decrease again after reaching the rated wind speed. A stall-regulated turbine, however, does not pitch its blades, resulting in a steadily increasing angle of attack and higher thrust loads. Above the rated wind speed, the turbine experiences stall, resulting in high thrust loads. Because this analysis is done for steady states, the thrust loads are not exact and should be checked in later research, including the dynamic stall behaviour, typical for stall-regulated turbines. Therefore, only the general trend of increasing thrust with wind speeds can be taken from this analysis.

In the plots for the power and thrust coefficients C_P and C_T, corresponding behaviours can be seen. Because the simulated turbine is also a constant speed turbine, there is no control of the C_P in the below-rated region. The power coefficient of the HAWCStab2 simulations increases first until approximately 0.4 and then starts to decrease, as its curve is the derivative of the power curve. The maximum C_P is therefore only reached at one specific wind speed of 7 m/s, resulting in a less efficient turbine than for torque-controlled turbines in the below-rated region where $C_{P,max}$ is used. Again, here is the general trend of the curves of the two simulations, very similar; it can, however, be seen that the highest C_P value of the OLW934 simulation is slightly lower than for the OLW965 simulation. Additionally, the starting C_P value at 3 m/s is already 0.05 higher than for OLW934. This result can be explained by the decreased blade length. With less blade length, the power in the below-rated region is less, and thus also the power coefficient.

Generally, the C_T plots show that the thrust coefficient reduces with increasing wind

speeds. This is also a result of the fixed rotor speed. C_T increases with the tip speed ratio λ, which is $\lambda = \frac{\omega R}{V}$. With increasing wind speed and constant rotational speed, λ and C_T are reduced. The OLW934 thrust coefficient is slightly higher in the below-rated region than the one from the OLW956 calculation. The difference is, however, minimal. These two plots, therefore, increase the validity of the new HAWCStab2 OLW934 simulation. Lastly, the plot of the torque shows a similar shape to the power curve. This can be explained by the equation for power $P = \omega Q$ with a constant rotational speed.

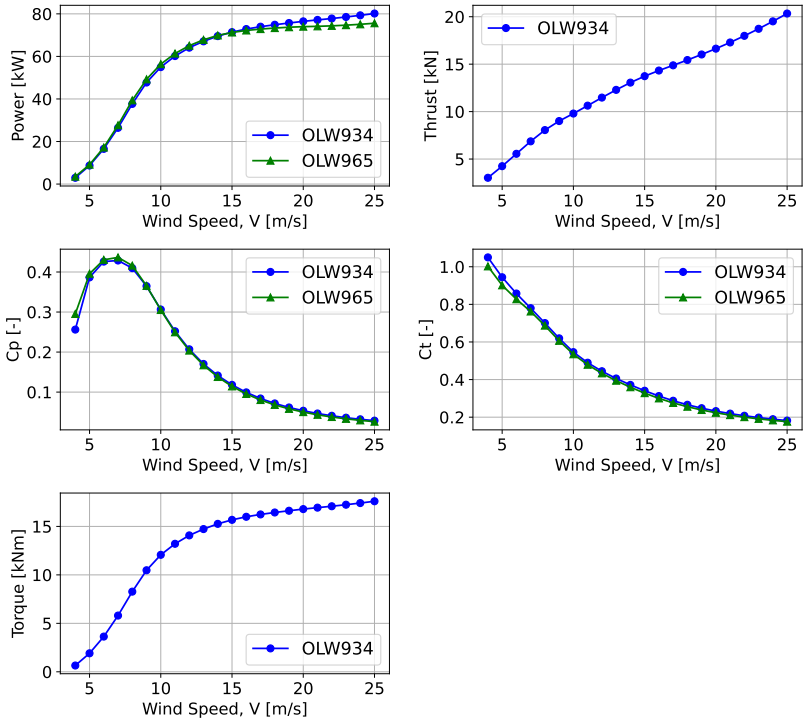

Figure 4.3: Operational behaviour of the NorZet turbine with the OLW934 blade from HAWCStab2 and Flex4 when available.

4.2.2. Resulting loads

Figure 4.4 shows the normalized flapwise and edgewise bending moments at the root of the blade over the wind speeds. It can be seen that the flapwise bending moment follows the behaviour of the thrust curve, and the edgewise bending moment follows the behaviour of the torque. This correlation can be explained by the working directions of the forces and the moments, as the flapwise bending moment at small pitch values mainly gets induced by the thrust force orthogonal to the rotor plane. The edgewise moment, however, is mainly a result of the torque in the rotor plane. It can be seen that the induced flapwise moment is significantly greater than the edgewise moment.

When comparing the simulation results of the two HAWCStab2 simulations, it can be seen that for both bending moments, the moment values of the OLW934 simulation exceed those of OLW956 in the above-rated region. Below rated the curves are

almost identical. This characteristic follows the behaviour difference in the power plot in Figure 4.3. It is reasonable to have higher bending moments when the power values are also higher, as more energy is extracted from the wind.

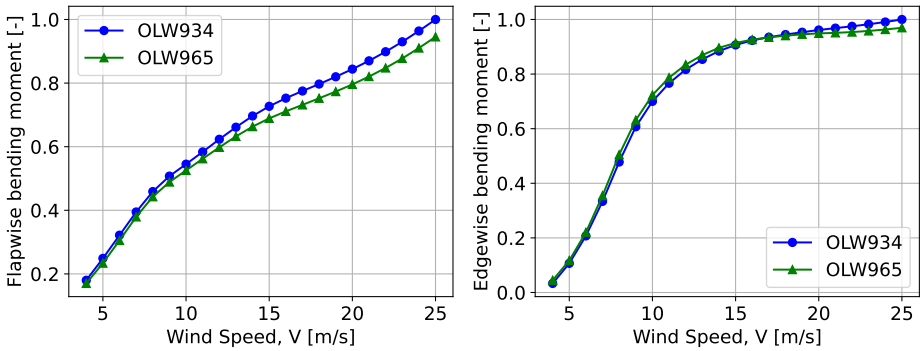

Figure 4.4: Normalized flapwise and edgewise bending moments for the NorZet E-3120 turbine with the blades OLW965 and OLW934.

In order to get the bending moments to be applied on the FEM-model, the maximum value of the steady loads needs to be multiplied by 2 and $\gamma_f = 1.35$, as explained in section 3.3. The resulting design loads from the HAWCStab2 simulation, as well as from time series results from a Flex 4 calculation conducted by NorZet for 676 load cases, are shown in Table 4.2. The design load for the Flex4 calculation was found by finding the highest loaded load case. It is as predicted in section 3.3, the DLC 1.3. extreme turbulence load case. The characteristic load is found by averaging the maxima of all time series. This one is then multiplied by the same load safety factor of $\gamma_f = 1.35$.

Table 4.2: Percent difference of design loads approximated from HAWCStab2 steady states from calculated loads using time series for 676 load cases in Flex4 by NorZet, calculated using absolute values.

Simulation	M_flap downwind [%]	M_flap upwind [%]	M_edge leading [%]	M_edge trailing [%]
Percent difference	5.57	48.01	-60.57	-31.29

It can be seen that the assumption of multiplying a factor of 2 to the steady state values results in very good agreement with the time series result for the flapwise downwind bending moment. For the other load directions, they, however, differ quite significantly. Because the Flex 4 calculation is expected to resemble reality better, in these load directions, the ultimate loading from the Flex 4 calculation is used to test the FEM-model. Figure 4.5 shows the bending moment distributions applied on the Abaqus FEM-model by loading five cross sections with the forces shown as the black dots in Figure 4.5. The moment distribution is multiplied by the root bending moment value in the specific direction to be analysed. The values of the forces applied at the black dots to result in the shown bending moment are calculated using Equation 3.13.

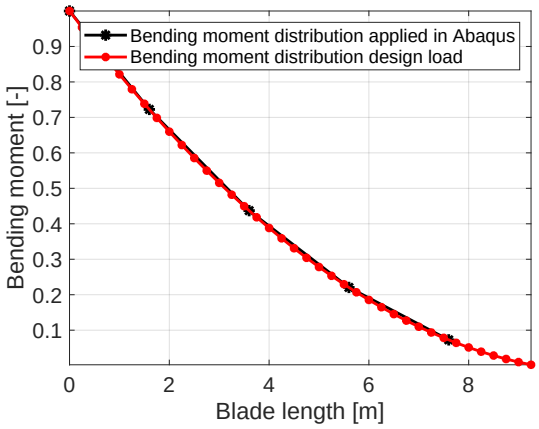

Figure 4.5: Normalized load distributions applied on the FEM-model in comparison to the load distribution of the design load.

The structural regions that are most vulnerable to fatigue are typically the adhesive joint interfaces and local areas with abrupt laminate thickness transitions [68][69]. These locations are prone to stress concentrations and, therefore, require dedicated fatigue analysis. However, neither of these regions is within the scope of the present study. While the adhesive regions are not modeled entirely, the stress concentrations at the thickness drops are also disregarded, as they are smoothened out in reality in comparison to the model. In this report, it is thus sufficient to base the design process solely on the ultimate loads. In a later iteration, should the fatigue analysis be included, however, either using a more exact model or component testing.

4.3. FEM analysis

In this section, the results of the FEM simulation are analyzed in order to find the Tsai-Wu failure index and deflections under the approximated ultimate load state DLC 1.3. The highest loaded areas are found as well, resulting in an evaluation of the improvement potential of the current blade OLW934.

The original blades' improvement potential can be evaluated using an analysis of the Tsai-Wu failure index and a deflection analysis. The failure criteria of Tsai-Wu is used to assess failure during this report, because it reflects the interaction between different stress components, and additionally can be used for many different loading scenarios, as explained in subsection 2.3.1. When considering the failure mechanisms available in Abaqus CAE, it is the most realistic one and is thus used in this report.

The Tsai-Wu failure criterion and deflection are evaluated for upwind and downwind flapwise loading and edgewise loading towards the trailing and leading edge.

4.3.1. Failure analysis

When evaluating the Tsai-Wu failure index, the validity of the result has to be checked, as it is very prone to local artificial stress concentrations, which give out non-sensical results. The original failure index values for all directions can be seen in Table 4.3.

Table 4.3: Tsai-Wu failure index and maximal deflection analysis under prescribed loading.

Tsai-Wu index [-]	Complete model	Without artifacts and Unifillo ply	Highest loaded ply	Direction
Flapwise downwind	1.53	0.87	UD1200	compression transverse
Flapwise upwind	1.22	0.71	UD600	compression transverse
Edgewise trailing	0.56	0.40	UD1200	compression transverse
Edgewise leading	1.10	0.65	UD1200	tensile transverse

It can be seen that when only looking at these values, the blade, according to the Tsai-Wu failure index, would fail in both flapwise directions and the edgewise direction, with bending towards the leading edge. To result in reasonable numbers, the model is checked for unrealistic artifacts, and these regions are neglected from the analysis. These artifacts include force load introduction areas, unsmoothed layup transitions, and areas with material definition assumptions, like the tip and the trailing edge flange. Additionally, the ply Unifillo, which is added in the spar cap design to distribute the resin flow better, was removed from the analysis. Because it was never expected to contribute to the strength of the blade, it is thus due to its low strength failing under the prescribed loading in the two flapwise directions. This failure is, however, not considered critical, and in the redesigned blade, this ply will be left out. The resulting failure index values without unrealistic artifacts and the Unifillo ply can be seen in Table 4.3. The field outputs for the different loading directions are discussed in the following.

The first and most critical direction to be analysed is the flapwise downwind direction. Figure 4.6 shows the original Tsai-Wu field output of the blade under flapwise downwind loading in three different views, as well as the loading on the blade. The loading is as explained before, the result of Equation 3.11 using the flapwise root bending moment calculated. The non-intuitive application of the third load with a direction upwind is a result of Equation 3.13. To resemble the correct bending moment distribution in Figure 4.5, it is necessary to reduce the moment induced from the outermost load at this blade position. This loading is thus applied, and the Tsai-Wu failure index output is analyzed.

It can be seen that there are multiple regions that are heavily loaded, and that failure occurs as the Tsai-Wu failure criterion is above 1. As explained before, the Unifillo ply results will be ignored in this analysis, and modelling artifacts are altering the result. These, thus, also need to be identified and neglected. This can be done when analyzing the zoomed-in pictures of the regions A through E in Figure 4.7, which show the highly loaded area field output results without the Unifillo ply.

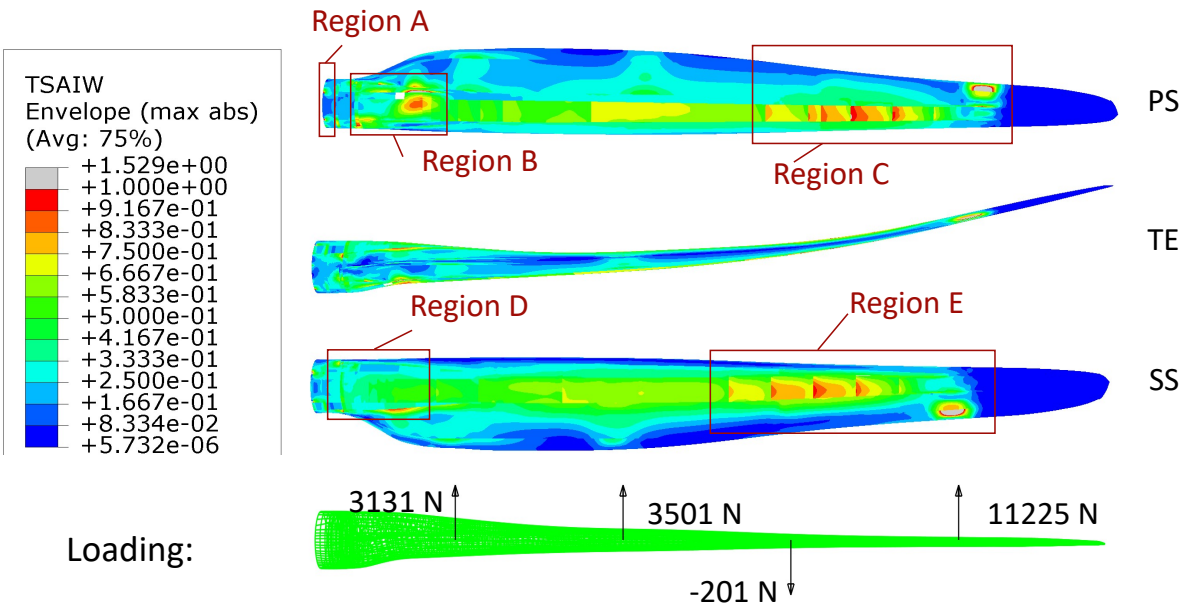

Figure 4.6: Tsai-Wu failure index for downwind loading of complete layup.

Figure 4.7b shows the root region. It can be seen that there are multiple elements that fail under the prescribed loading. These are situated at the edges between the spar cap layup and the transitional layup defined in Figure 3.6b. Thus, the stress concentration in these elements is induced by the big difference in layup thickness in the two regions. In reality, these transitions are done more smoothly. These failed elements are thus modelling artifacts, which can be neglected in the analysis. Also in Figure 4.7b, multiple regions can be seen that are highly loaded. Except for the stress region on the pressure spar cap, the other loaded regions are also neglected, as they result from sudden layup changes. The highly loaded region in the pressure spar cap region can, however, not be neglected. In this region, the innermost UD ply of the spar cap region has the highest failure index in the transverse direction. It is highly loaded in compression with a failure index of 0.8725. This is reported in Table 4.3 as the highest failure index in the downwind loading direction without considering the Unifillo ply and unrealistic artifacts. The failure occurs on the pressure side of the blade, which is loaded in tension. On the inside, however, high compressive loads in the transverse direction are applied to the laminate. As the UD-material has a low transverse compressive strength, as can be seen in Table 3.1, it shows a high failure index value. In the redesign, Biax or Triax plies should be used as the inner ply instead to provide transverse strength.

Figure 4.7d shows a part of the blade, from the half-blade length to the tip of the blade. The spar cap region is with a failure index of around 0.5, modestly loaded in tension. It can thus be seen that less material would be sufficient, and improvement potential is apparent. Additionally, on the right side of the blade snippet, failure can be observed. When comparing where this region is on the whole blade in Figure 4.6 it can be observed that this is the region where the highest point force is applied on the blade. Thus, this local failure is a direct result of that and can be neglected as

a modelling artifact. The same can be seen in Figure 4.7f, which shows the suction side tip region of the blade. Additionally, it can be seen that the spar cap region is slightly more loaded than the pressure side. This is due to the higher tensile strength than the compressive strength of the UD1200 material in the spar cap. Regardless, there is still significant improvement potential, as the maximum failure index value in this area is significantly below 1. The same can be seen in Figure 4.7e, which shows the suction side blade root region, which is only mildly loaded. The red region that can be observed in Figure 4.7e can also be neglected as an artifact of high thickness differences between adjacent layups.

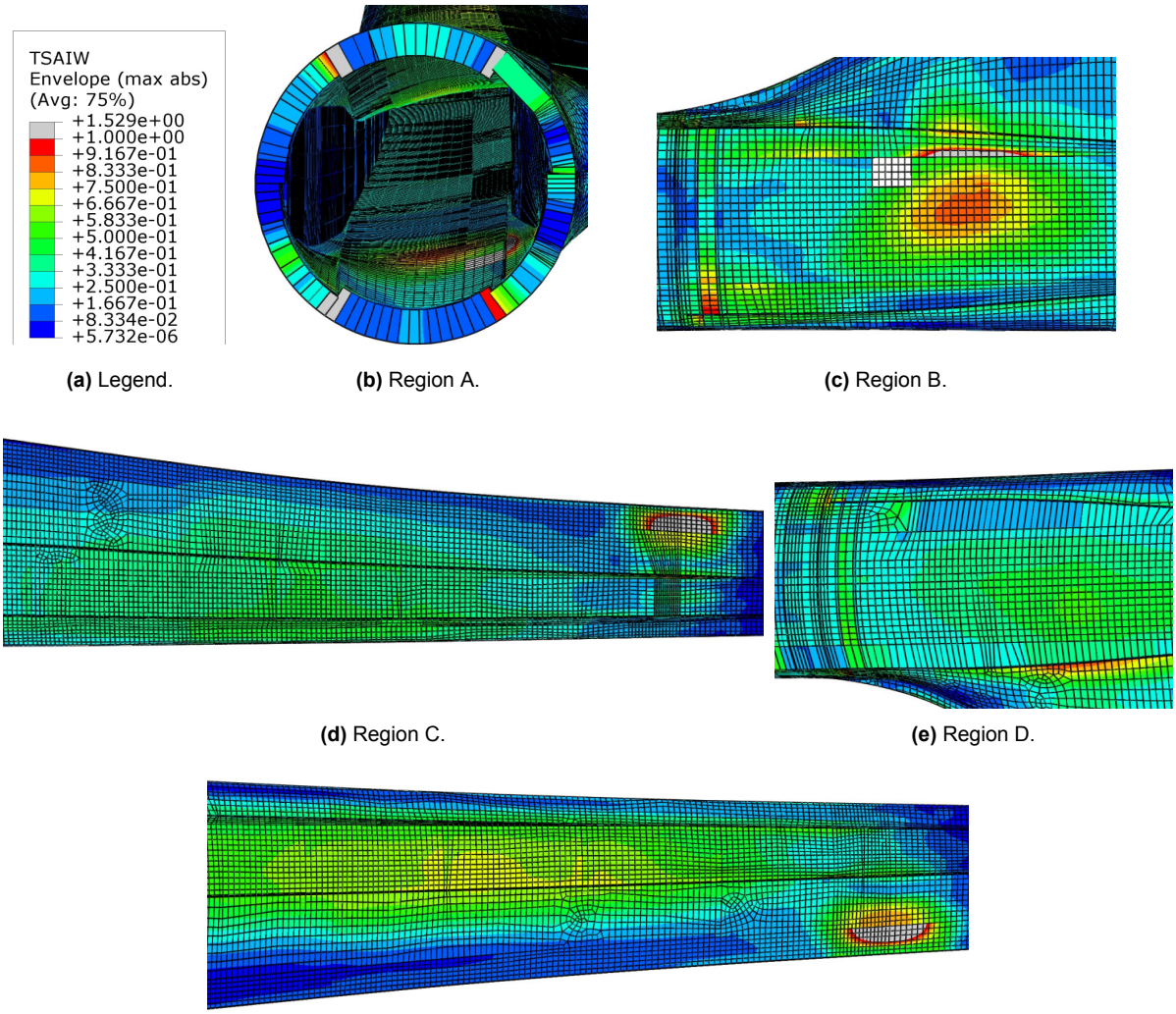

(a) Legend. **(b)** Region A. **(c)** Region B.

(d) Region C. **(e)** Region D.

(f) Region E.

Figure 4.7: Region areas defined in Figure 4.6 under downwind loading without Unifillo ply.

The next loading direction to be analyzed is the flapwise upwind loading. In Figure 4.8, the Tsai-Wu failure index of the blade can be seen in three views, including the Unifillo ply and modelling artifacts. It can be seen that in both Figure 4.6 and Figure 4.8, the regions where the loads are applied show higher stresses. The resulting stresses in the loaded regions can also, in this loading direction, be neglected as they are artifacts of the model.

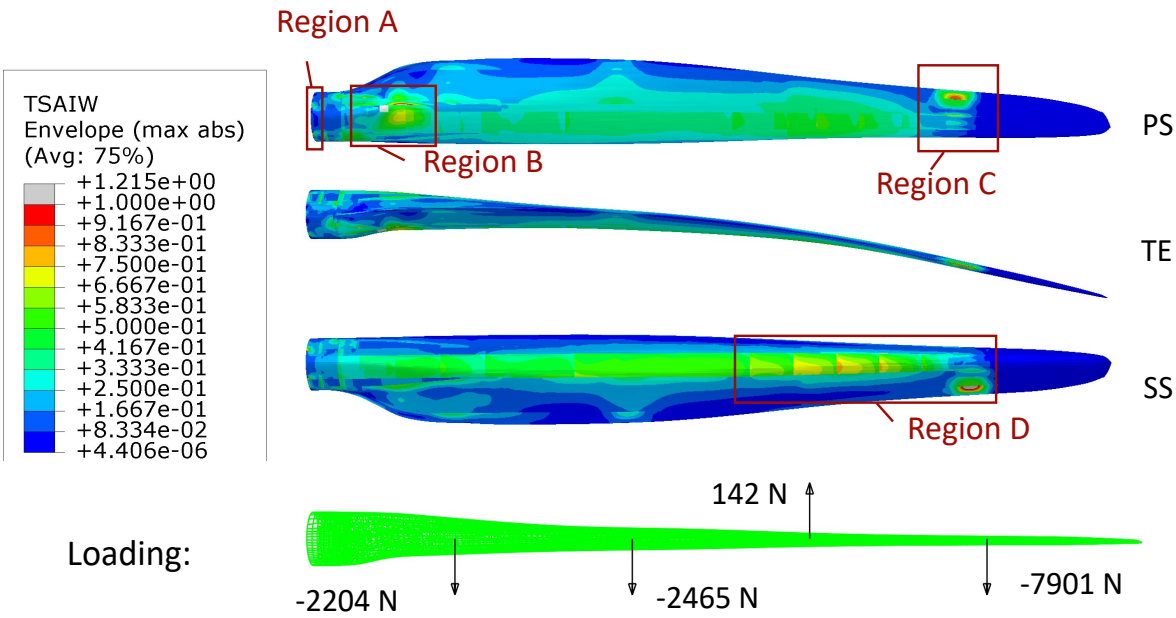

Figure 4.8: Tsai-Wu failure index for upwind loading of complete layup.

Figure 4.9 shows the regions A through D highlighted in Figure 4.8, excluding the Unifillo ply. In Figure 4.9b, the same artifacts can be seen as in the downwind loading scenario in Figure 4.7b. The elements adjacent to high thickness differences experience unrealistic stresses. The same can be seen in Figure 4.9c with a highly loaded area between the transitional and the spar cap layup. In Figure 4.9c, the highest Tsai-Wu failure index of this loading direction can also be found in the same region as in the downwind case. The blade is now, however, having the highest index in transverse compression in the UD600 ply used in the skin layup with 0.71, as can be seen in Table 4.3. This ply will be considered to be removed in the redesign, because the skin has high demands for transverse strength, which can better be provided by Biax material. It will thus be used as a design variable as well as the Biax skin thickness. In regions where it is not necessary, the UD-ply will be removed. In Figure 4.9d and Figure 4.9e, high stresses can be observed, similar to the downwind direction, where the outermost force load is applied. These can, as explained before, thus be neglected. The second highest loaded region can also be seen in Figure 4.9e, where the compression forces near the tip induce a failure index of about 0.35 in fiber direction. There is thus even higher improvement potential on the blade in the upwind loading case, and the downwind loading case is identified to be more significant for the design.

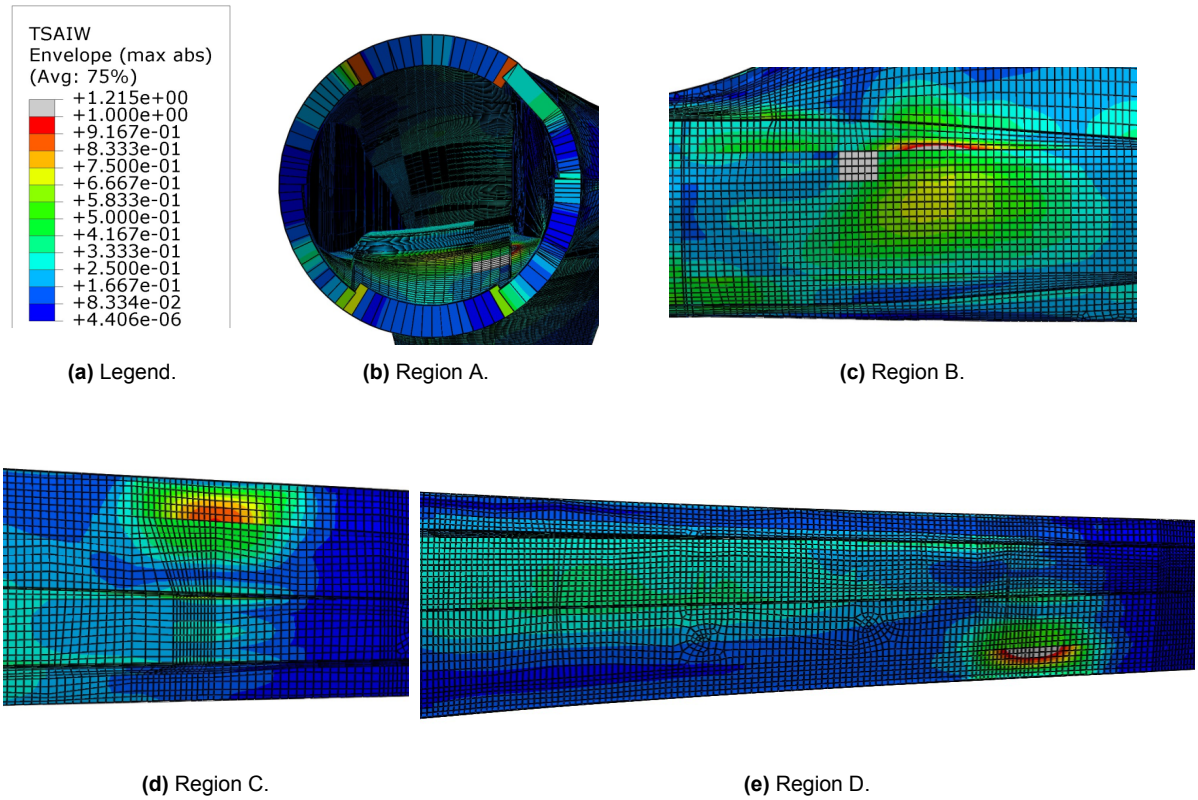

(a) Legend. **(b)** Region A. **(c)** Region B.

(d) Region C. **(e)** Region D.

Figure 4.9: Region areas defined in Figure 4.8 under upwind loading without Unifillo ply.

In Figure 4.10, the Tsai-Wu display output of the edgewise loading towards the trailing edge can be seen. In the three views, it can be observed that almost all over the blade, the stresses due to this loading direction are minimal.

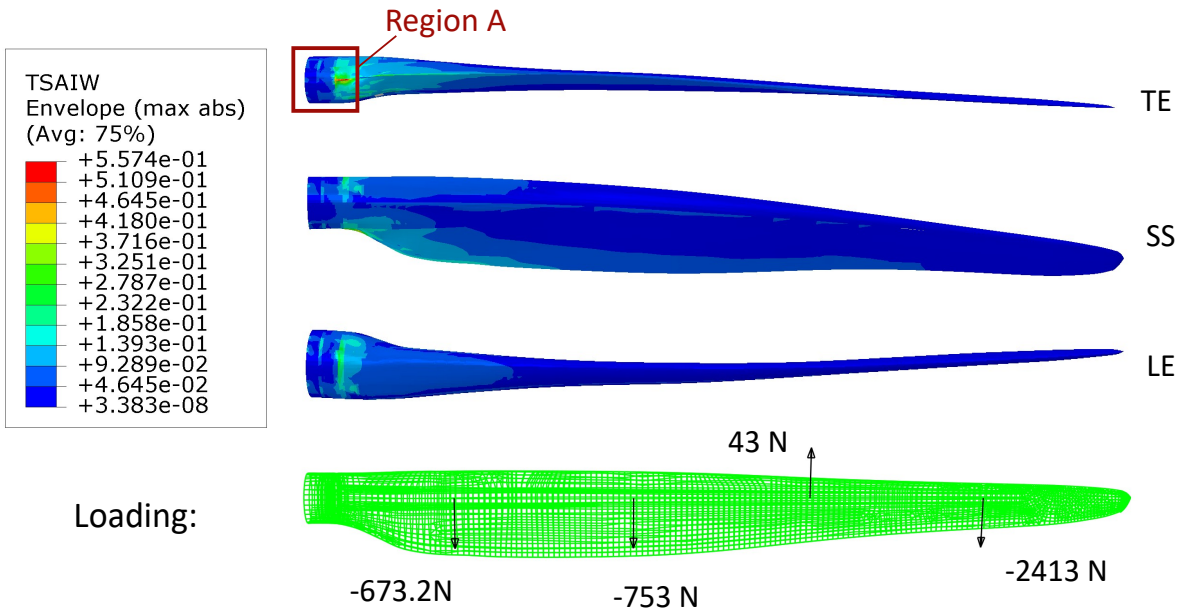

Figure 4.10: Tsai-Wu failure index for edgewise loading towards the trailing edge of complete layup.

The region with the highest failure index is the region where the geometry of the trailing edge starts building after the circular root section, shown in Region A in Figure 4.11. It can be seen that the highest stresses are apparent on the vertical surface of the trailing edge. Due to simplifications, the material in these regions is the same as the layup around. This is not true in reality, as in reality this surface is simply the end of the ply layups and adhesive in between. Thus, this area is not modelled realistically and is not considered in the analysis. In reality, the trailing edge joint can, however, experience failure, especially under fatigue loading. This area should thus be checked in a subsequent analysis to verify safe optimization. This is, however, outside of the scope of this report.

Around the flange surface, the highest stress in this loading direction is observed, 0.40. The highest loaded region is where the circular cross-section starts to transform into a trailing-edge shape. Thus, the big change in geometry induces stresses that result in a failure index of 0.40 in the trailing edge reinforcement layer UD1200, which has the highest index in transverse compression. This index is, however, comparatively to the other loading directions, the smallest, and high improvement potential is apparent.

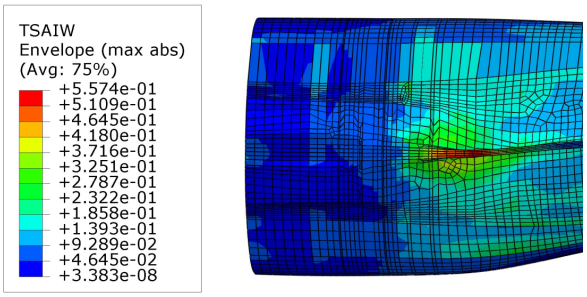

Figure 4.11: Region A defined in Figure 4.10 under edgewise loading towards the trailing edge without Unifillo ply.

The full blade output response in the edgewise loading towards the leading edge is shown in Figure 4.12. A similar stress state can be observed as in the loading towards the trailing edge. The index values are, however, higher. In the output, the Unifillo ply and artifacts are included. The Tsai-Wu failure index rises over the amount of 1 in the trailing edge region near the root, shown in Figure 4.12 as Region A.

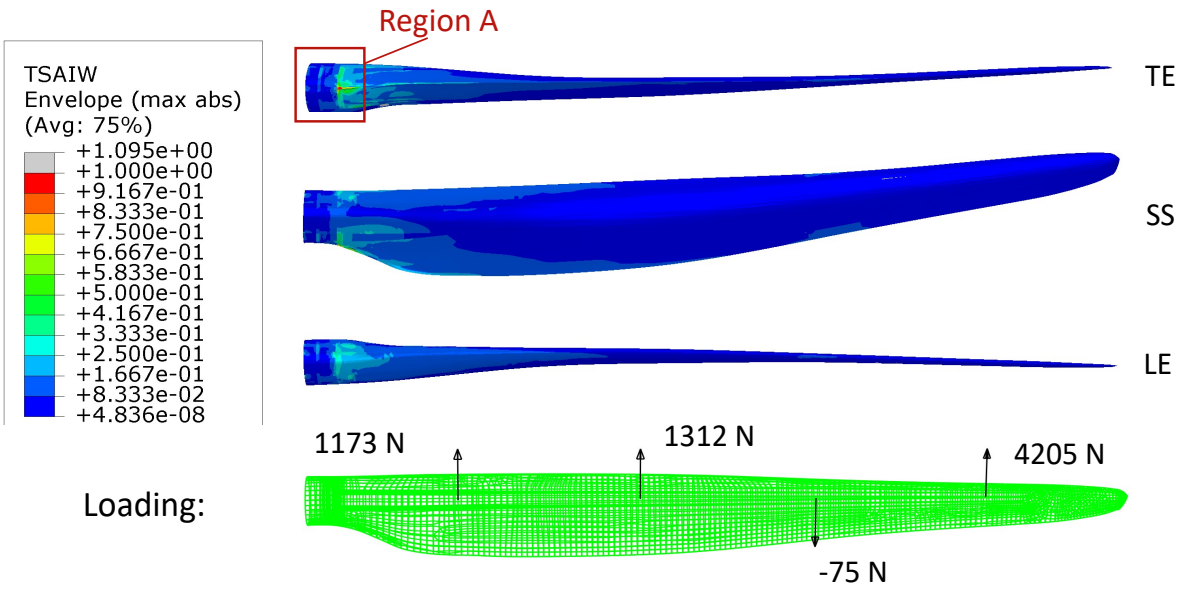

Figure 4.12: Tsai-Wu failure index for edgewise loading towards the leading edge of complete layup.

In Figure 4.13, the critical area can be seen, excluding the Unifillo ply. When also disregarding the flange area as explained in the loading towards the trailing edge, a maximum failure index of 0.65 is found in the trailing edge layup, where the geometry starts to significantly change from the root part to the blade airfoil. This is reported in Table 4.3 as well as that the same ply as in the loading towards the trailing edge has the highest index. In the same region, the highest failure index is obtained in the tensile transverse direction. This ply, thus, will be an object of the optimization and, if unnecessary, removed.

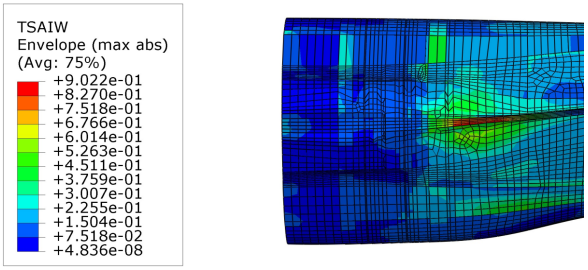

Figure 4.13: Region A defined in Figure 4.12 under edgewise loading towards the leading edge without Unifillo ply.

Generally, it can be seen that there is no failure occurring when disregarding the Unifillo ply along the spar cap and modelling artifacts. In future work, the areas disregarded as artifacts should be investigated more closely using more detailed FEM-models or component tests. For the sake of this report, they can, however, be excluded from the analysis. There is a high potential for improvement, as in all loading directions, the failure index stayed below one, and multiple regions are far away from that limit.

4.3.2. Deflection analysis

To check the stability under ultimate loading, the deflection and tower clearance under ultimate loads are important to verify that a blade can be used in operation. Because the E-3120 turbine is a downwind turbine, the tower clearance criterion is not as significant. The upwind loading direction could, however, still result in a violation and is thus checked in this subsection. The turbine and the HAWCStab2 coordinate systems can be seen in Figure 4.14.

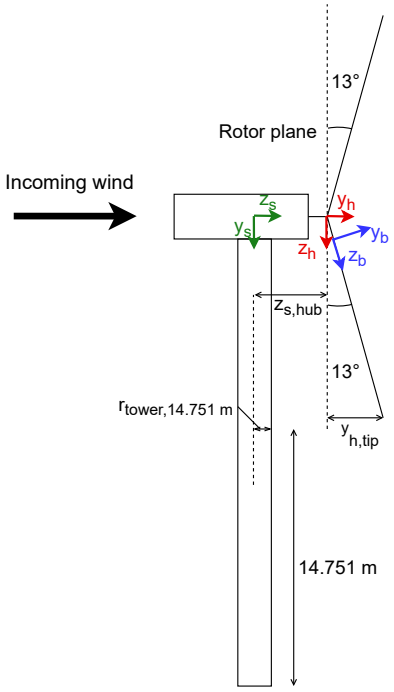

Figure 4.14: Sketch of coordinate systems in HAWC2.

The FEM model coordinate system coincides with the blade coordinate system shown in Figure 4.14. The tower clearance can then be calculated using Equation 4.1.

$$tc = y_{h,tip} + z_{s,hub} - r_{tower,14.751m} \tag{4.1}$$

$z_{s,hub} = 1.116$ m is the distance between the tower centerline and the hub center. The tower radius at $h_{hub} - r_{rotor} = 14.751$ m, which is 0.461 m, is subtracted to result in a conservative estimate of the tower clearance. The radius is interpolated from the Flex4 input data.

Table 4.4 shows the maximum deflection values under the flapwise and edgewise loading in the FEM-coordinate system. The magnitude and the y- and z-deflections are described. Figure 4.14 shows how the FEM-coordinate system, with the z-direction along the uncurved, undeflected blade, differs from the rotor coordinate system in HAWCStab2 due to the coning angle of the blade of 13° and a fixed pitch of 1°. In

this report, the pitch angle is considered negligible due to its small value. The coning angle, however, requires a coordinate transformation with a rotation around the x-axis, as can be seen in Figure 4.14. The deflections in the y-coordinate of the HAWCStab2 rotorplane are then calculated from Equation 4.2 with $\theta = 13°$ and are shown in Table 4.4 with the resulting tower clearance. The tower clearance is calculated using Equation 4.1.

$$\begin{bmatrix} y_{HAWCStab2} \\ z_{HAWCStab2} \end{bmatrix} = \begin{bmatrix} \cos(\theta) & -\sin(\theta) \\ \sin(\theta) & \cos(\theta) \end{bmatrix} \begin{bmatrix} y_{FEM} \\ z_{FEM} \end{bmatrix} \tag{4.2}$$

Table 4.4: Deflection under prescribed loading and resulting tower clearance.

Deflection [m]	Magnitude FEM	U1 FEM	U2 FEM	U3 FEM	y_h-deflection HAWCStab2	tower clearance
Flap downwind	0.769	0.052	0.767	0.005	0.746	3.628
Flap upwind	0.541	-0.037	-0.54	-0.004	-0.525	2.357
Edge trailing	0.038	-0.037	-0.011	0	-0.011	2.871
Edge leading	0.067	0.064	0.019	0.001	0.017	2.899

These values have to be compared to the allowable tower clearance, which can be computed from the undeflected state Equation 2.11. The clearance of the undeflected state can be calculated using Equation 4.1. The y position is found using the coning angle of 13° and the rotor radius from $y = r_{rotor} \cdot \sin 13$. This results in a tower clearance in the undeflected state of $y_{tc,undeflected} = 2.882$ m. It results, with the partial safety factors of $\gamma_f = 1.35$, $\gamma_m = 1.1$ and $\gamma_n = 1$ for the case DLC 1.3 and not tested material properties, in an allowable tower clearance of 0.94 m. It can thus be seen that there is no violation of the tower clearances under DLC 1.3 loading, and there is stiffness reduction potential in the optimization phase.

5 Discussion

The original blade was successfully modelled in this first part of the thesis. During the modelling parts of the global research goal to find a successful redesign of OLW934 with reduced mass and maintained structural integrity, some answers could already be found. These will be discussed in this chapter, as well as potential error sources and recommendations for future work.

5.1. Answers to research questions

One of the subquestions defined in section 2.6 was investigated in this first part of the thesis and can already be answered.

How is the performance, structural, and aeroelastic of the original design?
In the analysis, it was found that the original blade does not suffer failure when excluding the Unifillo material from the analysis. It was seen that the most significant loading direction is the downwind loading, with a maximum failure index of $I_f = 0.87$. In this direction, it was found that the highest loaded areas are in the root area, where the circular cross-section transfers into the airfoil shape of the blade. This area fails in transverse compression, indicating that in the outer layers of this region, Biax or Triax material should be used to account for the loads. In the longitudinal direction, it was found that the UD material in the spar cap can be reduced in this area. Also, the rest of the blade showed mass reduction potential in the spar cap region, because the resulting failure index stayed below a value of $I_f = 0.75$ when excluding modeling artifacts. The same findings were obtained when analyzing the flapwise upwind loading direction. In the edgewise loading directions, the highest loaded area is the trailing edge region where the trailing edge reinforcement UD ply fails in transverse loading, again emphasizing the need for Biax material in the skin. The rest of the trailing and leading edge regions are at very low failure values, resulting in the potential to save mass by reducing the leading and trailing edge reinforcements, as well as the sandwich structure material used in the blade.

When analyzing the aeroelastic behaviour of the E-3120 turbine with NorZet rotor, a usual behaviour of a stall-regulated downwind turbine with fixed rotor speed was seen. The maximum power found coincides with the rated power of the turbine of 80 m/s. Using the conducted analysis, the maximum loading was found to be applied

on the blades. Under the max loading, the turbine showed no tower clearance issues and no failure, as explained before. Additionally, it was found that no instability due to resonance is apparent, showing that the original OLW934 blade could be used on the E-3120 turbine with NorZet retrofits in operation if the bed plates and shafts were sufficient to hold their weight. To enable their use also on the E-3120 turbines with the original bed plates and shafts, the mass reduction on the blades will be investigated in the second part of the project.

5.2. Potential error sources

Potential sources of error can be found in various stages of the optimization process. The first stage is the setup of the original blade. The potential error sources during this first part of the project are discussed in this section.

In the original FEM-model, several assumptions regarding the representation of the original box girder structure were made, because a shear web version of the box girder blade was necessary to import the result into the ShellExpander. This was needed to load the FEM-blade into HAWCStab2. Also, the position and width of the spar cap and shear webs were imported from the DTU-made design for the OLW965 blade, which could not be up to date with the OLW934 blade. When importing the blade planform, the OLW965 blade was also used as the base with an alteration in the tip area. This could not resemble the OLW934 planform exactly and result in a structural and aerodynamic mismatch with the real blade. Additionally, the assumptions in how the material properties and thicknesses were estimated can have errors resulting in non-realistic stiffness, mass, and failure index results. These materials were also used in the setup of the following models and would introduce the error there, too. Another source of error in the original FEM-model is the way the loading is applied. Even though the forces are calculated for specific z-positions along the blade, they are applied over a length of several centimeters to reduce the induced stress concentration. Additionally, the four applied forces will not result exactly in the intended bending moment distribution. Between the force application points, the bending moment will have a linear change, which is an assumption from the quadratic polynomial bending moment distribution intended. The stress concentrations induced at the load application points also influence the field output, and the areas are neglected from the analysis. This, however, could result in the accidental neglect of relevant results in the same area. Also, the fully fixed boundary condition does not resemble reality, as in reality, the hub and turbine are not rigid bodies, which can deform and move. In the meshing of the blade, there are also potential sources of error. Moreover, linear four-node elements with reduced integration and hourglassing control are used, which are less exact than quadratic elements, as more nodes and integration points exist. This assumption will be validated in the meshing of the redesigned blade. Also, the mesh convergence done on the redesigned blade is used as validation for the original blade's design. This could result in the use of an insufficient mesh size in the original design. Additionally, highly loaded areas with too coarse meshes might induce inconsistent results. The application of the extra masses as engineering constants in the described regions could also induce error. There could be inherently wrong estimations of the amount of extra masses added, because they are also based on estimations made by Olsen

Wings A/S. The total blade mass of the models and the real blades is, however, in good agreement, showing that this error is most likely minimal. Additionally, the error in the placement of the extra masses is likely minimal because the position of the shear center is also compared and validated with real blade data. Lastly, the tip break is not modeled, and its stiffness is assumed by introducing shear webs in the tip area. This does not resemble reality and could influence the stiffness and mass of the blade and thus its eigenvalues and aeroelastic behaviour.

In the next stage of converting the FEM-blade into HAWCStab2, the introduction of errors is also possible. The first big assumption made is applying the extra mass distributed over the outer shell, which, as discussed in subsection 7.6.3, could alter the blades' eigenfrequencies. Additionally, there is only a certain number of cross sections defined to be imported into HAWCStab2. This will inherently induce some error by interpolation. The reference point for the cross-sectional property calculation in BECAS is found by measuring the half distance between the trailing and leading edges at each partition adjacent to the cross-section. The value is thus not evaluated in the center of the cross-section, inducing a small error. In the next step, the cross sections are imported into BECAS and then into HAWCStab2. During this process, all cross sections are reassembled, and the coordinate systems are changed. Small inconsistencies in the programs could change the original blade's cross-section and its properties.

In the load and aeroelastic analysis in HAWCStab2, some potential sources of error are apparent. When implementing the structural and aerodynamic input files, data from the Flex 4 model made by NorZet is used. The Flex 4 data might already have been generated using assumptions that are unknown; thus, the input could be a source of error. Additionally, HAWCStab2 requires the definition of the hub, tower top, and shaft properties. Some of these were approximated by using the data from the Vestas V27 turbine. Because no sufficient controller model was available, the rotational speed of the shaft is fixed; this might unrealistically neglect vibrations or operational data variations. Additionally, because of that, no turbulent simulations were possible to run with the model. The results from the analysis from Norwin Ltd were used instead; the assumptions made in that model are not known and could also impose an error. The loads found from this analysis are only root bending moments. The bending moment over the blade span was approximated with a quadratic polynomial used in DTU. This will thus inherently impose an error in comparison to the moment distribution in reality. When checking the tower clearance with FEM basic calculations are used to calculate the tower clearance with an estimated tower thickness, imposing small errors. Additionally, in the conversion from the FEM-result into the HAWCStab2 rotor coordinate system, the pitch of the blade was neglected.

Next to inherent inconsistencies and assumptions in the used programs, this completes the analysis of the potential error sources in the original design. The optimization is based on the FEM and HAWCStab2 model of the original blade; when there are already errors introduced, they will affect the following redesign process. To minimize that risk, the FEM-blade and HAWCStab2 mass output is compared to real blade data.

Additionally, the center of gravity is checked against the blade data found in real life. The representation of the original OLW934 blade is thus considered to be sufficient and can be used as a base for the following redesign process.

5.3. Recommendations for future work

To validate the results from the original OLW934 FEM-model, the areas disregarded due to modeling artifacts should also be tested using, for example, component tests. Next, the mass distribution should be applied more realistically, and a study on the stiffness and mass in the tip region should be conducted to find the correct eigenvalues of the blade with a tip break and validate the aeroleastic stability result further. Also, the found blade file should then be checked under turbulent loading to compare the results found to the ones using the existing blade inputs, to analyse possible differences, and validate the found blade model.

Part 2: Redesign OLW934

6
Methodology

The second part of this report describes the redesign process of the OLW934 blade. The redesign is done based on a structural and aeroelastic optimization using the OpenMDAO-based optimization tool AESOpt, developed by DTU Wind and Energy Systems, as explained in subsection 2.2.3. In this project, only part of that framework is used. The AESOpt inherently includes the cross-sectional finite element tool BECAS and the aeroelastic solvers HAWCStab2 and HAWC2. For simplification purposes and faster convergence times, the aeroelastic analysis is excluded from the optimization itself during this project. After the completion of the structural optimization, HAWCStab2 is used manually to check the resulting design. Additionally, during the process, a full-scale FEM-model using Abaqus CAE is used to validate the structural validity of the resulting design. Figure 6.1 shows the resulting workflow of the optimization process in this second part of the project.

First, four input files are created using the original blade planform and layup with four different internal structures. These input files are then loaded into the optimizer AESOpt. This step in the process is where the optimization tool AESOpt from DTU Wind is used. The optimization objective, constraints, and variables are defined. The optimization is run for these four input files, and the resulting blade structure gets transferred into the pre-existing HAWCStab2 model developed in Part 1 of this project. Using the HAWCStab2 model, the loads and aeroelastic behaviour of the turbine with the new blade are then calculated. The load difference is analyzed next to determine if the new blade significantly changed the loads. Also, the eigenfrequency placement is checked against the excitation frequencies to determine if the blade can be used in a safe operation. If the change in loads is not sufficiently small or there is a dangerous eigenfrequency, a new setup of the optimization parameters is done, and the optimization loop starts again. If these requirements are met, a decision between the four designs is made based on their weight saving. The chosen blade design layup is discretized and put into an FEM-model to check for buckling and failure under ultimate loads and tower clearance. If the design fails, some minor layup adjustments are made and rerun; if there are none, the final design is checked once more in HAWCStab2 for its aeroelastic stability. When all tests are sufficient, the completed design is found.

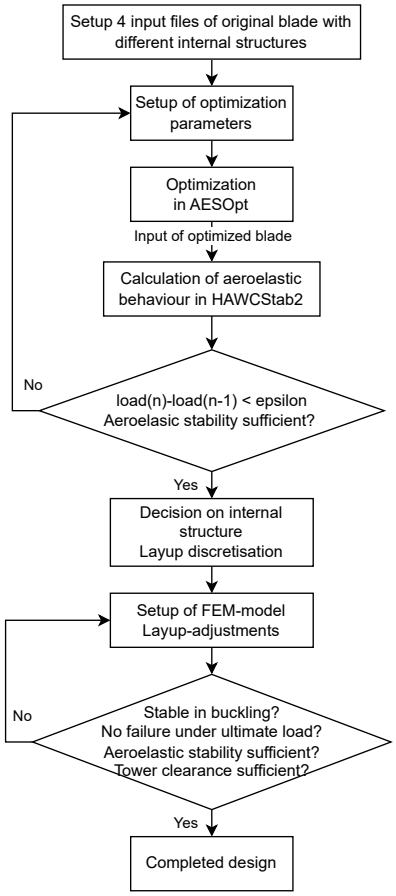

Figure 6.1: Work flow of the redesign of blade OLW934.

6.1. Setup of input files for optimization process

The first step in optimizing the existing OLW934 blade is to set up a windIO file with its planform, internal structure, materials, and lay-up, which is used as a baseline in the following optimization. Then, three more files are made with different spar cap widths and shear web distances to be optimized. These four files are the input files for the optimization. The setup of these files is described in this section.

6.1.1. Blade planform

The first part to include in the files is the planform information of the blade. This is done using the *windIO_converter* package developed by DTU Wind and Energy Systems. This package enables the conversion between HAWC2 and windIO files, keeping in mind their different coordinate systems and reference axes. While the data in HAWC2 is defined based on the half chord defined in the c2_def axis presented in Figure 3.10, AESOpt uses the half chord position at z=0 as the reference point. The two different

reference axes are shown in Figure 6.2a. Additionally, the coordinate system of the blade is different in the two software, as can be seen in Figure 6.2b.

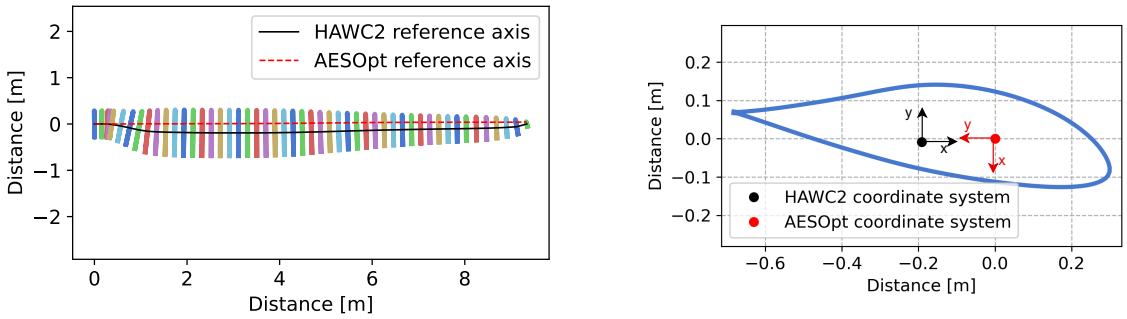

(a) Planform OLW934 view on suction side.

(b) Cross section OLW934 view from trailing edge.

Figure 6.2: Difference in the reference axes of HAWC2 and AESOpt.

The structural, aerodynamic, operation, and *.htc* files from the HAWCStab2 model developed in part 1 are input to a conversion script. This script reads those files and writes the blade planform parameters in the windIO file. This includes the airfoil position, new reference axes, chord, twist, structural pitch axis, and the thickness distribution. The converter package also includes the other structural components of the turbine and the airfoil polars in the output windIO file. Because in this project the resulting blade design is fed back into the original HAWCStab2 model, these are unnecessary for this project's windIO file and can be deleted. The script also includes a block containing the blade's elastic properties, enabling a planform optimization without having to define lay-up. As this project's main purpose is to find an optimized internal structure and lay-up, a lay-up definition is necessary, and the block of elastic properties is also deleted.

To complete the blade planform setup in the windIO files, the airfoil geometry of the airfoils used in the blade is necessary, which is not defined in HAWCStab2. The airfoils used in the OLW934 were also used in the design of the OLW956, made by DTU Wind and Energy Systems. Those airfoil coordinates are thus added to the windIO file. This completes the setup of the blade planform. Figure 6.3 shows the resulting blade planform in three different views from the tip, the trailing edge, and the suction side. When comparing this planform to the original blade planform in Figure 2.12, it can be seen that they are in good agreement.

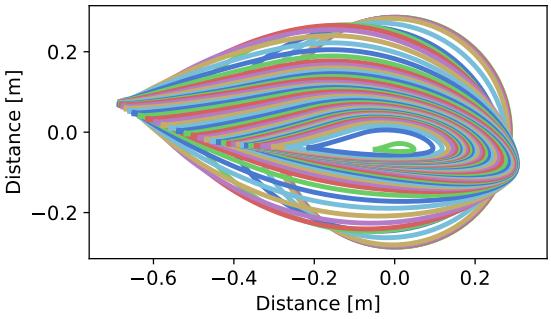

(a) Cross section OLW934 view from tip.

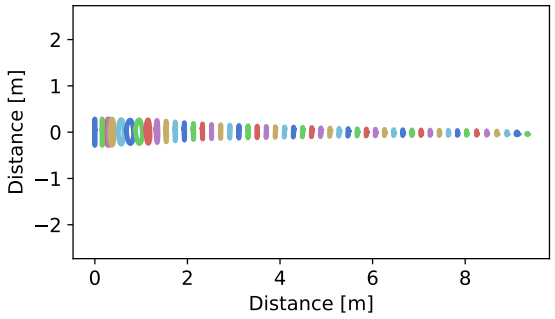

(b) Planform OLW934 view from trailing edge.

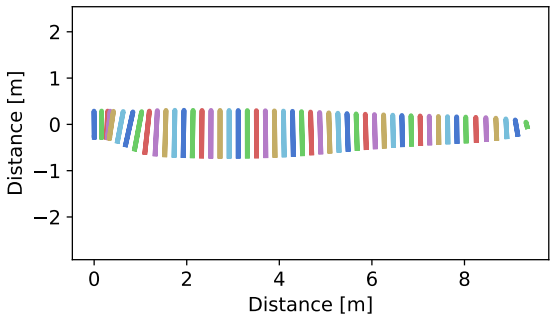

(c) Planform OLW934 view on suction side.

Figure 6.3: Blade planform of OLW934 in AESOpt model, imported from HAWCStab2 and visualized with cross sections.

6.1.2. Internal structure

The next step is to include the internal structure in the windIO files. This includes the shear web placement, the spar cap width, the placement of different lay-up regions, and their material definitions. All four input files are defined to have the same layup regions and the same material definitions. They differ in the spar caps' width and the shear webs' distance.

Definition baseline design

The input file created based on the spar cap width of the original OLW934 blade will be the baseline of the optimization process. However, as described earlier, it does not exactly resemble the internal structure of the original OLW934 blade, which was made in a box girder design. Nevertheless, this assumption is chosen due to constraints of the software tools and primarily also because the new blade is intended to have a shear web design instead, saving weight due to less adhesive used.

- The shear webs' y-position (windio coordinate system) is adjusted. In the original design, as seen in Figure 3.6b, they are part of the box structure. As a result, their position is first at a greater distance from the mid-point than the half width of the spar cap, and as the blade gets slimmer, lastly, at the same distance. The shear webs are placed in the spar cap region in this design.
- The region order in the lay-up is changed through the thickness. Instead of having the complete shell lay-up on the outside, only the outer half of the shell

lay-up is on the outside in this input file. This is followed by the core material, the spar cap layups, and the trailing and leading edge reinforcement regions. The other half of the original shell lay-up is used as an inner shell.

All of the changes in the cross-section design can be seen in Figure 6.4, where the defined internal structure is shown exemplary at a spanwise position of z=3.87 m.

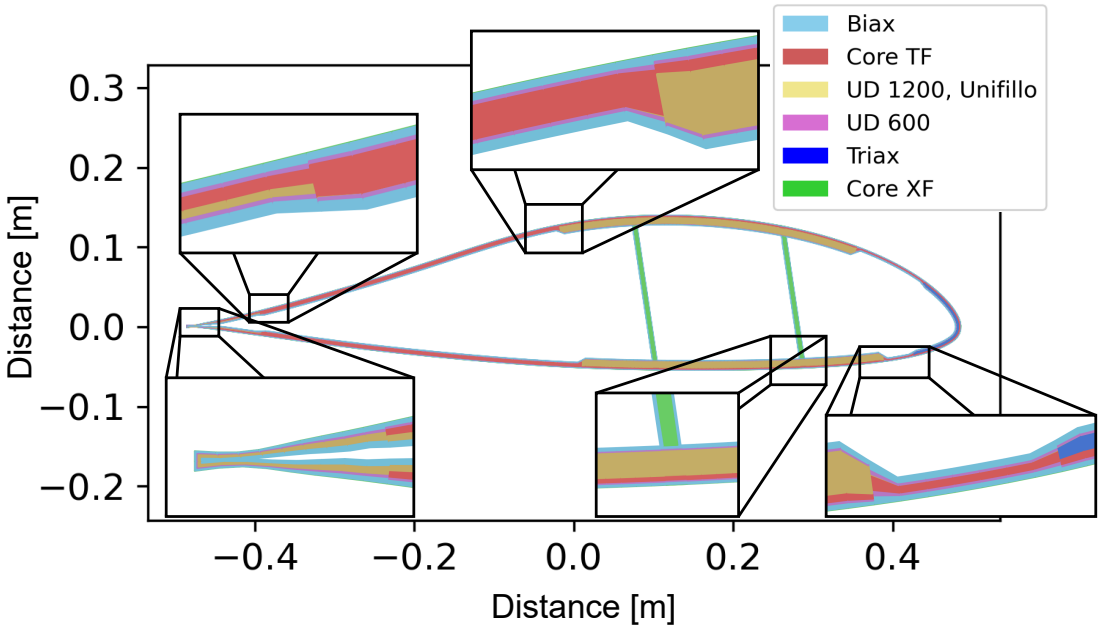

Figure 6.4: Layup regions in the original OLW934 blade at spanwise position z=3.87 m.

The changes were made to result in a reasonable shear web design.

The y-position of the shear webs was adjusted because, in a shear web design, they are usually placed in the spar cap region to distribute the forces over the blade most effectively. When placing the shear webs in the spar cap region, the shear forces can be applied on the strong spar cap laminate instead of the skin, which usually has significantly lower strength. The change was necessary, as the original choice of web placement was made with regard to a structurally different spar design concept. Additionally, the bonding of the flanges is easier in the manufacturing process when the shear webs are only placed inside the spar cap region.

To determine where the shear webs are placed, first, an approximation of the spar cap width along the blade is made based on the original design. In the original design, the width of 0.4 m is kept until a spanwise position of z=2.43 m, because a wider spar cap is needed to withstand the bending moments in the root area of the blade. z=2.43 m is the spanwise position where the shear webs first have the same distance as the spar cap width. The spar cap width reduces after that. The same is done in the definition of this baseline input file. At the tip cut position z=8.04, the width of 0.16 m and

a shear web distance of 0.11 m is defined to comply with a requirement set by Olsen Wings AS to have a minimum distance between the webs of 100 mm until the tip cut to enable the assembly of the tip shaft. Between these two widths, the optimizer AESOpt automatically puts a smoothed curve. The resulting width over the length of the blade can be seen in Figure 6.5. The resulting web distance in comparison to the spar cap width is also shown in Figure 6.5. At z=0.317 m, the shear web starts as defined in the original blade. It is placed with an offset to the y=0 position of 0.15 m, which results in a shear web distance of 0.3 m. This is done to leave a distance margin of 0.1 m between the width of the spar cap and the distance of the shear webs. Because their center position coincides, this results in a 0.05 m distance between the shear web and the end of the spar cap, to ensure safe bonding in the flange areas. A linear reduction in the distance between the webs is chosen to result in a plane shear web, which is easier to manufacture. The shear web is stopped with the spar cap at the tip cut at the above-mentioned width and distance.

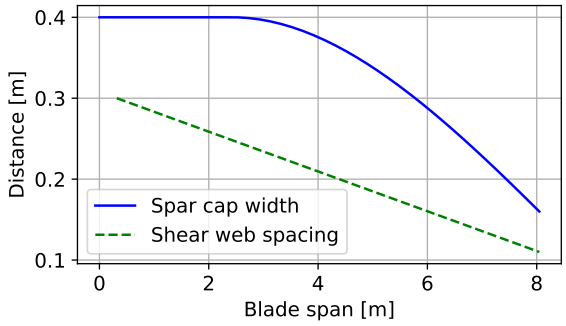

Figure 6.5: Spar cap width and distance between shear webs for the original blade OLW934.

Moreover, the region order is changed through the thickness to adjust to the different spar design choices. As shown in Figure 2.6, in a shear web design, the outer shell is set up using an inner and outer skin and placing the cores, spar caps, and the leading and trailing edge reinforcements in between. The lay-up regions can be seen in Figure 6.4. In the box girder design, on the other hand, the Biax material shown in Figure 2.6 is all part of the outer skin, and the UD 1200 material, which builds the spar cap, is glued in from the inside of the cross section, as these layers are part of the box girder layup.

The two skins defined in the baseline design consist of Biax material and a layer of UD 600. In the outer skin, a thin layer of Soric TF material is part of the layup, as it was used in the original blade's shell layup. Inside, starting at the leading edge, triax material is placed as reinforcement. The original blade layup has no leading edge filler between the leading edge reinforcement and the spar cap. Next, the spar cap layup consisting of UD material is placed as explained before, followed by the leading edge filler, consisting of Soric TF core material. No Soric TF material is used anymore in the trailing edge region, and UD material is used as trailing edge reinforcement. The shear webs consist of Biax skins and Soric XF as core material to increase their area moment of inertia. These regions' thicknesses are optimized in the following optimization.

When using the original thicknesses of the OLW934 blade, the total mass of the baseline blade is found to be 330.62 kg, which is only 0.98 % different from the median weight of the blades manufactured in reality.

Definition of 3 extra input files

In addition to the baseline design, there are also three other input files with different internal structures optimized in this report. These include the same data as the baseline file, but differ in the width of the spar cap and the distance of the shear webs. The different spar cap and shear web curves for the four input files can be seen in Figure 6.6.

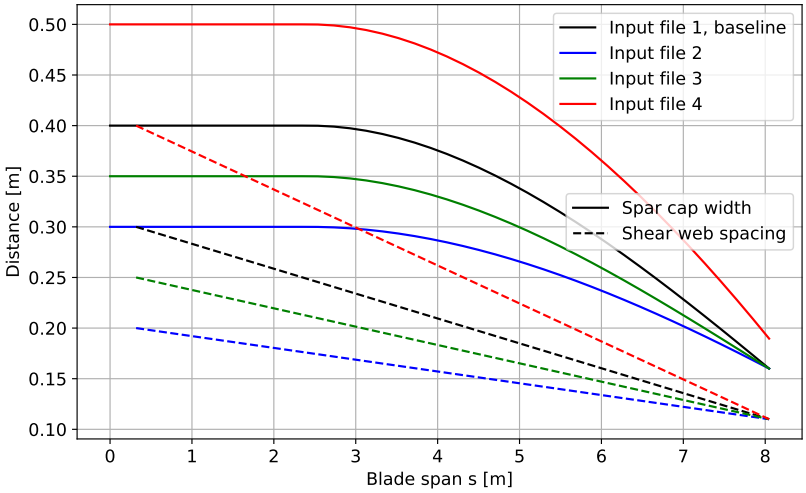

Figure 6.6: Spar cap width and shear web spacing of the four different input files.

Three different root spar cap widths of 0.3, 0.35, and 0.5 m are used. The spar cap width stays constant until z=2.43 m and gets smoothened from AESOpt between that point and the tip cut position. The tip cut position is determined by Olsen Wings' requirement of at least 100 mm distance between the shear webs at that position. To ensure safe bonding of the shear web on the spar cap, a minimal distance of 2.5 cm on both sides between the shear web and the outer edge of the spar cap is kept at the tip cut position at z=8.04 m. For the spar cap designs in input files 2 and 3, this measure results in the same spar cap width as the baseline design of 0.16 m. The input file 4, however, keeps a higher margin due to a higher initial spar cap width. It was chosen to use these general behaviours to find the most effective root spar cap width for the design of the OLW934 blade. The investigation aims to answer the question of whether a higher or lower spar cap width results after thickness optimization in lower blade mass while keeping the blade's structural and aeroelastic integrity. In this study, the spar cap width is kept constant until z=2.43 m for all designs. This is done to withstand the bending moment in the root area of the blade. In this report, the same spanwise position is used as in the original blade. A study on which spanwise position to start the width decrease should be done in future design iterations. The spanwise position z=2.43 m is, however, kept fixed during this study due to limited

computational time available.

Also, the general behaviour of the shear web is kept the same as the original, starting at z=0.317 m and following a linear curve. Their y-position in the windIO coordinate system is determined by the width of the spar cap. At the root, its position is set to be at a distance of 0.05 m from the edge of the spar cap to ensure safe bonding, while maximizing its distance to the other shear web to increase the stability of the blade.

Higher spar cap widths and thus also bigger shear web distances are expected to have intrinsically better blade stability, but also higher mass. The smaller width designs might, however, have to account for their lack of stability with thickness and thus mass increases. Finding the compromise between these factors will be the aim of this study. Figure 6.6 thus shows the chosen spar cap and shear web combinations to be optimized for layup thickness.

6.2. Setup of optimization script

The optimization uses the baseline design described before. The baseline model is, thus, run first. The windIO file is loaded in, and the splined planform is added as a subsystem. Also, the structural subsystem is defined with mesh and BECAS options used when the cross-sectional mesher (CS_mesher) and BECAS are called in the framework. The structural subsystem is also added, and the two subsystems get connected, so that the structural subsystem can also access the reference axes and planform parameters. The subsystem of ”strains” is added to the problem next. It uses the StrainRecoveryGroup class and enables the display of the strain response of all elements in each cross-section and their strain failure index using the strains calculated in BECAS. Thus, the subsystem strains get connected to the BECAS strains. Before the run command is the last step, adding the loads vector containing the loads found in section 3.3. After the run command, the resulting output case is defined as the baseline.

A similar structure is used in the following optimization part, where the four different input files are loaded. The optimization parameters are added between the steps of connecting the strains subsystem to the BECAS strains and connecting a recorder. The objective of this optimization is to reduce the weight from the baseline design without compromising the blade’s structural integrity. In the optimization script, the objective is thus added. To increase the stability and efficiency of the optimizer, the order of magnitude of the design variable and the objective function should be similar. The design variables are in this case the layup thicknesses with an order of magnitude of $\sim 0.01 - 0.001$ m, and the objective function is the mass with an order of magnitude of $\sim 1 - 100$. Because these differ significantly is the blade mass in the framework scaled by $0.1/m_{baseline}$, bringing the value down to the order of magnitude of 0.1. This is used for the optimization procedure internally; the result is at the end of the optimization automatically multiplied by the inverse of the scaling factor, eventually resulting in the resulting blade mass in kg in the output.

6.2.1. Design variables

The design variables used in this project are the thicknesses of the layers defined in Figure 6.4. The spar cap widths and shear web distances are changed manually in this framework by running the four different input files in the optimization. This is done to decrease computational time and stabilize the optimization process. Because they are constrained to many parameters, optimizations, including the width of the spar cap and the distance of the shear webs, have difficulty converging. For example, the spar cap has to be slim enough so that it does not overlap with the leading or trailing edge reinforcements, but wide enough to result in a reasonable shear web distance. Also, the shear web is supposed to be a straight line for manufacturing purposes, and its distance from the other shear web can not be wider than the spar cap's width. A manual approach is thus chosen, and in this report, the four designs shown in subsection 6.1.2 are checked.

The design variables defined in the optimization script are the thicknesses of the layers. For the layers in Figure 2.6, first, splines are defined. They are smooth curves with control points along the blade span that are evaluated by the optimizer and an interpolation scheme between them. This report uses 5 control points per spline, which results, with 16 design layers, in a total of 90 design variables. The Bezier method is used as an interpolation method. For these splines, design variables are defined in the optimization script with lower and upper thickness variation bounds limiting the optimizer's range. The bounds describe the allowable change of the resulting thickness of the specific layer from the baseline design. Because some layers are considered necessary for the structural integrity of the blade, they are set to have a lower bound of 0, making it only possible for the optimizer to increase their thickness or otherwise maintain the thickness of the baseline design. This is done for the skin Biax layers. The other layers' bounds are defined in a way that their thickness can increase, but also decrease.

6.2.2. Constraints

Next to the design variables are also constraints necessary for a successful optimization setup. Constraints define specific events that are not allowed to occur, for example, that the thickness of a layer is not allowed to fall below zero.

The main constraint in this project is that the blades' structural integrity needs to be maintained. To achieve that, constraints limiting the maximum strain failure index of each cross-section to 1 for each load case are introduced. In Aesopt, only the axial strain failure index can be used. Thus, a check for the other directions will be done in the resulting blade FEM-model.

Next to this design constraint are also constraints introduced to keep the optimizer stable and not result in negative stiffness or mass results. For all layers that are not already limited by a lower bound of 0 in the design variable definition, minimum thicknesses of 0 are set as a constraint.

Lastly, to result in an easy-to-manufacture design are the layers with more than one in-

tegration point constraint, resulting in reduced thicknesses over the blade span. This is done by introducing a differential subsystem for each layer and constraining it with an upper bound of 0.

After defining the constraints, the optimization driver options are lastly defined in the optimization script. The gradient-based optimizer Sequential Least Squares Programming (SLSQP) is used to solve the problem, because gradient methods, as explained in subsection 2.2.3, have fast convergence times and result in good solutions when the input is not very far off initially. It is a sequential quadratic solver (SQP), which, as described in subsection 2.2.3, usually results in faster convergence times than linear solvers [70]. Because the original lay-up is used as the input for the optimization instead of building the lay-up from zero, this is considered to be true. After defining the tolerance and max iteration number, it is defined that the optimizer should approximate the gradients with finite differences to enable the use of Becas strain constraints. Becas requires the use of the approximation, as its analytical gradients can not be used in the current version. After attaching the recorder and the setup and run command, is the result saved as opt. The two different designs can then be compared by calling the case names baseline and opt.

6.3. Transfer to and calculation in HAWCStab2

In order to test the aeroelastic behaviour of the turbine with the new blade, the newly found blade structure is written into a blade_st.dat file. This file is then used in the already developed HAWCStab2 model, described in section 3.2. Following the steps in section 3.2, the steady states are recalculated in HAWCStab2 and an aeroelastic Campbell diagram is generated using HAWCStab2.

Because the turbine is a downwind turbine, no problem with the tower clearance is expected. The upwind loading will be the most critical. In HAWCStab2, the upwind deflection can not be checked because the blade does not deflect in the upwind direction in a steady state scenario. During this optimization procedure, the tower clearance is thus verified at the end of the procedure in a FEM-analysis and not considered in this step of the optimization.

Also, the steady-state root bending moments are compared between the calculations with the two different blades to see how the loading on the blade changes. When the difference in flapwise and edgewise bending moment is higher than 2%, the loads in the optimizer are updated and the optimization is rerun. In section 4.2, it was, however, found that only the downwind flapwise loading can be approximated accurately using the described approximation for the ultimate loads from the steady states. Because this one also drives the design by having the highest failure indexes, it is found to be reasonable to use an approximation for the other load cases. The percent difference between the calculated bending moments with the two different blades in steady states is applied to the design loads obtained with the original blade to get the design loads with the new one.

The last thing to check is the eigen frequency placement found with the new blade. If

the endangered frequency of flapwise backwards whirling defined in subsection 4.1.2 is higher than or equal to that of the original blade, the new blade is considered to be stable.

When there is too high a difference in load or when the tower clearance and frequency placement are insufficient, the optimization is rerun. In the case of insufficient frequency placement or tower clearance, an extra constraint is introduced, limiting the minimum stiffness of the blade to solve that problem.

When all requirements are met, the found optimized design can be used in the next steps. This framework results in four optimized designs. The design with the lowest blade mass that still complies with all constraints is chosen to be used in the following discretization and FEM setup.

6.4. Discretization of Layup

The last step to a complete structural design is the discretization of the found lay-up. Because the optimizer results in a continuous thickness distribution over the blade span for each layer, which is not realistic as plies have distinct thicknesses, the thickness of each layer has to be discretized. This is done by rounding up ply thicknesses and using engineering understanding to determine if certain ply thicknesses can also be rounded down. This process will result in a slightly different mass and stiffness distribution. The internal structure and lay-up are used in the following step of setting up an FEM-model of the redesigned OLW934 blade.

6.5. FEM-setup

To verify that the new blade design is stable against buckling and does not show failure under the ultimate loads in the transverse direction, a FEM-model is made with the result of the optimization.

The new FEM-model is set up utilizing the same steps as in the original blade model. The blade planform is loaded using Python scripts and the same cross-sectional data as in the original OLW934 blade, because the outer planform stays the same. Next, partitions are made at cross sections optimized in AESOpt. At these cross sections, using the enter parameter tool, the *start_nd_arc* and *end_nd_arc* positions of the spar cap width from the Windio file are defined in Datum points along the blade cross sections circumference in the FEM-model. These are then used to generate partitions that build the spar caps' outer edges along the blade span.

The shear webs are introduced accordingly. The start and end arc positions from the windIO file at z=0 and z=8.04 are defined using the enter parameter function to introduce datum points. These are then used to create a partition along the blade length where the shear web is situated. This is done at all four shear web positions along the circumference of the cross-section. The two partitions on the pressure side are then connected using the shell loft feature to the two partitions on the suction side, resulting in the two shear webs.

The layup is defined in the next step using the same materials as defined in the first FEM-setup. Also, the meshing, constraint, and simulation setup are done according to section 3.1. The application of the extra masses is, however, adjusted to the new blade design. While the application of the gel coat, the root nuts, and the tip break are done the same, the area and mass of the adhesive are different in the new design. In the box girder design, the entire beam has to be glued into the skin, while in the new design, only the flanges of the shear webs are glued, which have a significantly smaller surface. In Olsen Wings' documentation on the use of adhesive, it can be seen that they use 2 kg of adhesive to glue the two box girder parts on both the trailing and leading edges. This number is used to estimate how much glue is necessary to glue the shear webs. Because there are four flanges, 8 kg is assumed to be needed. For gluing the outer two shells, 2 × 2 kg is also estimated. To be conservative, 2 kg is also added for the tip shaft reinforcements, and 2 kg more for the implementation of the tip break itself. This results in an adhesive weight of 16 kg. To use a conservative estimate, this number is rounded up to 20 kg of adhesive. This is thus a reduction of 42.03 % in adhesive mass. This weight is applied to the model as shown in Figure 6.7. The flanges of the shear webs are assumed to be 5 cm in width. In this area, the weight is applied, as well as on the trailing edge and tip break area. Because the flange area at the leading edge is significantly smaller, in this report, the extra weight of the adhesive is not applied there.

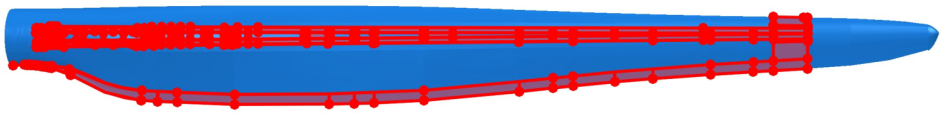

Figure 6.7: Adhesive engineering constant application in redesign FEM model.

This model is then run for the different load cases defined in subsection 4.2.2 and an eigenvalue analysis is done.

6.6. HAWCStab2-setup

In order to check the final design for its aeroelastic stability, it is again transferred to HAWCStab2 using the preprocessor tool ShellExpander and BECAS. For that, following the process of the original OLW934 blade, a version of the FEM model is made, which uses a constant layer of minimal thickness as the outermost layer of the shell. It has minimal stiffness, very high strength, and results in the same mass as the applied engineering constants. Figure 6.8 shows the cross sections to be analyzed in shellexpander and BECAS. It can be seen that the distance between the cross sections is wider than 0.2 m, as done in the original blade design. However, it is estimated to be exact enough to have a high resolution in the blade root area, where the geometry changes significantly, and reduce the resolution towards the tip, where the cross-sectional geometry does not change significantly. In between the cross sections, HAWCStab2 interpolates the blade properties. For these cross sections, the half chord point is found and used to define the reference axis for the following stiffness and mass calculation in BECAS. The cross sections and the centerline coordi-

nate system are used as inputs to the shellexpander, which results in 2D BECAS input files.

Figure 6.8: BECAS cross sections redesign.

In a script as explained in subsection 3.2.2, the values for the HAWC2 Blade_st.dat file are calculated and then exported into the HAWC2 input file. At the tip of the blade at r=9.34 m, the values computed at the last cross section at 8.46 m are applied to result in a completed input file. This is considered reasonable because the cross-section does not change significantly after 8.46 m and because the tip region is not implemented realistically intrinsically, as the tip break system is missing. The new input file is then run in the existing HAWCStab2 model, described in section 3.2, and the aeroelastic stability as well as the loads and the tip deflections are checked and compared to the results of the previous design stages. When the new design shows no problems, it is found to be the redesigned OLW934 blade, if not a reiteration of the layup in the FEM-model is done.

7

Results and Analysis

The results of the redesign process are shown and analyzed in this section. The redesigned internal structure of the OLW934 blade is described, and its structural and aeroelastic performance are analyzed.

7.1. Validation of input design choices

As explained in subsection 6.1.2, there are significant changes made between the original design in the first Abaqus FEM model, which resembles the box grider design, and the AESOpt baseline design, which already includes the changes in the internal structure explained in subsection 6.1.2. While the spar cap width and the material layer thicknesses are the same in both designs, the layer orders and the shear web placement are adjusted to a shear web design. The two designs are compared in this section to validate the newly implemented internal structure with shear webs.

Figure 7.1 shows a comparison between the two designs of their mass distributions in Figure 7.1a and their bending stiffness distributions in Figure 7.1b. The mass plot shows very similar behaviour for both models. It can be seen that the Original blade design has a slightly higher mass at the root of the blade. After that, it can, however, be seen that its mass stays below the one from the Baseline design until around three meters. From three meters to the tip, the two curves are almost identical. The deviation before three meters can be explained by modeling simplifications, as well as the new region definitions of the layups. In the baseline design, the transitional layup defined in the original FEM model is not included, and the sandwich structure in the trailing edge region instead directly connects to the spar cap, which could change the mass distribution. Additionally, the layup defined in the other regions does not exactly match the layup in the original, as the optimization tool AESOpt uses a continuous thickness distribution. Because the original length of the plies is implemented, this results in slightly more material in AESOpt. This is the case due to a continuous reduction in thickness after a ply ends instead of a drop in thickness, as it is in reality and in the FEM-model. Next to these factors, the use of two different software programs for the generation of the data might also induce small deviations due to assumptions in the user input and in the software itself.

When analyzing the bending stiffness distributions in Figure 7.1b, higher deviations

can be observed. It can be seen that the bending stiffnesses of the baseline are higher than those of the Original OLW934 blade model. This could be influenced by different factors. Next to differences in the calculations of the softwares, the first difference in the models that could influence the stiffness is again the continuous thickness distribution in AESOpt; a continuous thickness distribution without thickness drops increases the stiffness in those areas, making the full blade stiffer. Additionally, the newly implemented internal structure, as described in subsection 6.1.2, could increase the stiffness. The first change in the internal structure that possibly benefited the stiffness is the use of the core material in the whole trailing edge region by getting rid of the transitional layup. Next, the placement of the shear webs in the spar cap area will increase the flapwise stiffness K_{44} by enabling a more effective shear load transfer between the spar caps. This reduces shear deformation and enhances the overall bending resistance in the flapwise direction. Another structural change that could have increased the torsion stiffness is the change in the layup regions through the thickness. By placing half of the skin layup on the inside of the blade and putting the spar cap and core material in the middle between the two skin layup parts, the load transfer through the thickness is improved, and a more symmetric and balanced layup is found, which increases the torsional stiffness. Indirectly, it also improves the other two bending stiffnesses, because a symmetric and balanced layup reduces stress concentrations, which indirectly influence the resulting stiffness values.

Overall, these findings support and validate the design choices made in the new internal structural layout, indicating that they increase the blade's structural performance. However, it cannot be conclusively stated that these changes alone are responsible, as differences between the two models may also contribute to the observed behaviour.

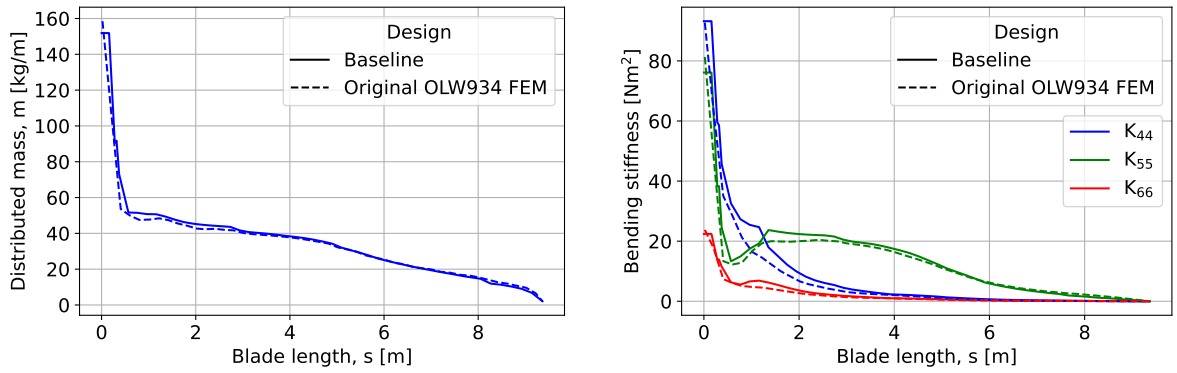

(a) Mass distribution.

(b) Bending stiffness distribution.

Figure 7.1: Comparison of Original OLW934 and baseline design bending stiffness and mass distribution along the blade span.

The strain failure index in the axial direction, which is the main constraint in the following optimization, is checked for the baseline design in the four loading directions. The resulting indices can be seen in Figure 7.2. The most critical loading direction of flapwise downwind loading still has significant improvement potential, as its highest value is only around 0.65. Thus, the baseline design does not fail, and its weight can be reduced in the following optimization.

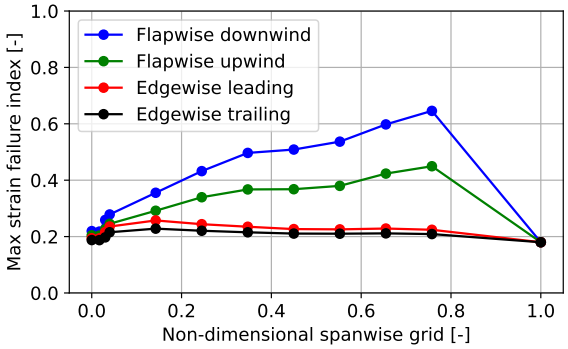

Figure 7.2: The failure indices of the baseline design under flapwise and edgewise loading.

7.2. Optimized designs

As explained in subsection 6.1.2, four designs, having different spar cap widths and shear web spacings, were optimised. The resulting mass and stiffness distributions can be seen in Figure 7.3 and Figure 7.4. In Figure 7.3, it can be seen that the lower the spar cap width is, the lower the mass of the blade. The resulting blade masses can be seen in Table 7.1. A reduction in spar-cap width thus results in an increase in layup thickness; however, this increase is not high enough to surpass the mass of the wider spar-cap designs, which therefore remain heavier. Figure 7.3 shows that a lot of mass was saved in the inner half of the blade; in the outboard region, the achievable reduction decreases, reflecting the smaller amount of material present there initially. When the load difference in the following HAWCStab2 analysis is below 2% different from the original ones and the aeroelastic stability of the design is sufficient, then the design with the smallest spar cap width is used.

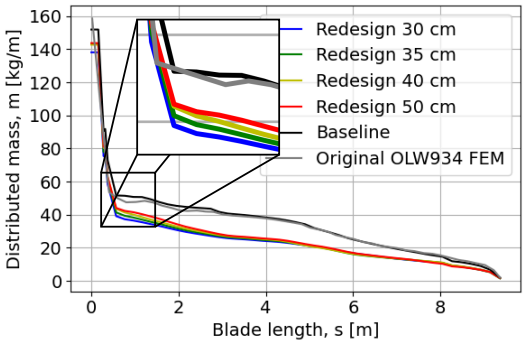

Figure 7.3: Comparison of mass distributions of the new designs and the original and baseline design; Redesigns refer to variations in spar cap width.

Table 7.1: Total mass of optimized designs.

Redesign spar cap width	30 cm	35 cm	40 cm	50 cm
Total mass [kg]	233.46	238.75	243.66	248.45
Reduction from OLW934 [%]	-28.71	-27.10	-25.60	-24.14

Figure 7.4 also shows expected results, that the bending stiffness of the design with the smallest spar cap width is the lowest in flapwise, edgewise, and torsional direction. The stiffness then gradually increases with the width of the spar cap. To result in the lightest design, it generally makes sense to use the optimized design with a spar cap width of 30 cm. It will, however, need to be tested for tower clearance as well as aeroelastic stability due to its low stiffness values.

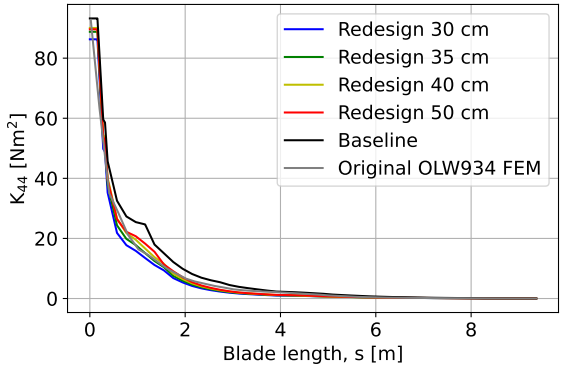

(a) Bending stiffness around x-axis; Redesigns refer to variations in spar cap width.

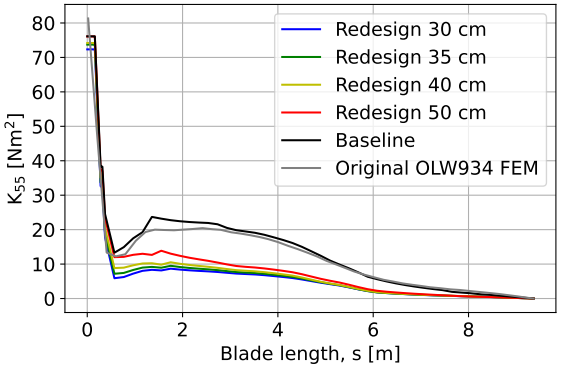

(b) Bending stiffness around y-axis; Redesigns refer to variations in spar cap width.

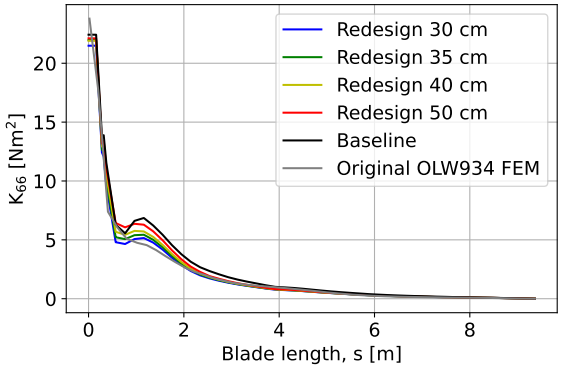

(c) Bending stiffness around z-axis; Redesigns refer to variations in spar cap width.

Figure 7.4: Bending stiffnesses in the HAWCStab2 blade coordinate system for four redesigns in comparison to the original blade and the baseline design.

7.3. Analysis in HAWCStab2

The new designs are tested in HAWCStab2 in the next step. First, the resulting flapwise and edgewise moments are checked to make sure they do not exceed the set load difference tolerance of 2%. If those are sufficient, the aeroelastic stability of the

designs in order of mass reduction is tested. The lowest mass design that also fulfills that requirement is chosen for the following analysis of structural stability in FEM and tower clearance.

7.3.1. Calculated loads and operational data

To verify that the loading, which is the input of the optimization, does not have to be adjusted, the resulting steady-state flapwise and edgewise bending moments are compared to the original ones observed when using the FEM original blade model. Figure 7.5 shows the percentage difference of the baseline design and the four redesigns from the original FEM-model loads over the wind speed range. The maximum value at V=25 m/s is used in the calculations. The highest percent difference at that wind speed is around 0.4% in the edgewise bending moment plot, which is below the set tolerance of 2%. Thus, no recalculation is necessary.

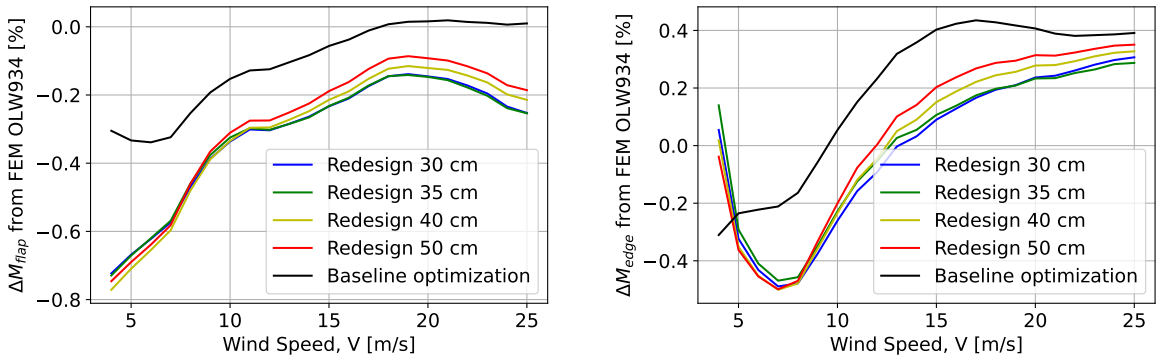

(a) Comparison case: Flap-root-bending moment; Redesigns refer to variations in spar cap width.

(b) Comparison case: Edge-root-bending moment; Redesigns refer to variations in spar cap width.

Figure 7.5: Percentage difference plots to the original FEM-model of root bending moments over the wind speed regime for different redesigns found from AESOpt.

In the flapwise loading plot in Figure 7.5a, it can be seen that all redesigns have lower flapwise loads than the original FEM OLW934 and also as the baseline design. The baseline design has slightly increased loads in comparison to the original blade design over 17.5 m/s. Before that wind speed baseline designs flapwise bending loading is less. When looking at the curves of the redesigns, the same behaviour can be observed as in the edgewise loading, where below a wind speed of 8 m/s, the less stiff designs experience higher loading, and above that mark, the stiffer designs.

When analyzing the trend of the different designs for the edgewise bending moment in Figure 7.5b, it can be seen that all curves follow a similar behaviour over the wind speed regime. Below rated the original blade design experiences higher bending loads than the AESOpt designs. Above rated the AESOpt designs experience higher loads. Additionally, it can be seen that the baseline design generally has a higher load than the four redesigns except for the wind speeds of 3 and 4 m/s. In the behaviour of the four redesign curves, it can be seen that until around 8 m/s, the low stiffness curves have higher loads, and after that, they switch. The curves do not follow this behaviour strictly, as for example at the wind speed of 20 m/s, the design with the

lowest stiffness, the redesign with a spar cap of 30 cm width, and the one with 40 cm width cross, and the lower stiffness design results in a higher load. A general trend is, however, obtainable.

These behaviours can be explained when analysing the tip position plot in Figure 7.6. Figure 7.6 shows the tip position in the y-direction, which is perpendicular to the rotor plane in HAWCStab2. It can be seen that generally, the redesigned curves have higher tip positions than the original design and the baseline design. Only at 3 m/s does the baseline have a higher value than the redesign with a spar cap width of 30, 40, and 50 cm. Additionally, it can be observed that for the redesign curves and for the original design curves, the stiffer designs have higher tip positions at lower wind speeds, but the less stiff designs have higher positions at high wind speeds. The original undeflected, unloaded rotor has a tip position of 2.22 m. This is the value where the described switches occur. For the redesigns, this tip position is reached at around 8 m/s, and for the original designs at 14 m/s.

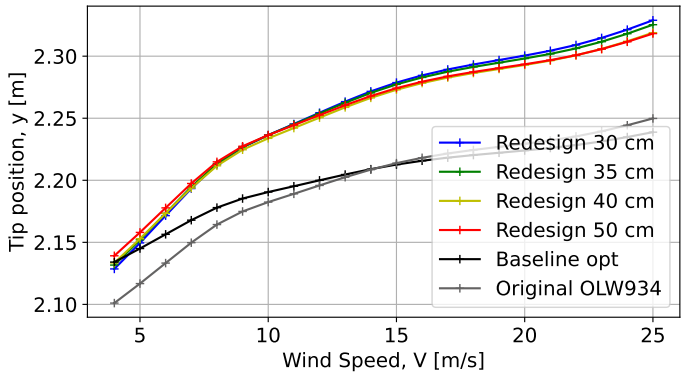

Figure 7.6: Tip position y in the HAWCStab2 rotor coordinate system for four redesigns compared to the original blade and the baseline design; Redesigns refer to variations in spar cap width.

This can be explained by the fact that the blades have a cone angle of 13°, the turbine is a downwind turbine, and it has a fixed rotational speed. In low wind speeds the blades bend against the wind direction. This is the case because in the low wind regime with a fixed rotor speed, centrifugal forces govern the deformation. Due to the centrifugal forces the blades feel, the coning of the blades is reduced, increasing the rotor area and decreasing the tip y-position. The wind has only a small effect in this regime and can not counteract the centrifugal forces that are induced by the relatively high rotor speeds in comparison to wind speeds in this regime. At y=2.22 m, the original coning angle is then reached again due to increased thrust forces induced by higher wind speeds. At this point, the centrifugal and aerodynamic loading counteract each other. With increasing wind speeds after that, the blades deform with the wind direction. Because the centrifugal forces are governed by the mass that is rotating, the heavier blades experience higher forces, resulting in smaller tip positions in the y-direction over the whole wind speed regime and thus also a later return to the original coning angle at V=14 m/s. Lastly, the observation that the stiffer blades have a higher tip position in low wind speeds and a lower tip position at high wind speeds can

also be explained by this. The stiffer blade experiences smaller deflections and thus differs in both loading directions less from the original tip position of y=2.22 m.

Using these observations, the thrust and power difference plots shown in Figure 7.7 can be explained, and following their behaviour, thus also the flapwise and edgewise loading difference plots in Figure 7.5, because the general behaviour of the percent difference for the different designs is the same. This is the case because the flapwise root bending moment is directly proportional to the thrust. The edgewise bending moment is dependent on the aerodynamic moment and thus the power, because $P = \omega \cdot T$ with the rotational speed ω, the torque T, and the weight of the blades. Thus, the percent difference plots are almost identical. The influence of the weight can however be seen when comparing the power plot in Figure 7.5b with the edgewise loading plot in Figure 7.7b. The redesign curves are shifted to lower load values in comparison to the zero line, which represents the original FEM OLW934 model, and to the baseline design, because heavier blades result in higher edgewise bending loads. The general behaviour of the curves is, however, kept. That can be explained for both the edge- and flapwise loading, and the power and thrust curves with the observations found from the y-position plot in Figure 7.6.

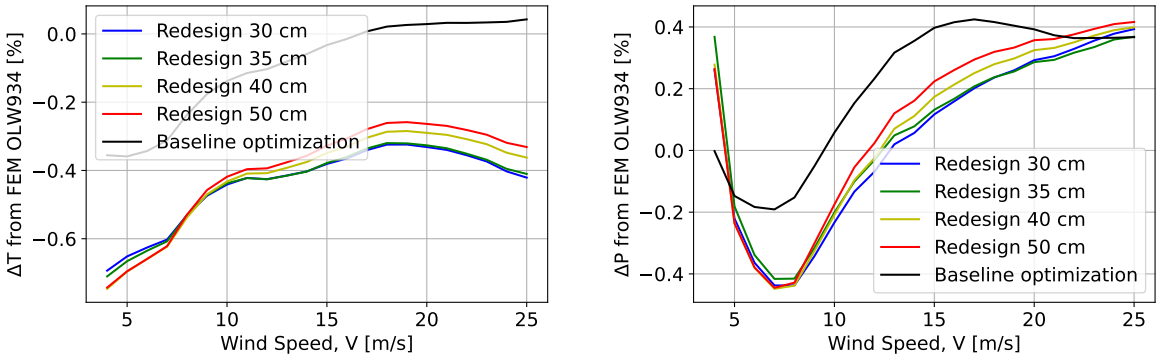

(a) Comparison case: Thrust; Redesigns refer to variations in spar cap width.

(b) Comparison case: Power; Redesigns refer to variations in spar cap width.

Figure 7.7: Percentage difference plots to the original FEM-model of operational data power and thrust over the wind speed regime for different redesigns found from AESOpt.

Generally, the higher the wind speed gets, the lower the rotor area. Also, the designs that experience the lowest tip position in y have the highest thrust, and flapwise root bending moment outputs due to the difference in rotor area described, as can be seen in Figure 7.5a and Figure 7.7a. The power and edgewise bending moment percent difference plots in Figure 7.5b and Figure 7.7b show the same behaviour below rated wind speed at 11 m/s. The highest difference can be found at around 8 m/s where in Figure 4.3 there is the highest power coefficient C_P. This thus shows that the different designs result in different maximum power coefficients depending on how big the rotor area is. The designs with the highest rotor area result in the highest power coefficient and thus the highest power and edgewise moment outputs. Above rated, the behaviour of the power and the edgewise root bending moment is governed by the stall behaviour of the turbine, which influences the power coefficient. Higher power

values can be found for the designs that have a more favourable angle of attack distribution over the blade, resulting in higher power outputs at a wind speed. The angle of attack is dependent on the flapwise bending deflection and possible bend-twist coupling due to it. This is highly dependent on the internal structure defined in the blade, and the stiffness and mass distributions of the different designs.

Overall, it can be seen that in both the flapwise and edgewise root bending moment, the maximum percent difference from the original design is only around 0.5% for the edgewise direction and 0.75% for the flapwise direction, which can be considered negligible. All redesigns can be used in the following design process.

7.3.2. Aeroelastic stability

In the next step, the aeroelastic stability of the designs is checked. Because the redesign with a spar width of 30 cm results in the lowest mass, this one is checked first. If this design is sufficient, it will be chosen for the following design process steps, because it will result in the highest mass reduction at the end of the process.

Figure 7.8 shows the Campbell diagram using the redesigned blade. It can be seen that none of the blade frequencies are close to 1P or 3P, and that the tower frequencies are not close to 3P, 6P, and 9P. As explained in subsection 2.4.2, thus no danger of resonance is occurring. The turbine with the redesigned blade with a spar cap width of 30 cm does not have aeroelastic stability issues and is used in the following steps of the design process.

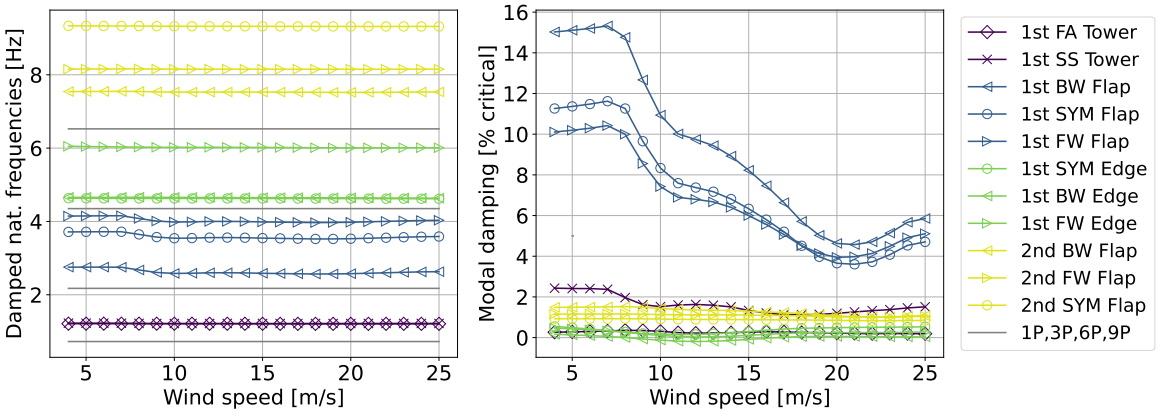

Figure 7.8: Aeroelastic Campbell diagram of redesigend OLW934 blade.

7.4. Internal structure and optimized layup of chosen Design in AESOpt

The redesign chosen is the one with a spar cap width of 30 cm. This design is shown in detail in this section. Figure 7.9 shows the internal structure of the redesign. The spar caps have a width of 0.3 m at the root and reduce to 0.16 m at the tip cut. The width is constant until z=2.43 m and is then gradually reduced. They are placed on the root center point line as described in subsection 6.1.2. The shear webs are placed

at a distance of 0.2 m at the root and have a distance of 0.05 m to the spar cap end to enable secure bonding. At z=8.04 m, they reduce to a distance of 0.11 m to enable fitting the tip shaft. After z=8.04 m, both the spar caps as well as the shear webs are stopped, and the skin layup is continued until the tip. Because the tip break construction is not modeled in this project and no realistic data is available, the tip layup and internal structure were not optimized. To increase stiffness in this area, the cavities in the tip section could be filled with foam. However, this is not within the scope of this report.

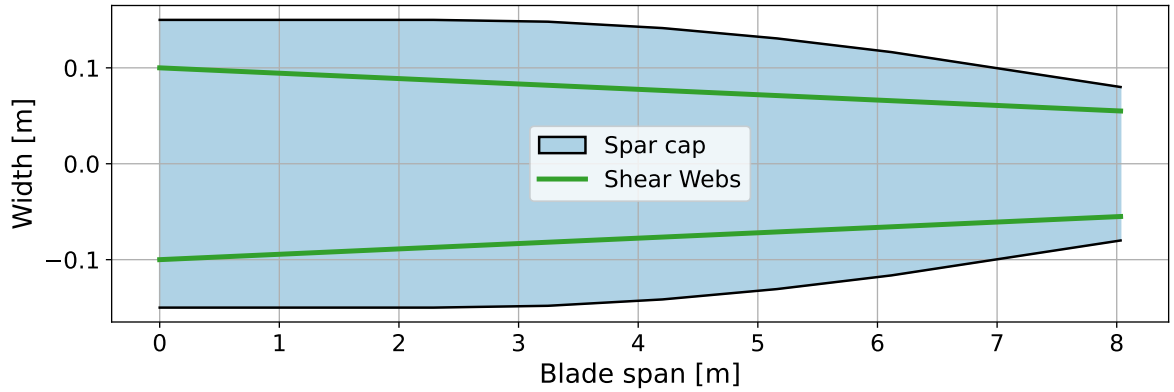

Figure 7.9: Internal structure of redesign.

The baseline layup is optimized except for the insert layup and the shear web layup, which are kept from the original design. The insert is not part of this optimization problem and gets manufactured as an extra part prior. An optimization on the inserts could be part of a subsequent design optimization loop, but is not considered during this report. The layup of the webs is kept to maintain the structural integrity of the blade, because its layup is already minimal. It only consists of two outer layers of Biax on both sides and Core XF in between. This core is only available in this thickness. To reduce the material mass in the webs, a different material would be necessary. The potential material savings on the web are not considered significant enough to study behaviour with different materials. The web layup is therefore kept from the baseline.

The layup was optimized using the layer regions in Figure 6.4. In the optimized design, leading- and trailing-edge reinforcements are deleted, and core material is only introduced between the trailing edge and the spar caps. The placement of three 90° UD plies in the root section is kept the same, with one ply stretching from z=0 m to z=0.4 m, one to z=0.3 m, and one to z=0.2 m. This is done to prevent shrinkage of the cross-section due to resin shrinkage in the curing process. The Biax layer in the skin has a thickness of 1 mm; this was set as a minimum thickness to maintain structural integrity. Additionally, the UD ply with an areal weight of 600 g/m^2 in the skin is only added on the pressure side from 0 to 6.5 m blade span, instead of on the complete skin surface. The placement in the baseline layup can be seen in Figure 6.4. These cuts already reduce the mass. The main mass improvement potential lies, however, in the spar caps and trailing edge filler regions.

Figure 7.10 shows the thicknesses of these four layup regions over the blade span for the baseline and the redesign. The values shown are already real ply thicknesses, the distribution is, however, not fully discretized yet, as in between the section points a continuous distribution is set by AESOpt. In the two spar cap plots in Figure 7.10a and Figure 7.10b, it can be seen that the thickness of the layup is reduced significantly. Especially in the pressure side spar cap is significant optimizaion possible. The pressure side thickness can be reduced more than the one on the suction side over the length of the blade, because the UD strength in tension is higher than the one in compression. Because the downwind loading is higher than the upwind loading, the suction side needs to have more plies than the pressure side. The core material is as can be seen in Figure 7.10c and Figure 7.10d, optimized to have the same thickness variation over the blade span. The core material ply thickness of 1.5 mm is reached at 0.6 m or a normalized value of 0.064. It thus starts when the blades' airfoil changes from a cylindrical cross-section to the next airfoil. The ply is introduced until a blade length of 5.16 m. After that point, AESOpt gradually reduces the thickness to zero. Next to the change in the positioning of the ply is also the thickness reduced from the baseline design, and only 1.5 mm TF core plies will be used instead of 3 mm, like in the original OLW934 blade.

This optimization was done using the axial strain failure index as a constraint, which thus won't be violated. The transverse direction will need to be tested in an FEM-model of the redesigned blade. Before that analysis, the layup will be discretized with engineering judgment to result in a realistic layup.

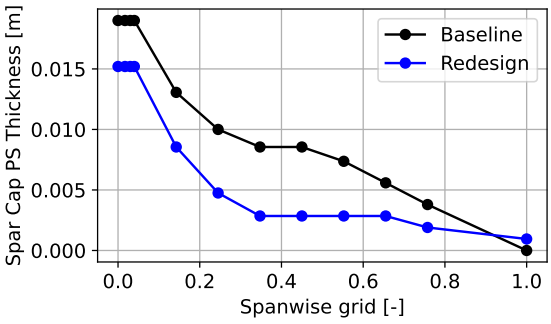

(a) Pressure side spar cap.

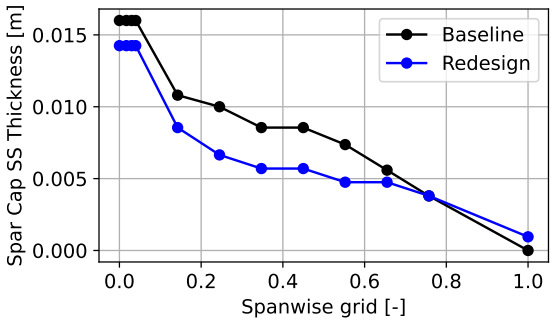

(b) Suction side spar cap.

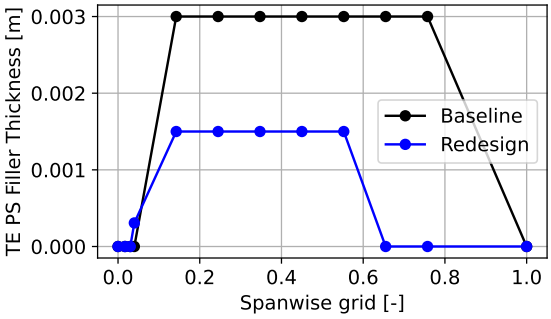

(c) Pressure side trailing edge core.

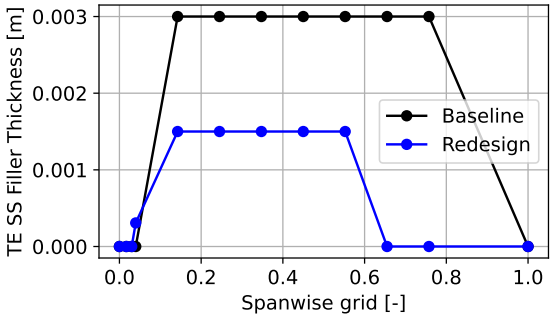

(d) Suction side trailing edge core.

Figure 7.10: Ply thicknesses of baseline and redesign in AESOpt over the blade span.

7.5. FEM-optimization and -validation

In order to validate the blade design in the transverse direction and in buckling a FEM-model is made of the redesigned blade. After discretizing the layup, it is tested in the flapwise downwind and upwind, and in the two edgewise loading directions. The redesigned blade has a mass of 212.48 kg, which is a mass reduction of 35% from the original OLW934 blade. This new design will be validated in the following sections.

Figure 7.11 and Figure 7.12a show a failure in downwind loading conditions and edgewise loading towards the leading edge, which need to be addressed with layup adjustments. Figure 7.11 shows the failure due to flapwise downwind loading. While there is a significant failed region close to the tip, this one can be disregarded, as this is the z-position where the force load is applied. The failure in the suction side spar cap area, however, needs to be addressed, as it is a result of insufficient strength in this region. The problem is solved by continuing one of the UD plies instead of from the blade root to z=5.5 m until the end of the spar cap.

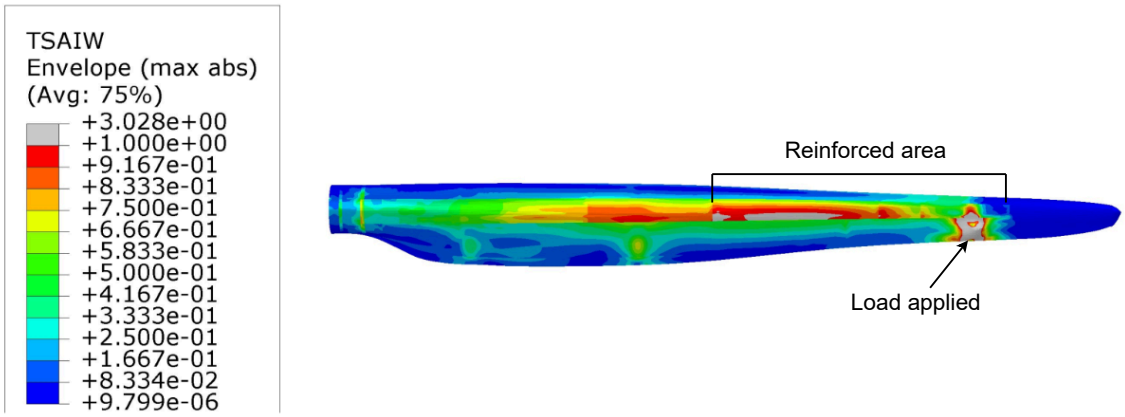

Figure 7.11: Failure under downwind flapwise loading.

The failure in Figure 7.12a due to edgewise loading in the leading edge direction shows significant failure along the circumference between z=0.357 m and z=0.4 m. This is the case due to the use of a 90° UD ply in this area. As a solution, this ply is reduced to only stretch from z=0 to z=0.36 m. The problem arises due to a high change in tensile stiffness in this area, as at z=0.357 m, the extra layers from the root insert end. This induces high tensile stresses. Because UD-material has low strength values in the transverse direction, these stresses induce the failure in the 90° ply. Additionally, a trailing edge reinforcement UD 1200 ply in 0° orientation is used to increase the stiffness in the area. It is applied 10 cm along the trailing edge from z=0 m to z=0.6 m, where the core material ply starts between the trailing edge and the spar cap region, which increases the stiffness. The resulting failure index output is shown in Figure 7.12b, where it can be seen that no failure is apparent anymore.

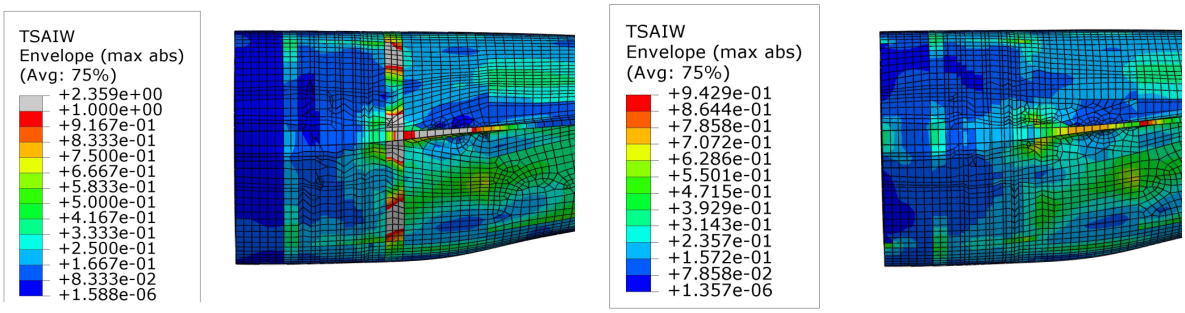

(a) Failure under edgewise.

(b) Tsai-Wu index over the blade after adjustments.

Figure 7.12: Plots under loading towards the leading edge for the blade found from the optimization and after layup adjustments.

After these adjustments, the new layup is tested in the four loading directions, and a mesh convergence study based on deflection is done. The results in the four loading directions for the different mesh sizes between 0.04 and 0.01 m can be seen in Table 7.2. While the deflection in the edgewise loading cases is constant between the four meshes, it can be seen that the tip deflection values for the flapwise loading directions converge. In this study, a mesh size of 0.02 m is used for the modelling, because the maximum deflection difference between this mesh and the 0.01 m mesh is 1 mm in the upwind and downwind loading directions. This is only a percentage difference of 0.08%, which is considered negligible. Thus, the bigger mesh of 0.02 m is used in the redesign. This also validates the use of the same size mesh in the original FEM model in subsection 3.1.3.

Table 7.2: Tip deflection analysis under prescribed loading for different mesh sizes.

Deflection magnitude [m]	Mesh size: 0.04 m	Mesh size: 0.03 m	Mesh size: 0.02 m	Mesh size: 0.01 m
Flapwise downwind	1.304	1.299	1.296	1.295
Flapwise upwind	0.917	0.914	0.912	0.911
Edgewise leading	0.164	0.164	0.164	0.164
Edgewise trailing	0.094	0.094	0.094	0.094

In the original design and redesign, linear S4R elements are used because they result in lower computational time. The drawback of hourglassing control is met by the Abaqus CAE software itself, which provides hourglassing control for linear elements. To verify the use of linear elements, the different loading directions are tested with the same mesh size of 0.02 m and quadratic elements. Table 7.3 shows the tip deflection results. The highest difference can be observed in the flapwise downwind direction with 2 mm, corresponding to a percentage difference of 0.15%. This is also small enough to be considered negligible.

Table 7.3: Tip deflection analysis under prescribed loading for linear and quadratic elements (mesh size: 0.02 m).

Deflection magnitude [m]	Element type: S4R	Element type: S8R
Flapwise downwind	1.296	1.294
Flapwise upwind	0.912	0.911
Edgewise leading	0.164	0.163
Edgewise trailing	0.094	0.094

To investigate the behaviour differences between linear and quadratic elements the Tsai-Wu output of the redesigned blade using quadratic elements is analysed. Figure 7.13 shows the Tsai-Wu output of the fixed blade in edgewise loading towards the trailing edge. It shows the same simulation result as Figure 7.12b, just with quadratic instead of linear elements. It can be seen that there is a failure occurring with quadratic elements. It occurs, however, only at stress concentrations that are artifacts induced by thickness or mass drops. The quadratic elements thus amplify non-realistic artifacts, which correlates to the result in Tsai-Wu with decreasing element size. The drop in thickness induces a stress singularity in those areas, which increases as the element size decreases or the order of the element increases, as the interpolation points in the elements move closer to the ply drop edge. The stress goes to infinity for infinitely small elements. In reality, the ply drops would, however, be made smoother, reducing the stress concentration. Additionally, the stress would be accounted for by microplasticity in these defined thickness drop areas and would most likely not result in the failure of the blade. These areas can not be tested in an FEM-model and have to be tested in a later design iteration using, for example, component testing. In the surrounding area around these high stresses, both Figure 7.13 and Figure 7.13 show similar values. The same behaviour is obtained in the other loading directions. Because the high stress areas are not physical and disregarded, and the remaining stress results are very similar, the use of linear elements for the redesign and also the original blade FEM model is validated.

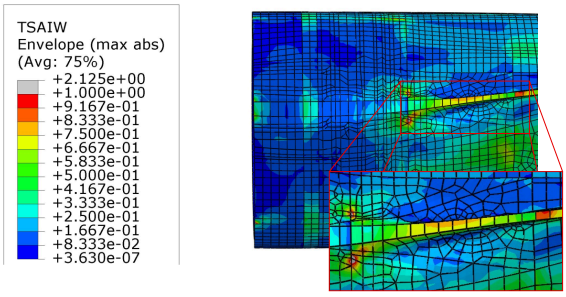

Figure 7.13: Tsai-Wu index under edgewise loading towards the leading edge using quadratic elements.

The resulting Tsai-Wu failure values for the four loading directions of the redesigned, updated blade are shown in Table 7.4. It can be seen that no failure is occurring.

Table 7.4: Tsai-Wu failure index under prescribed loading (mesh size: 0.02 m, S4R elements).

	Tsai-Wu index [-]
Flapwise downwind	0.955
Flapwise upwind	0.913
Edgewise leading	0.8408
Edgewise trailing	0.537

These failure values are obtained after disregarding modeling artifacts, like unrealistic stresses in the load application regions or unrealistic stress results in elements adjacent to thickness drops. The field outputs, including all elements and regions, are shown in Figure 7.14 to Figure 7.17.

The field output for the downwind loading direction in Figure 7.14 shows failure in the load application regions two and four along the blade. These failures can, however, be ignored as these stress concentrations are modelling artifacts. In the rest of the blade, it can be seen that the highest load areas are the suction side spar cap and the pressure side leading edge. Even though the failure index is relatively high, with values between $I_F = 0.9$ and $I_F = 1$, these stress distributions are considered to be acceptable, because both on the materials as well as on the loading high safety factors according to the IEC 61400-1 standard were applied.

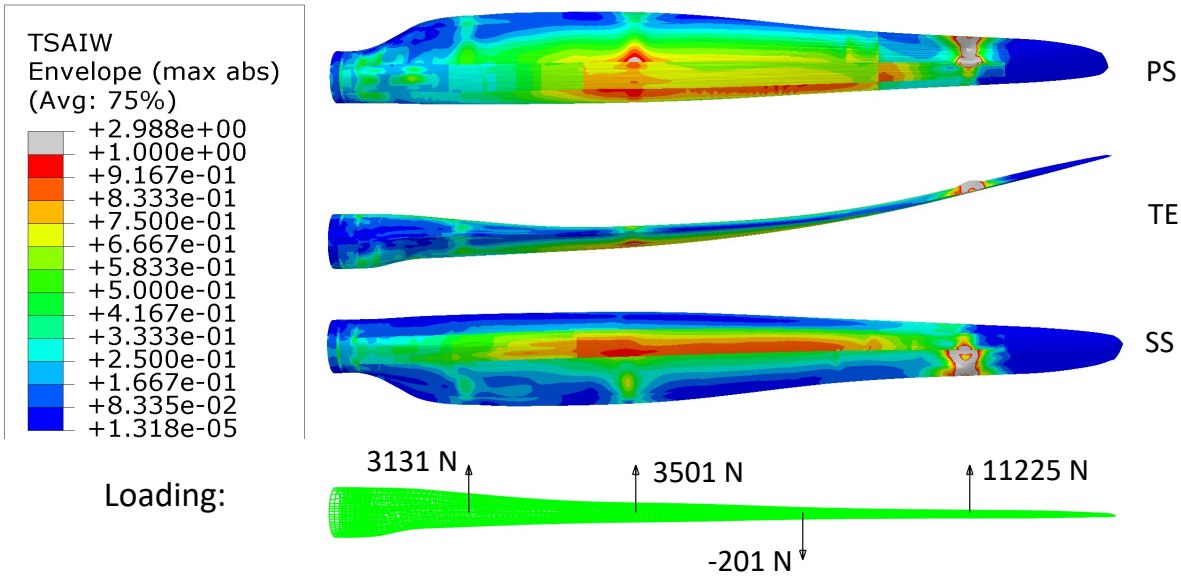

Figure 7.14: Tsai-Wu failure criterion field output under flapwise downwind loading.

Figure 7.15 shows the Tsai-Wu response of the blade to applied upwind loading. In this plot, again, the higher loading areas where the force loads are applied can be neglected. The next highest loaded area is on the pressure side at z=6.5 m. This can be explained by the drop of a UD 1200 ply in the spar cap layup at that z-position and the end of the UD600 reinforcement ply in the skin layup on the pressure side.

Because the failure criterion is not violated, this stress concentration is considered acceptable for this report.

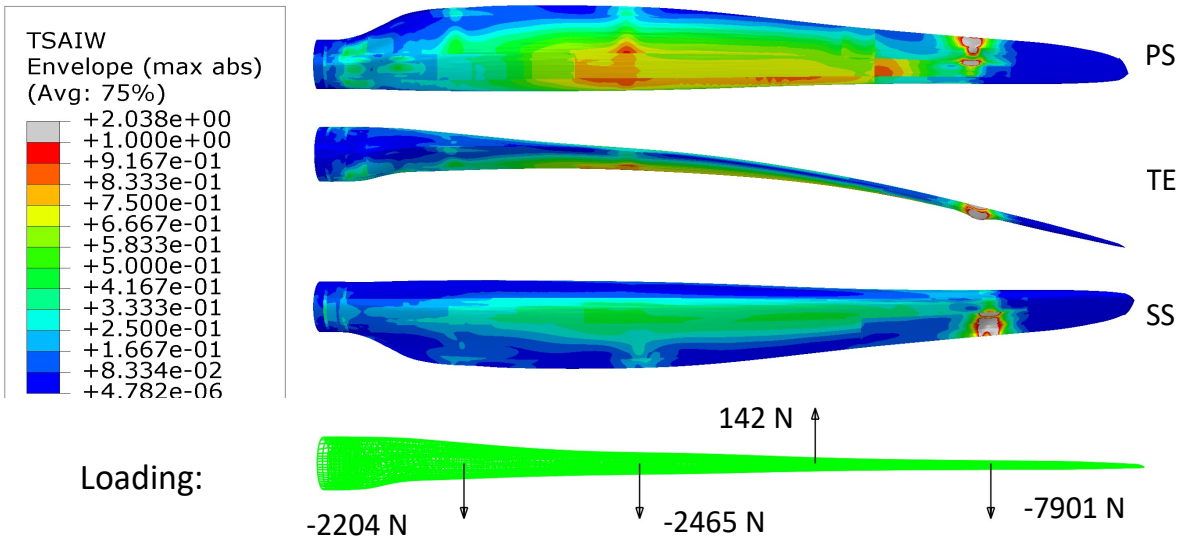

Figure 7.15: Tsai-Wu failure criterion field output under flapwise upwind loading.

Figure 7.16 and Figure 7.17 show the Tsai-Wu failure index field output for the edgewise loading towards the leading and the trailing edge. Both plots show the same highest loaded area, which is the region where the circular cross-section transforms into the trailing edge. In zooms, it can be seen that again, the highest failure criteria values are obtained on the flange surface of the trailing edge. Like in the original Blade FEM-model, these areas are neglected because they do not represent the correct material definition in that region.

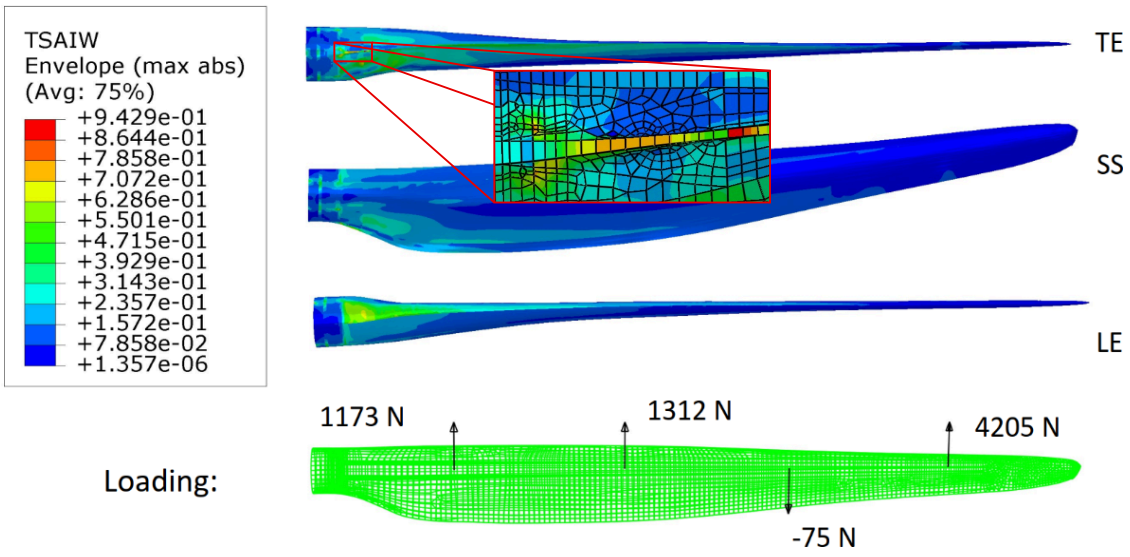

Figure 7.16: Tsai-Wu failure criterion field output under edgwise loading towards the leading edge.

The next highest values are found at z=0.357, where the insert layers drop, and on the

upper and lower surface of the trailing edge flange. Because of significant changes in geometry layup in this region, these stress concentrations are introduced. They do, however, not exceed the failure index value of 1, and this area's structural performance is sufficient.

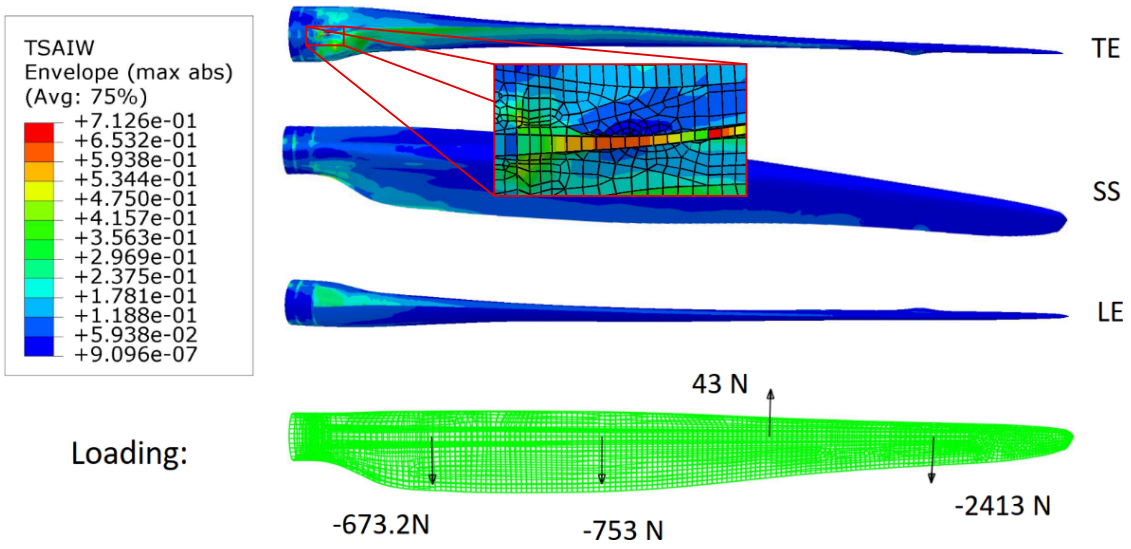

Figure 7.17: Tsai-Wu failure criterion field output under edgwise loading towards the trailing edge.

These failure index outputs validate the design's resistance against buckling and other failures.

7.5.1. Deflection analysis

The next step to validate the design is the deflection analysis. The tip deflections in FEM are found and reported in Table 7.5. Additionally, the corresponding y-deflection in the HAWCStab2 rotor coordinate system is calculated using Equation 4.2. Using Equation 4.1, the tower clearance can be calculated. It can be seen that the tower clearance is in all load cases larger than the minimal tower clearance of 0.94 m calculated in subsection 4.3.2 and thus sufficient.

Table 7.5: Deflection under prescribed loading.

Deflection [m]	Magnitude	U1	U2	U3	y-deflection HAWCStab2	tower clearance
Flap downwind	1.295	0.071	1.293	0.011	1.258	4.140
Flap upwind	0.911	-0.050	-0.910	-0.007	-0.885	1.997
Edge trailing	0.094	-0.093	-0.015	0	-0.016	2.866
Edge leading	0.164	0.162	0.027	0	0.026	2.908

7.6. HAWCStab2 Analysis of final design

The last step to fully validate the redesigned blade is checking its aeroelastic stability and loads. This is done in this section as well as comparing the redesigned blade

mass and stiffness to the found redesign in AESOpt with a spar cap width of 30 cm, the baseline AESOpt blade, and the original FEM blade model. HAWCStab2 is used for that. The final redesigned blade is imported into HAWCStab2 using the steps explained in section 6.6.

7.6.1. Mass and Stiffness comparison

The mass and bending stiffnesses of the two redesigned models and the two original blade models are compared. For both the redesign and the original, the FEM version is compared to the AESOpt version.

Figure 7.18 shows the mass distribution for the four blade models after transferring them into HAWCStab2. It can be seen that the mass distribution from the models made in FEM fits closely with the ones coming from AESOpt. When analyzing the final design curve, it can, however, be seen that after the initial root part ends, the model in FEM drops to a lower mass value than the one in AESOpt. This can be explained by the discretization of the layup. This part is where the biggest change in the spar cap thickness happens. Thus, here is also the highest deviation expected, when the thickness distribution is discretized. The last section at 9.34 m also deviates slightly, as in the setup of the FEM input file, the parameters of the second-to-last section are also applied to the blade tip. The rest of the blade mass deviates only minimally from the mass distribution in AESOpt.

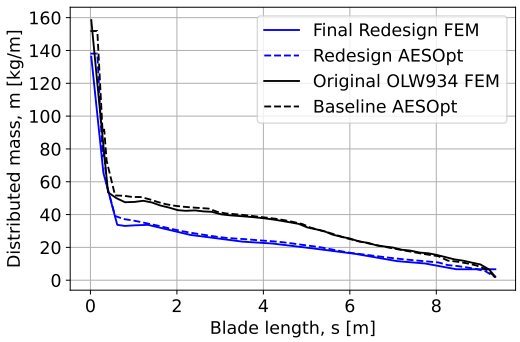

Figure 7.18: Comparison of mass distributions of the new designs and the original and baseline design; Redesigns refer to variations in spar cap width.

Table 7.6 shows the total masses between the 4 models, as well as the mass calculated in FEM, and their percentage difference to the original OLW934 blades made in reality.

First, comparing the original blade masses, it can be seen that, as intended, all are very close to the blades made in reality. The three design masses also do not deviate significantly in comparison to each other, which verifies the validity of the models. The total mass of the redesigned blade in AESOpt is 233.46 kg, 28.71 % lower than the original, showing a significant weight reduction and blade improvement. The mass reduction is with about 35 % even bigger in the FEM model as can be seen in Table 7.6. This is the case due to layup discretization and reduced adhesive mass. The goal of

reducing the blade mass by 75 kg is thus exceeded with the new design.

Table 7.6: Total masses of the original blade models and the redesigned ones in FEM and HAWCStab2.

	Mass [kg]	Difference from reality OLW934 [%]
FEM Original	321.42	-1.85
Import from FEM Original into HAWCStab2	316.56	-3.34
Baseline AESOpt	330.62	0.95
Redesign AESOpt	233.46	-28.71
FEM Redesign	212.48	-35.12
Import from FEM Redesign into HAWCStab2	214.28	-34.60

When analyzing the bending stiffnesses in Figure 7.19, however, higher deviations can be observed. While the edgewise bending stiffness between the two models matches closely, they deviate in K_{44} and K_{66} in the transition area between the root and the rest of the blade. The differences are again a result of the discretization process. In general, it can be seen that the two calculation methods roughly result in the same values, validating the chosen approach.

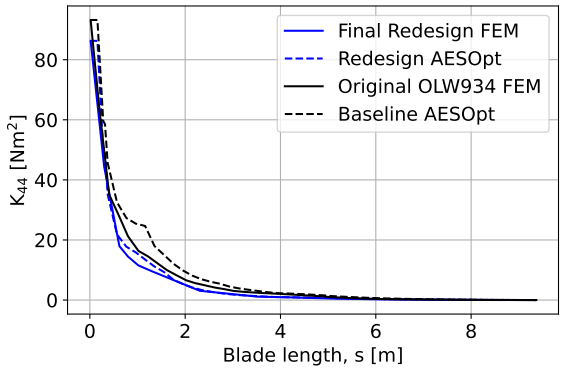

(a) Bending stiffness around x-axis; Redesigns refer to variations in spar cap width.

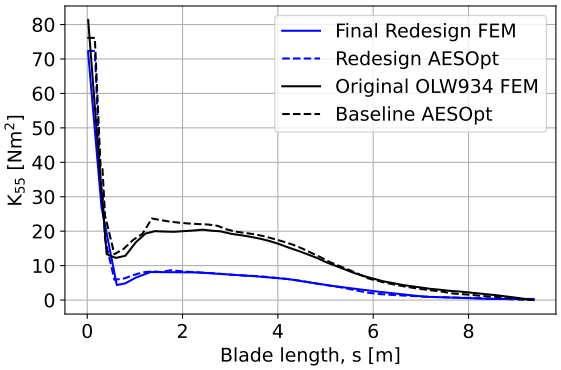

(b) Bending stiffness around y-axis; Redesigns refer to variations in spar cap width.

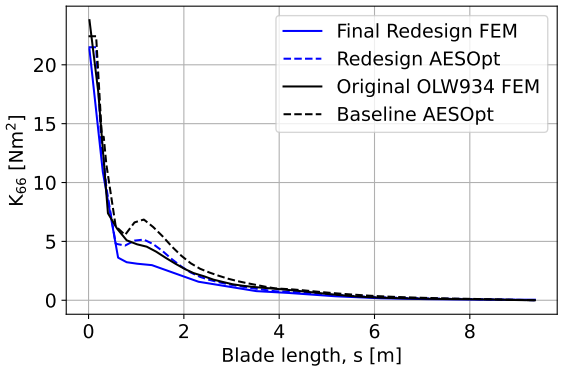

(c) Bending stiffness around z-axis; Redesigns refer to variations in spar cap width.

Figure 7.19: Bending stiffnesses in the HAWCStab2 blade coordinate system for four redesigns in comparison to the original blade and the baseline design.

7.6.2. Calculated loads and operational data

To check whether the applied DLC 1.3 loads are valid, the new steady state loads and operational data are again checked for the new design. Figure 7.20 shows the percent differences compared to the original loads calculated using the FEM imported original blade. It shows the AESOpt baseline blade, the redesign AESOpt blade, and the final redesign FEM blade.

In the flapwise plot in Figure 7.20a, it can be seen that the final redesign FEM blade follows the general trend of the other curves. It is, however, more consistent at a value of between 0.4 and 0.1%. The flapwise moment of the final redesign imported from FEM is higher than the Redesign AESOpt, which reflects the chosen design with a spar cap width of 30 cm. After a wind speed of 19 m/s, the flapwise moment of the AESOpt design is, however, higher. The discretization and layup adjustments in the FEM setup thus changed the flapwise and edgewise bending moments. An influence can also be observed when analyzing the edgewise loading percent difference plot in Figure 7.20b. While below 8 m/s the two curves of the redesign in AESOpt are close, above that wind speed their edgewise root bending moment differs significantly. While the curve of the final redesign FEM-model is lower than the AESOpt model until $V = 21$ m/s, with higher wind speeds, the FEM-model imported curve of the final redesign surpasses the AESOpt-model redesign curve, and at 23 m/s, also the curve of the AESOpt Baseline is surpassed.

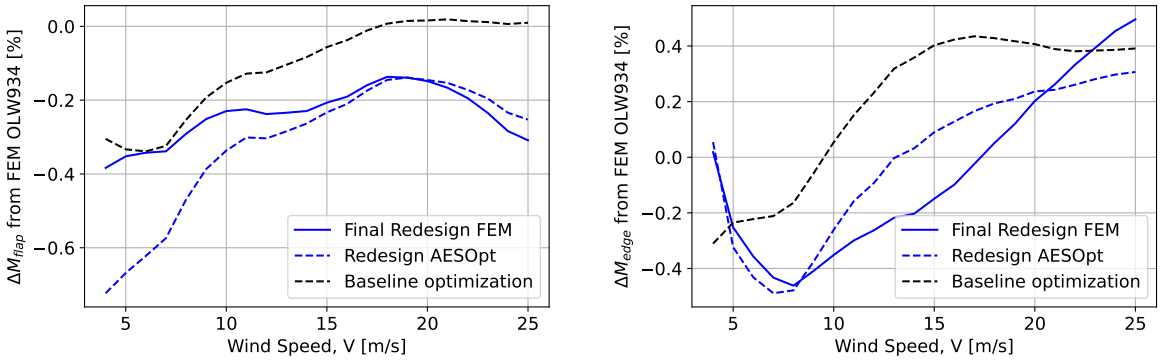

(a) Comparison case: Flap-root-bending-moment; Redesigns refer to variations in spar cap width.

(b) Comparison case: Flap-root-bending-moment; Redesigns refer to variations in spar cap width.

Figure 7.20: Percentage difference plots to the original FEM-model of root bending moments over the wind speed regime for the AESOpt baseline and redesign, and the Final redesign.

These behaviours can again be explained when analyzing the tip y-position plot in Figure 7.21. It can be seen that the rotor with the final redesign FEM blade has the highest tip deflection over the wind speed regime, except for the wind speed of 4 m/s, where it is slightly below the Baseline design imported from AESOpt. This can be explained by the earlier observation that it has the lowest mass and the lowest stiffness. While the low stiffness causes the blade to bend against the wind speed due to its centrifugal force until a wind speed of 7.5 m/s, it does not bend as far as the AESOpt Redesign curve. This is the case because the deflection in this wind regime is mainly governed by the lower mass, causing lower centrifugal loads. Overall, it can

be seen that the slope of the tip position over the wind speed is higher for this design, because its stiffness is lower, resulting in higher deflections in the wind speed regime above 7.5 m/s.

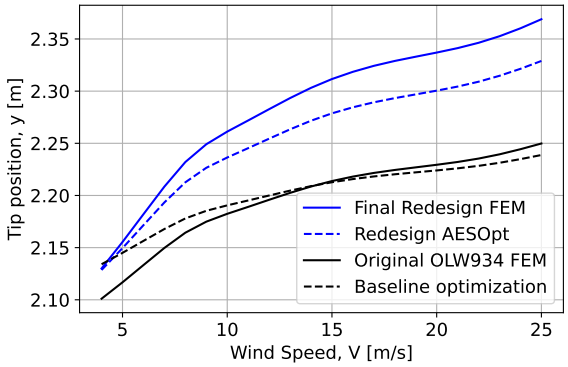

Figure 7.21: y-position in HAWCStab2 hub coordinate system.

These observations can be used to explain the behaviour of the root bending moments in Figure 7.20. The flapwise bending moment starts at higher values than the Redesign AESOpt; this can be explained by the lower stiffness of the blade in all bending directions. The blade probably experiences a different amount of bend-twist coupling than the AESOpt blade. The same can be seen when analyzing the baseline curve in comparison to the original FEM model, which is in these plots defined as the zero line. While their difference as described in section 7.3 is likely caused by their different deflections, a different bend-twist coupling could also be apparent. Thus, the blades imported from FEM seem to have more bend-twist coupling. When the blades deflect against the wind, the bend twist coupling results in a higher angle of attack and thus power, thrust, and root bending moment.

After 7.5 m/s, it can be seen that the AESOpt redesign curve starts to increase significantly in flapwise root bending moment. The FEM redesign curve stays more constant in comparison to the original FEM-model design, because it experiences higher deflections in the downwind direction at the same wind speeds, resulting in less rotor area and thus lower thrust loads. Additionally, the bend-twist coupling working in the opposite direction likely limits the thrust output and thus the flapwise moment.

When analysing the edgewise root bending moment, the corresponding behaviour can be seen below the rated wind speed, with higher power due to the bend-twist coupling. Already at a wind speed of around 8 m/s the curves cross; however, due to stall starting around the V_{rated} wind speed. The stall behaviour of the different blades is, as explained before, very dependent on the local angle of attack along the blade span, resulting in different stall behaviour depending on the bend-twist coupling of the blade and the deflection and resulting rotor area. A detailed analysis of the stall regime lies beyond the scope of this report. Overall, it can, however, be seen that the redesigned blade imported from FEM also results in a percentage difference of less than 2% from the original design, validating the loads applied on the FEM-model.

Figure 7.22 shows the corresponding thrust and power plots, which follow the behaviour, as explained, of the root bending moments in the flapwise and edgewise direction, and also only result in a maximum percentage difference of 0.6 for the redesign imported from FEM in the difference in power. It again shows that the power difference below rated is less than the edgewise bending moment difference, because the edgewise bending moment is amplified by the blade mass, which differs significantly between the two FEM designs.

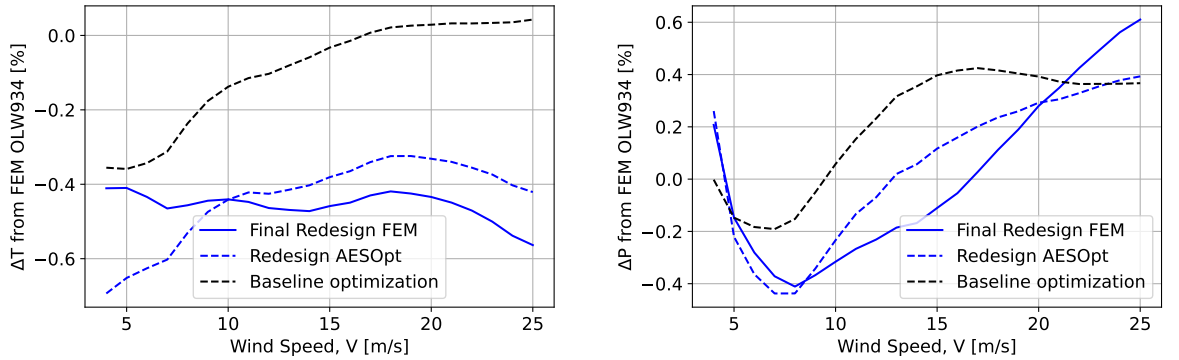

(a) Comparison case: Flap-root-bending-moment; Redesigns refer to variations in spar cap width.

(b) Comparison case: Flap-root-bending-moment; Redesigns refer to variations in spar cap width.

Figure 7.22: Percentage difference plots to the original FEM-model of the thrust and power output over the wind speed regime for the AESOpt baseline and redesign, and the Final redesign.

7.6.3. Blade eigenfrequencies of Redesign

Next, the eigenfrequencies in HAWCStab2 and the FEM model for the redesign are compared for verification of the data transfer between the two software. Table 7.7 shows the eigenfrequency results for the HAWCStab2 and FEM model and their percent difference. It can be seen that there is a significant mismatch between the two models. Two causes are investigated during this report.

Table 7.7: Blade-only eigenfrequencies computed with HAWCStab2 using a transfer with averaged mass distribution and a mesh size of 0.06 m.

Mode	Mode name	HAWCStab2 [Hz]	Redesign FEM	
			f [Hz]	Diff [%]
1	1st flap	3.25	2.78	15.59
2	1st edge	5.56	4.36	24.19
3	2nd flap	9.83	10.55	7.07
4	3rd flap	19.59	18.83	3.96
5	Combination flap & edge	22.16	20.51	7.74
6	1st torsion	34.53	20.91	49.12

The first possible cause is a too coarse mesh in FEM and BECAS, influencing the correct transfer of structural properties between the two models. Table 7.8 shows the blade-only eigenfrequencies using a mesh size of 0.02 m. It can be seen that the percent difference values are very close to the ones in the coarser mesh. Additionally, Table 7.8 shows the eigenfrequencies in FEM, if the same averaged mass distribution of the extra masses is applied as used in the transfer between the two models. It can be seen that the difference between those frequencies and the ones found in HAWCStab2 is significantly smaller, and the percent differences are reduced. This mass distribution does, however, not reflect reality. The assumption of using an averaged mass distribution is thus not very exact for the redesigned blade model in HAWCStab2, and in the next iteration loop, the mass distribution should be applied realistically when transferring between the models to be able to verify the aeroelastic stability results of the turbine.

Table 7.8: Blade-only eigenfrequencies computed with HAWCStab2 using a transfer with averaged mass distribution and a mesh size of 0.02 m.

Mode	Mode name	HAWCStab2 [Hz]	Redesign FEM		Avg. mass FEM	
			f [Hz]	Diff [%]	f [Hz]	Diff [%]
1	1st flap	3.21	2.79	14	3.30	2.76
2	1st edge	5.46	4.37	22.17	4.86	11.63
3	2nd flap	9.70	10.59	8.77	9.85	1.53
4	3rd flap	19.46	18.75	3.72	17.60	10.03
5	Combination flap & edge	21.95	20.48	6.93	20.26	8.01
6	1st torsion	34.28	20.57	49.99	22.65	40.86

In the future, the influence of the tip stiffness should also be investigated, as this would also alter the blade eigenfrequencies and thus the aerolastic stability of the turbine. During the report, the extra stiffness included by the tip break is not included; the mass is, however, in the FEM model applied to the tip region of the blade. This is most likely the main reason for the mismatch between the two models, as the mass in the HAWCStab2 model is low in the tip region. A high mass in the tip, without the corresponding stiffness, is, however, also not realistic, making it necessary to do a closer investigation into this area to be able to calculate the correct eigenfrequencies of the blades. In the original blade design in subsection 3.1.1, extra shear webs were used in the tip area to mimic the stiffness of the tip. This could also be one measure in the redesign to better resemble the stiffness in reality. This could also be the reason why less deviance between the eigenfrequencies was observed in the original blade case, because the stiffness and mass in the tip region in the FEM-model were more balanced. Using the averaged mass distribution during this report is thus considered to be in better agreement with the eigenfrequencies in reality than applying the tip break mass in the tip region without adding its stiffness. In future design loops, both factors should, however, be adjusted to best resemble the blade in reality.

7.6.4. Aeroelastic stability

The study on how the tip stiffness changes the blade-only eigenvalues will also change the aeroelastic stability analysis of the turbine. The Campbell diagram using the current HAWCStab2 model can be seen in Figure 7.23. No violation between the blade frequencies and the 1P and 3P and of the tower frequencies and the 3P, 6P, and 9P frequencies is apparent.

When including the findings from the blade-only eigenvalue analysis, there could be a problematic interaction between the first flapwise backwards whirling mode and the 3P frequency, as they are close together. A decrease in the first flapwise eigenfrequency of the blade dor example when implementing the correct mass and stiffness distributions could result in a decrease in the first flapwise backwards whirling frequency, resulting in resonance problems. Table 7.7 and Table 7.8 show that the first flapwise eigenvalues are significantly smaller using the correct mass distribution. On the other hand, however, no stiffness from the tip break is included in the model, which would increase the frequency again. Thus, it is necessary to specifically model the tip region more exactly to be able to verify the aeroelastic stability of the turbine. Using engineering judgement, however, no instability is expected, because this mode is highly damped, as can be seen in Figure 7.23. Additionally, because the stiffness of the tip is underrepresented in the current setup, most likely the first backwards whirling flap frequency will not fall significantly when considering the correct mass and stiffness distribution, and an exact coincidence of the two frequencies is generally not probable. To ensure this, however, an extra design iteration is necessary. When an exact coincidence is occurring, it is based on the wind turbines' fixed speed characteristic, easy to solve the resonance problem by either adding stiffness to the blade using reinforcements or lump masses to offset the turbines' first backwards whirling mode, as it is relatively constant over the wind speed regime.

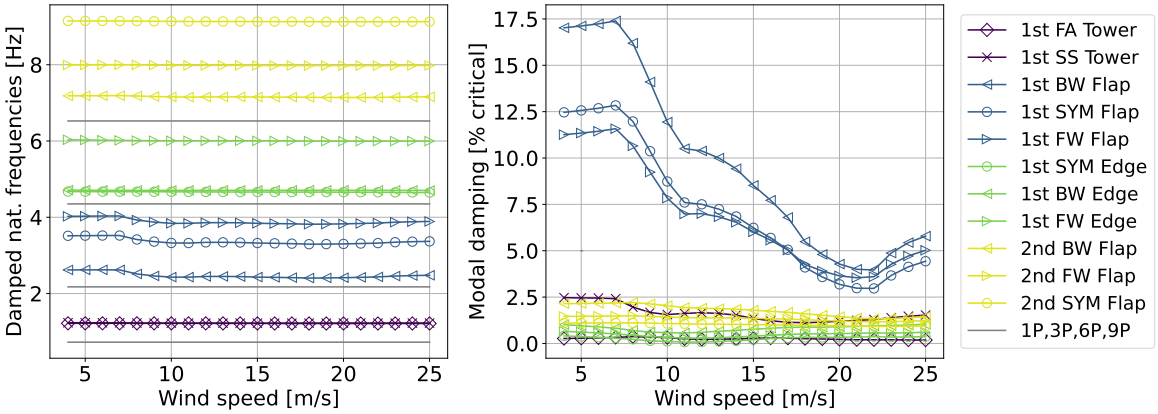

Figure 7.23: Aeroelastic Campbell diagram of the final redesigned OLW934 blade with averaged mass distribution.

8

Discussion

A framework was successfully applied to improve the OLW934 rotor blade and reduce its overall weight. The target mass reduction of 75 kg was exceeded while still maintaining structural and aeroelastic integrity. This makes the blade suitable for use by NorZet Ltd on the E-3120 turbine. The blade was successfully improved by using engineering judgment and a gradient-based approach to optimize the internal structure, the materials, and the layup. The structural and aeroelastic constraints of no failure under ultimate loading, sufficient tower clearance, and aeroelastic stability were employed to ensure the integrity of the blade. This is how a blade's weight can be reduced while keeping the structure's integrity, answering the main research question of this work.

8.1. Answers to research questions

The sub-research questions investigated in the second part of the project are answered in this section, demonstrating the main findings during the redesign process.

What are the most significant weight drivers in the design?
The main weight drivers in the original blade design were the internal box girder structure, the lay-up strategy employed, and the use of relatively thick laminates. By switching to a shear web design, stiffness was increased and mass reduced, without optimizing the lay-up. Next to a reduction in necessary adhesive, the switch enabled the more strategic placement of the webs inside the spar cap region, enabling better shear load transfer. Additionally, this measure gave the opportunity to remove the weight inefficient transitional layup between the sandwich core structure in the trailing edge region and the spar cap. Instead, the spar cap directly connects to the trailing edge sandwich structure, increasing the stability of the blade. Additionally, the definition of the layup regions through the thickness was redone by placing a skin with biax plies on the inside and outside of the blade to better manage transverse loads. The core sandwich material is no longer used in the entire skin but only in the trailing edge region, enabling significant weight reduction. The largest weight reduction was achieved in the first half of the blade, where more material is apparent. The outer half required more structural integrity to preserve aerodynamic surface stability, limiting potential reductions there.

What can be done to mitigate the weight drivers?
Changing the internal structure from a box girder to shear webs significantly improved stiffness and lowered the mass. It also reduced the number of lay-up transitions, lowering the risk of stress concentrations. When this new structure was combined with a strategic optimization using the gradient-based optimization software AESOpt, more efficient material usage was achieved, resulting in a total mass reduction of 35%. This demonstrates that redesigning both internal structure and lay-up together has great weight reduction potential, resulting in better-performing rotor blades.

During this report, a simpler version of the AESOpt optimization was used, excluding the aerodynamic optimization and also excluding aeroelastic checks from the optimization scheme. These validation checks were done manually after the resulting design. Because in this project only the internal structure was changed, this procedure was sufficient and reduced convergence issues as well as computational time. During the optimization, thus, only the structural constraint of no axial failure being allowed was used. With that, a significant weight reduction was achieved by optimizing the thickness of the play layers. Design variables on the spar cap and shear web spacing and positioning were also found to be easier to use in the setup of the input than in the optimization scheme itself, to again reduce computational time and result in a sufficiently designed blade during the time period set in this project. It was, however, noted that including these in the optimization scheme in future iteration loops could likely result in an even higher weight reduction.

What are the effects of the redesign on the aeroelastic behaviour and the stability of the rotor blade and turbine?
Reducing blade mass affects aeroelastic stability and must be balanced by maintaining sufficient stiffness. If the blade's eigenfrequency aligns with an excitation frequency, stiffness must be adjusted to avoid resonance. Because a fixed speed stall turbine is analyzed, the eigenfrequencies only change slightly with wind speeds; thus, the eigenfrequency placement is straightforward to simply avoid exactly coinciding eigen and excitation frequencies. In this report, no definitive answer can be made as to whether the aeroelastic stability is sufficient, because the stiffness and structure of the tip, containing the blade tip break, are not known, and an averaged mass distribution has been shown to be an insufficient assumption to reflect reality. Differences in the mass and stiffness distributions of the blade influence the blade's eigenfrequencies. Engineering judgment is used to give a suggestion. Most likely, the blade is stable as the eigenfrequency in danger, the first flapwise backwards whirling frequency, is heavily damped, and the introduction of stiffness from the tip break construction will increase this mode's frequency, counteracting possible reduction in the frequency due to changes in the mass distribution, endangering resonance due to proximity to the 3P excitation frequency. An additional design iteration is, however, necessary to verify this.

In this redesign, aeroelastic loads remained largely unchanged. A heavier blade typically results in higher edgewise loading, so reducing weight is beneficial. Additionally, since the turbine uses coned blades, reduced stiffness can cause more deflection,

slightly decreasing the rotor area and load in the flapwise and edgewise direction. Also, other effects have likely affected the blades' load output, like bend-twist coupling and different distributions of angle of attack, resulting in different stall behaviour. Overall, the change in loads was, however, found to be significantly below the set tolerance of 2%, and a reiteration with updated loads was thus not considered necessary. The structural stability of the final blade design under the ultimate loads was found to be sufficient after minor layup adjustments on the blade, resulting from the optimization in AESOpt.

8.2. Potential error sources

During the redesign process, all errors described in section 5.2 found for the setup of the original blade are also possible in the HAWCStab2 and FEM setup of the redesigned model. Some additional potential sources of error are, however, also apparent.

In AESOpt, four different internal structure designs are defined, which vary based on the width of the spar cap. Apart from that, no other changes in the spar cap and shear web design and placement were tried. It is, thus, very likely that the resulting internal structure is not the most optimized version. Additionally, a layup region definition was made as an input, impossible to change by the optimizer. Next, a specific number of cross sections is defined for which the optimizer optimizes the thicknesses. Thus, interpolation error between those will not result in the most optimized redesign. Additionally, an error is introduced by setting a specific optimization success criterion, where the weight of the previous iteration is compared to the current one. Lastly, when discretizing the resulting layup with engineering understanding, the resulting design is very likely to deviate from the most optimized one. When checking the aeroelastic behaviour of the new design, it was found that the steady-state loads of the redesigned blades deviate only minimally, and the difference was thus neglected, inducing a small error. Also, only the steady state values are compared and not the turbulent load cases. When checking the resulting blade in HAWCStab2 and FEM in the following steps, the same error sources discussed for the original design are apparent. Also, again, intrinsic assumptions in the windIO to HAWC2 converter and the AESOpt framework could induce minimal errors.

Despite the identified potential sources of error, the applied framework has proven to be effective. A significant blade mass reduction was achieved without compromising structural or aeroelastic integrity. While some assumptions and simplifications require further validation, they do not diminish the relevance or reliability of the overall findings. This work demonstrates that substantial weight savings are achievable and provides a solid foundation for future iterations of the OLW934 blade optimization.

8.3. Recommendations for future work

The next steps to be taken are conducting a comprehensive validation of the resulting aeroelastic behaviour, including the influence of the tip stiffness and a more exact mass distribution. Also, as for the model of the original blade, the structural validity

of the areas disregarded due to modelling artifacts during the FEM analysis should be investigated more closely, and their structural integrity should be validated using, for example, component tests. Additionally, other initial internal structure designs as well as layup region definitions should be checked to see if there is an even higher-performing design. The resulting design should also be checked by running turbulent load cases, including lifetime assessment using fatigue analysis. When the chosen redesign is found for the OLW934 blade and its aeroelastic and structural stability is found to be sufficient, certification tests will be the next step before the first prototype can be manufactured and tested, resulting eventually in series production and the use of the blade on the NorZet rotor retrofit of the E-3120 turbine.

Generally, the adjustments made to the framework can be used in future work to optimize different blades and get reasonable first redesigns. These can then be refined in the following design iterations. The framework can also be extended to include the aeroelastic behaviour directly in the optimization itself, resulting in a higher automation level of the process.

9 Conclusion

This report investigates how the weight of a wind turbine rotor blade can be reduced while maintaining the structure's integrity. This is done based on the OLW934 wind turbine blade from Olsen Wings A/S. A framework is used to reduce the blade weight of around 327 kg by optimizing the blade structurally with a gradient-based method. Additionally, constraints on the structural and aeroelastic stability, as well as the tower clearance, are employed to ensure sufficient structural integrity. After the redesign process, the resulting blade's mass is reduced by 35% from the original one, resulting in a final blade reduction of around 114 kg from reality and thus exceeding the target of 75 kg. The results of the checked constraints, including structural stability, aeroelastic stability, and tower clearance, show that they are fulfilled. Extra verification on the aeroelastic stability is, however, needed in the next iteration of the design.

This result is generated by simulating the original blade and turbine first structurally and aeroelastically using Finite Element Methods and the Aeroelastic code HAWCStab2. Also, input data from an existing aeroelastic model of the original blade in Flex 4, made by NorZet Ltd, was used. The original blade is then structurally optimized using the gradient-based method AESOpt. The resulting design is checked for validity in FEM and HAWCStab2 again. This concludes the optimization process, resulting in the significant mass reduction of 35%.

Several key discoveries were found during the optimization process. Adopting a shear web design proved to be more efficient in terms of blade mass than a box girder, allowing for greater mass reduction. Structural optimization alone, without altering the airfoil shapes, was sufficient to achieve significant reductions in overall blade mass, where most savings were generated in the inner part of the blade. A smaller spar cap width also contributed to higher mass reduction, even with thicker spar cap laminates. Since the shear webs are placed within the spar cap region, both the spar cap width and the resulting shear web placement are important factors in the optimization. These findings highlight the effectiveness of the applied optimization process using the gradient-based optimization framework AESOpt in improving the blade's structural efficiency.

References

[1] J. Zhu, X. Cai, D. Ma, J. Zhang, and X. Ni, “Improved structural design of wind turbine blade based on topology and size optimization,” *International Journal of Low-Carbon Technologies*, vol. 17, pp. 69–79, 2022, ISSN: 17481325. DOI: 10.1093/ijlct/ctab087.

[2] M. F. Jensen and K. Branner, “Introduction to wind turbine blade design,” in *Advances in Wind Turbine Blade Design and Materials*, Elsevier Inc., 2013, pp. 3–28, ISBN: 9780857094261. DOI: 10.1533/9780857097286.1.3.

[3] K. Wood, *Wind turbine blades: Glass vs. carbon fiber*, Accessed: 04 Feb 2025, 2012. [Online]. Available: https://s3-video.definedstem.com/WebsitePDFs/0b2e0f3b-fdd4-4dd6-b1f2-7ba1e3a09186.pdf.

[4] K. Hayat, S. Siddique, T. Sultan, H. T. Ali, F. A. Aloufi, and R. F. Halawani, “Effect of Spar Design Optimization on the Mass and Cost of a Large-Scale Composite Wind Turbine Blade,” *Energies*, vol. 15, no. 15, Aug. 2022, ISSN: 19961073. DOI: 10.3390/en15155612.

[5] A. More and A. Roy, “Design and Weight Minimization of Small Wind Turbine Blade for Operation in Low-Wind Areas,” in 2020, pp. 311–322. DOI: 10.1007/978-981-15-2662-6_29.

[6] Olsen Wings A/S, *Internal documents*, 2025.

[7] P. Robynne Murray, D. Snowberg, D. Berry, R. Beach, S. Rooney, and D. Swan, “Manufacturing a 9-Meter Thermoplastic Composite Wind Turbine Blade: Preprint,” Tech. Rep., 2017. [Online]. Available: https://docs.nrel.gov/docs/fy18osti/68615.pdf.

[8] P. U. Haselbach, F. Zahle, P. Berring, *et al.*, “Blade research and demonstration platform,” in *Journal of Physics: Conference Series*, vol. 1618, IOP Publishing Ltd, Sep. 2020. DOI: 10.1088/1742-6596/1618/5/052073.

[9] C. Bak, R. Bitsche, A. Yde, *et al.*, “Light rotor: The 10-mw reference wind turbine,” in *Proceedings of EWEA 2012 - European Wind Energy Conference & Exhibition*, Copenhagen, Denmark: European Wind Energy Association (EWEA), 2012. [Online]. Available: https://backend.orbit.dtu.dk/ws/portalfiles/portal/7946741/Light_Rotor.pdf.

[10] C. Bak, F. Zahle, R. Bitsche, *et al.*, “The DTU 10-MW Reference Wind Turbine. Sound/Visual production (digital),” Tech. Rep., 2013. [Online]. Available: https://backend.orbit.dtu.dk/ws/files/55645274/The_DTU_10MW_Reference_Turbine_Christian_Bak.pdf.

[11] *Vindenergianlæg - Del 5: Vindmøllevinger*. Dansk Standard, 2020. [Online]. Available: https://www.ds.dk.

[12] S. Gamesa, *Siemens Gamesa's Danish blade plant celebrates 20-year anniversary*, Accessed: 23 Jan 2025, 2022. [Online]. Available: https://www.siemensgamesa.com/global/en/home/explore/journal/2022/06/wind-blade-factory-aalborg-anniversary.html.

[13] S. L. Lee and S. J. Shin, "Structural design optimization of a wind turbine blade using the genetic algorithm," *Engineering Optimization*, vol. 54, no. 12, pp. 2053–2070, 2022, ISSN: 10290273. DOI: 10.1080/0305215X.2021.1973450.

[14] P. S. Veers, T. D. Ashwill, H. J. Sutherland, *et al.*, *Trends in the design, manufacture and evaluation of wind turbine blades*. John Wiley and Sons Ltd, 2003, vol. 6, pp. 245–259. DOI: 10.1002/we.90.

[15] S. Sajan and D. Philip Selvaraj, "A review on polymer matrix composite materials and their applications," in *Materials Today: Proceedings*, vol. 47, Elsevier Ltd, 2021, pp. 5493–5498. DOI: 10.1016/j.matpr.2021.08.034.

[16] H. Boudounit, M. Tarfaoui, and D. Saifaoui, "Modal analysis for optimal design of offshore wind turbine blades," in *Materials Today: Proceedings*, vol. 30, Elsevier Ltd, 2019, pp. 998–1004. DOI: 10.1016/j.matpr.2020.04.373.

[17] J. Hwang, D. J. Platenkamp, and R. Beukema, *A Literature Survey on Remote Inspection of Offshore Wind Turbine Blades Automated Inspection and Repair of Turbine Blades (AIRTuB)-WP1*, 2021. [Online]. Available: http://hdl.handle.net/10921/1559.

[18] Y. Khagendra Kumar and D. Singh Lohchab, "Influence of Aviation Fuel on Mechanical properties of Glass Fiber-Reinforced Plastic Composite," *IARJSET International Advanced Research Journal in Science, Engineering and Technology*, vol. 3, 2016, ISSN: 2394-1588. DOI: 10.17148/IARJSET.2016.3413. [Online]. Available: https://www.researchgate.net/publication/305996572.

[19] B. A. Newcomb and H. G. Chae, "The properties of carbon fibers," in *Handbook of Properties of Textile and Technical Fibres*, Elsevier, Jan. 2018, pp. 841–871, ISBN: 9780081012727. DOI: 10.1016/B978-0-08-101272-7.00021-3.

[20] F. R. Jones and N. T. Huff, "The structure and properties of glass fibers," in *Handbook of Properties of Textile and Technical Fibres*, Elsevier, Jan. 2018, pp. 757–803, ISBN: 9780081012727. DOI: 10.1016/B978-0-08-101272-7.00019-5.

[21] P. Bortolotti, D. Berry, R. Murray, *et al.*, "A Detailed Wind Turbine Blade Cost Model," Tech. Rep., 2019. [Online]. Available: https://docs.nrel.gov/docs/fy19osti/73585.pdf.

[22] J. P. Carey, "Introduction to braided composites," in *Handbook of Advances in Braided Composite Materials: Theory, Production, Testing and Applications*, Elsevier Inc., 2017, pp. 1–21, ISBN: 9780081003770. DOI: 10.1016/B978-0-08-100369-5.00001-5.

[23] L. Mishnaevsky, K. Branner, H. Petersen Nørgaard, J. Beauson, M. McGugan, and B. F. Sørensen, *Materials for wind turbine blades: An overview*. MDPI AG, 2017, vol. 10. DOI: 10.3390/ma10111285.

[24] C. Wu, F. Xu, H. Wang, H. Liu, F. Yan, and C. Ma, *Manufacturing Technologies of Polymer Composites - A Review*. MDPI, Feb. 2023, vol. 15. DOI: 10.3390/polym15030712.

[25] C. Kaboglu, S. Pimenta, A. Morris, and J. P. Dear, "The Effect of Different Types of Core Material on the Flexural Behavior of Sandwich Composites for Wind Turbine Blades," Tech. Rep. 2, 2017, pp. 1102–1109.

[26] W. S. Carron, D. Snowberg, P. Murdy, and S. Hughes, "Using Large-Scale Additive Manufacturing for Wind Turbine Blade Core Structures," Tech. Rep., 2023. [Online]. Available: https://docs.nrel.gov/docs/fy23osti/85673.pdf.

[27] Lantor BV, *Soric® textile foam core*, Accessed: 06 Mai 2025. [Online]. Available: https://www.lantorcomposites.com/textile-foam-cores/soric/.

[28] W. H. Wu and W. B. Young, "Structural analysis and design of the composite wind turbine blade," *Applied Composite Materials*, vol. 19, no. 3-4, pp. 247–257, 2012, ISSN: 0929189X. DOI: 10.1007/s10443-011-9193-z.

[29] J. H. Sjølund and E. Lund, "Structural gradient based sizing optimization of wind turbine blades with fixed outer geometry," *Composite Structures*, vol. 203, pp. 725–739, 2018, ISSN: 02638223. DOI: 10.1016/j.compstruct.2018.07.031.

[30] K. Hayat and S. K. Ha, "A parametric study of skin laminates used in the composite layup of large-scale wind turbine blades," *Advanced Composite Materials*, vol. 27, no. 2, pp. 195–208, 2018. DOI: 10.1080/09243046.2017.1405599. [Online]. Available: https://doi.org/10.1080/09243046.2017.1405599.

[31] N. Buckney, S. Green, A. Pirrera, and P. M. Weaver, "On the structural topology of wind turbine blades," *Wind Energy*, vol. 16, no. 4, pp. 545–560, 2013, ISSN: 10991824. DOI: 10.1002/we.1504.

[32] J. P. Blasques and M. Stolpe, "Multi-material topology optimization of laminated composite beam cross sections," *Composite Structures*, vol. 94, no. 11, pp. 3278–3289, 2012, ISSN: 02638223. DOI: 10.1016/j.compstruct.2012.05.002.

[33] S. Zhong, G. Jin, Y. Chen, T. Ye, and T. Zhou, *Review of Vibration Analysis and Structural Optimization Research for Rotating Blades*. Editorial Board of Journal of Harbin Engineering, 2024. DOI: 10.1007/s11804-024-00405-6.

[34] S. N. Sørensen, R. Sørensen, and E. Lund, "DMTO - A method for Discrete Material and Thickness Optimization of laminated composite structures," *Structural and Multidisciplinary Optimization*, vol. 50, no. 1, pp. 25–47, 2014, ISSN: 16151488. DOI: 10.1007/s00158-014-1047-5.

[35] L. X. Qian, W. X. Zhong, K. T. Chen, and Y. K. Sui, "An Approach to Structural Optimization - Sequential Quadratic Programming, SQP," *Engineering Optimization*, vol. 8, no. 1, pp. 83–100, 1984. DOI: 10.1080/03052158408902482. [Online]. Available: https://doi.org/10.1080/03052158408902482.

[36] J. Zhu, X. Cai, P. Pan, and R. Gu, "Multi-objective structural optimization design of horizontal-axis wind turbine blades using the non-dominated sorting genetic algorithm II and finite element method," *Energies*, vol. 7, no. 2, pp. 988–1002, 2014, ISSN: 19961073. DOI: 10.3390/en7020988.

[37] C. R. Çırak and H. Çalık, “Hotspots in maximum power point tracking algorithms for photovoltaic systems – A comprehensive and comparative review,” *Engineering Science and Technology, an International Journal*, vol. 43, 2023, ISSN: 22150986. DOI: 10.1016/j.jestch.2023.101436.

[38] C. Cobos Sánchez, F. J. Garcia-Pacheco, J. M. G. Rodriguez, and J. R. Hill, “An inverse boundary element method computational framework for designing optimal TMS coils,” *Engineering Analysis with Boundary Elements*, vol. 88, pp. 156–169, 2018, ISSN: 09557997. DOI: 10.1016/j.enganabound.2017.11.002.

[39] M. Jureczko, M. Pawlak, and A. Mezyk, “Optimisation of wind turbine blades,” *Journal of Materials Processing Technology*, vol. 167, no. 2-3, pp. 463–471, 2005, ISSN: 09240136. DOI: 10.1016/j.jmatprotec.2005.06.055.

[40] J. Chen, Q. Wang, X. Shen W. Z.and Pang, S. Li, and X. Guo, “Structural optimization study of composite wind turbine blade,” *Materials and Design*, vol. 46, pp. 247–255, 2013, ISSN: 02641275. DOI: 10.1016/j.matdes.2012.10.036.

[41] R. H. Barnes and E. V. Morozov, “Structural optimisation of composite wind turbine blade structures with variations of internal geometry configuration,” *Composite Structures*, vol. 152, pp. 158–167, 2016, ISSN: 02638223. DOI: 10.1016/j.compstruct.2016.05.013.

[42] S. M. Hermansen and E. Lund, “Multi-material and thickness optimization of a wind turbine blade root section,” *Structural and Multidisciplinary Optimization*, vol. 67, no. 7, 2024, ISSN: 16151488. DOI: 10.1007/s00158-024-03811-0.

[43] S. M. Hermansen, T. Macquart, and E. Lund, “Gradient-based structural optimization of a wind turbine blade root section including high-cycle fatigue constraints,” *Engineering Optimization*, 2025, ISSN: 10290273. DOI: 10.1080/0305215X.2024.2428678.

[44] M. K. McWilliam, T. K. Barlas, H. A. Madsen, and F. Zahle, “Aero-elastic wind turbine design with active flaps for AEP maximization,” *Wind Energy Science*, vol. 3, no. 1, pp. 231–241, 2018, ISSN: 23667451. DOI: 10.5194/wes-3-231-2018.

[45] P. U. Haselbach, “An advanced structural trailing edge modelling method for wind turbine blades,” *Composite Structures*, vol. 180, pp. 521–530, 2017, ISSN: 02638223. DOI: 10.1016/j.compstruct.2017.08.029.

[46] E. Q. Sun, *Shear Locking and Hourglassing in MSC Nastran , ABAQUS , and ANSYS*, 2006. [Online]. Available: https://api.semanticscholar.org/CorpusID:16443110.

[47] H. Ounis and A. Balehouane, “Buckling behavior of wind turbine blade,” *Journal of Renewable Energies*, vol. 19, no. 4, pp. 509–516, 2023, ISSN: 1112-2242. DOI: 10.54966/jreen.v19i4.589.

[48] L. Mishnaevsky, “Root Causes and Mechanisms of Failure of Wind Turbine Blades: Overview,” *Materials*, vol. 15, no. 9, 2022, ISSN: 19961944. DOI: 10.3390/ma15092959.

[49] Dassault Systèmes Simulia Corp., *Plane Stress Orthotropic Failure Measures (Section 17.2.3)*, 2006. [Online]. Available: https://classes.engineering.wustl.edu/2009/spring/mase5513/abaqus/docs/v6.6/books/usb/pt05ch17s02abm04.html.

[50] Composite Materials Hub, *Failure criteria in composite materials*, Accessed:16 Aug 2025. [Online]. Available: https://compositematerialshub.com/failure-criteria-in-composite-materials/.

[51] I. Daniel and O. Ishai, "Failure criteria and margins of safety," in *Practical Micromechanics of Composite Materials*, J. Aboudi, S. Arnold, and B. Bednarcyk, Eds., Butterworth-Heinemann, 2021, pp. 161–214, ISBN: 978-0-12-820637-9. DOI: 10.1016/B978-0-12-820637-9.00008-8.

[52] H. Söker, "Loads on wind turbine blades," in *Advances in Wind Turbine Blade Design and Materials*, Elsevier, 2023, pp. 55–78, ISBN: 9780081030073. DOI: 10.1016/B978-0-08-103007-3.00002-1.

[53] *Wind energy generation systems. Part 1 : Design requirements*. International Electrotechnical Commisson, 2019, p. 168, ISBN: 9782832262535.

[54] K. Y. Maalawi and H. M. Negm, "Optimal frequency design of wind turbine blades," *Journal of Wind Engineering and Industrial Aerodynamics*, vol. 90, pp. 961–986, 2002. DOI: 10.1016/S0167-6105(02)00214-3.

[55] R. Damiani and D. Davis, "Aeroelastic Modeling for Distributed Wind Turbines: March 11, 2021 - November 10, 2021," Tech. Rep., 2022. [Online]. Available: https://docs.nrel.gov/docs/fy22osti/81724.pdf.

[56] Y. Huang, X. Yang, W. Zhao, and D. Wan, "Aeroelastic analysis of wind turbine under diverse inflow conditions," *Ocean Engineering*, vol. 307, 2024, ISSN: 00298018. DOI: 10.1016/j.oceaneng.2024.118235.

[57] K. Thomsen, "The Statistical Variation of Wind Turbine Fatigue Loads," Tech. Rep., 1998. [Online]. Available: https://backend.orbit.dtu.dk/ws/portalfiles/portal/7751353/ris_r_1063.pdf.

[58] P. U. Haselbach, *Ultimate Strength of Wind Turbine Blades under Multiaxial Loading*. DTU Wind Energy, 2015, vol. 10, ISBN: 9788793278929.

[59] W. D. Calliste Jr. and D. G. Rethwisch, *Materials Science and Engineering: An Introduction*, 9th. John Wiley & Sons, 2013, ISBN: 9781118476543.

[60] Composite Materials Hub, *Rule of mixtures in composite materials*, Accessed: 18 Apr 2025. [Online]. Available: https://compositematerialshub.com/rule-of-mixtures/.

[61] PersiaResin, *Mechanical Properties of Unsaturated Polyester Resin*, Accessed: 22 Apr 2025. [Online]. Available: https://persiaresin.com/en/mechanical-unsaturated-polyester-resin/.

[62] K. K. Chawla, *Composite Materials: Science and Engineering*, 4th. Springer Nature Switzerland AG, 2019, p. 560, ISBN: 9783030289829. DOI: 10.1007/978-3-030-28983-6.

[63] 3B-Fibreglass, *HiPer-tex® – High performance glass*, 3B-Fibreglass — Glass Technology section, Accessed: 26 Mar 2025. [Online]. Available: https://www.3b-fibreglass.com/HiPer-tex.

[64] EurocodeApplied.com, *Eurocode 3 – Table of design properties for structural steel*, Accessed: 03 Mai 2025. [Online]. Available: https://eurocodeapplied.com/design/en1993/steel-design-properties.

[65] E. Gaertner, J. Rinker, L. Sethuraman, *et al.*, "Definition of the IEA Wind 15-Megawatt Offshore Reference Wind Turbine Technical Report," Tech. Rep., 2020. [Online]. Available: https://docs.nrel.gov/docs/fy20osti/75698.pdf.

[66] S. Markkilde Petersen, "Wind Turbine Test Vestas V27-225 kW," Risø National Laboratory, Roskilde, Denmark, Tech. Rep. Risø-M-2861, 1990. [Online]. Available: https://www.osti.gov/etdeweb/servlets/purl/7795314.

[67] A. M. Antunes, D. R. Verelst, R. Riva, *et al.*, "Static response of wind turbine blades: Comparison of low- and high-fidelity numerical models," in *Journal of Physics: Conference Series*, vol. 2767, Institute of Physics, 2024. DOI: 10.1088/1742-6596/2767/5/052037.

[68] L. Jin, Y. Chen, X. Tang, J. Zhang, and Z. Wang, "A numerical study on damage characteristics in composite tapered laminates under cyclic loading with different stress ratios," *Composite Structures*, vol. 311, 2023, ISSN: 02638223. DOI: 10.1016/j.compstruct.2023.116777.

[69] I. Ashcroft and J. A. Pascoe, "Evaluating and predicting fatigue behavior in adhesively bonded joints," in *Advances in Structural Adhesive Bonding, Second Edition*, Elsevier, 2023, pp. 643–674, ISBN: 9780323912143. DOI: 10.1016/B978-0-323-91214-3.00026-0.

[70] P. Virtanen, R. Gommers, T. E. Oliphant, *et al.*, "SciPy 1.0: Fundamental Algorithms for Scientific Computing in Python," *Nature Methods*, vol. 17, pp. 261–272, 2020, Accessed documentation page: https://docs.scipy.org/doc/scipy/reference/generated/scipy.optimize.minimize.html. DOI: 10.1038/s41592-019-0686-2.